

Outflows in Starburst Galaxies

Master's Thesis in Physics and Astronomy

Presented by

Saurabh Mittal

September 15, 2022

Astronomisches Institut Dr. Karl Remeis-Sternwarte
Friedrich-Alexander-Universität Erlangen-Nürnberg



Supervisor: Prof. Dr. Manami Sasaki

Abstract

This thesis explores the X-ray emission from the outflows of star forming galaxies. The first part of this thesis consists of the analysis of *Chandra* data to study the outflows from M82. The latter part utilises this analysis to perform simulations and validate the expectations for the *Athena* WFI instrument.

X-ray instrumentation has been evolving for decades with newer detectors ranging from *Chandra*, *XMM-Newton* to *eROSITA* providing improved resolution and sensitivity. To maintain the pace of discovery in the field, instrumentation needs to keep evolving which is what is expected from the upcoming *Athena* mission that will offer improved spatial resolution and spectroscopic properties. The *Athena*-WFI provides a large field of view with excellent energy resolution while high spectral resolution is achieved from *Athena* X-IFU.

X-ray observations act as a powerful probe that allow us to study outflows from starburst galaxies and other accretion driven processes therefore providing insight into the physics related to feedback. The mean X-ray spectra of starburst galaxies contain valuable information about the highly energetic processes involved along with the chemical composition and thermodynamics of the outflowing gas. An improved understanding of the evolution of galaxies and furthermore the evolutionary trend in the early universe can be obtained by studying such galactic outflows. Therefore, with the advanced instrumental capabilities expected from *Athena*, one would be able to resolve the X-ray spectra from galactic outflows at cosmological distances revolutionizing our current understanding of such sources. This work also validates these expectations and the simulated data show a major improvement in *Athena*'s spatial resolving capabilities and sensitivity as compared to the observations made from *Chandra*.

Contents

1	Introduction	7
2	Starburst galaxies	8
2.1	Outflows from starburst galaxies	8
2.2	Driving mechanisms	9
2.3	X-ray emission	9
2.3.1	X-ray binaries	10
2.3.2	Supernova remnants	12
2.3.3	Compton scattering	12
2.3.4	Diffuse thermal plasma	12
3	M82	13
4	X-Ray instrumentation	13
4.1	<i>Chandra</i>	14
4.2	<i>Athena</i>	16
4.3	Simulation tools	16
5	Creating a diffuse emission image for M82	19
6	Spectrum extraction and analysis for M82	26
7	Spectral fitting	30
8	Simulation modeling	34
9	Simulations at higher red-shifts	49
10	Conclusion	52
A	Spectral fits	57
B	<i>Chandra</i> diffuse emission images	62
C	Simulated spectral fits	63
	Bibliography	68

1 Introduction

Starburst galaxies are objects with intense recent star-formation, having galaxy-sized outflows with velocities ranging from several hundreds to a thousand kilometers per second. This increased star-formation activity drives a chain of stellar and interstellar (IS) phenomena exhibiting far-infrared (FIR) and X-ray emission. The FIR emission from starburst galaxies is a result of the efficient heating of the IS dust by the radiation from abundant massive stars making it a characteristic feature of starburst galaxies [Soifer et al., 1986]. The enhanced star formation rate also makes them a powerful X-ray emitter compared to normal galaxies due to the energetic phenomena related to the end stages of stellar evolution (X-ray binaries, supernova remnants, galactic winds and Compton scattering). Furthermore, increased stellar activity also leads to higher supernova (SN) rate, shock heating of the IS gas, and more efficient particle acceleration mechanisms compared to normal galaxies.

The data analysis in this work is based on 9 different observations of a nearby starburst galaxy M82 made by *Chandra* ACIS between 1999-2010 totaling an exposure time of 534 ks. These observations are utilized to create diffuse emission images, analyse the diffuse emission and study the variations in its thermal and metallic properties as a measure of distance from the starburst nucleus. These images and spectral results are further utilized to perform simulations on the *Athena* WFI instrument at higher redshifts to estimate the spatial resolving capabilities of the instrument.

In §2, an introduction about starburst galaxies, their outflows, and emission from these outflows is described followed by a brief overview of M82 in §3. The X-ray telescope and instrumentation utilized for the analysis is detailed in §4. §5 describes the steps to remove the discrete sources from the *Chandra* ACIS observations and create diffuse emission images for M82. The spectrum extraction process from this diffuse emission is described in §6 followed by the spectral fitting models detailed in §7. Finally, §8 and §9 explain the steps performed to run simulations on the *Athena* WFI instrument at M82's current distance and higher distances respectively. §10 summarizes the results obtained in this thesis along with the future implications and prospects.

2 Starburst galaxies

Starburst galaxies (SBGs) are galaxies which are experiencing a brief ($10^7 - 10^8$ year) burst of intense star formation activity. They are observed to be forming stars at an unusually high rate about 10^3 greater than that in a normal galaxy [Swinburne, 2022]. This high star forming activity is usually observed around the nucleus of the galaxy but can also extend and be spread around throughout the galaxy. Starburst can be triggered by tidal interactions or mergers between gas-rich galaxies. Such interactions can result in a tidal tail in a galaxy which is a commonly observed feature in galaxies undergoing high star formation. Tidal interactions and mergers can also cause lopsidedness in a galaxy and studies have also shown a strong direct correlation between lopsidedness of a galaxy and its young stellar population [Reichard et al., 2009] providing further evidence that such encounters could be the triggering mechanisms for starburst. Starburst galaxies are typically surrounded by large amounts of dust which is heated by the radiation from young massive stars therefore emitting infrared radiation and making them among the most luminous infrared objects in the universe. These young massive stars burn very rapidly and are likely to explode at the end of their lives as supernovae whose winds can sweep away the gas from the galaxy affecting/inhibiting any further star formation. The hot phase of the interstellar medium (ISM) can also break out of the disk of the galaxy and escape into the halo or circumgalactic medium (CGM). A large number of distant galaxies observed in the early universe are known to be starburst but cannot be studied in greater detail due to their large distances. Therefore, studying the physics of nearby starburst galaxies can provide insight to the history of galaxy formation and evolution and can also give us more information about the young stages of the universe.

2.1 Outflows from starburst galaxies

Star forming activity in a galaxy can often initiate large scale outflows (winds), that are responsible for removing metals from the galaxy and polluting the inter-galactic medium (IGM) e.g. in M82 [Shopbell and Bland-Hawthorn, 1998], Arp 220 [Varenius et al., 2016], and NGC 253 [Walter et al., 2017, Krieger et al., 2019]. These outflows are usually produced when stellar winds from young stars, and energetic particles and gas from supernova events collide creating a bi-conical structure (the path of least resistance ¹) that extends above and below the plane of the host galaxy [Veilleux et al., 2005]. They are usually multi-phase, with a cool component ($T_c \sim 10^2 - 10^4$ K) [Strickland et al., 1996, Lehnert et al., 1999] and a hot component ($T_h \sim 10^7$ K) [McKeith et al., 1995] [Shopbell and Bland-Hawthorn, 1998], galactic scale ($R \gtrsim 5-20$ kpc) [Strickland et al., 2009] and have been observed in galaxies of different masses and environments. The galactic outflows can reach velocities between 10 - 1000 km s⁻¹ [Rupke et al., 2005, Rubin et al., 2014] and can extend to a few tens of kpc [Veilleux et al., 2005, Bland-Hawthorn et al., 2007, Rubin et al., 2014]. However, the X-ray emitting gas region is bound to a few kpc from the

¹This path of least resistance mainly depends on the conditions exterior to the star-forming core

starburst nucleus [Strickland and Stevens, 2000, Devine and Bally, 1999, Tsuru et al., 2007]. Outflows generated from star-forming activities in galaxies carry away energy, gas and metals from the star-forming regions to the CGM of their host galaxy. This regulates the inflow of galactic gas, and by extension, star formation activity, thus acting as a feedback mechanism alongside other processes operating within the interior of the host [Owen et al., 2018]. Such feedback processes have large scale impacts and can heavily regulate the evolution of the host object. This interdependency between outflows from a galaxy and its star forming activity implies that the two processes co-evolve together, and therefore, examining the observational characteristics of galactic outflows would provide insights into the evolutionary trends of the host.

2.2 Driving mechanisms

The driving mechanisms of an outflow are governed by the properties of their host galaxy. Outflows from starburst galaxies can be “driven” or “accelerated” by thermal pressure (corresponding to the thermal content of the gas), radiation pressure, and/or cosmic rays (CRs) [Yu et al., 2020]. Thermal outflows can be a result of the heating of the ISM by overlapping core-collapse SN explosions. If the driving force of the SN remnant exceeds the local escape velocity, this can result in a thermally driven wind. Stellar feedback also includes CRs. The SN remnant shock is an efficient accelerator of CRs and about $\sim 10\%$ of the SN energy can be converted into CR energy which can contribute to large-scale galactic outflows. For massive stars, radiation pressure is one of the dominant feedback mechanisms to affect their surrounding medium before the final SN explosion and may also be responsible in launching galactic winds². While a metal-rich galaxy can be driven by radiation pressure, thermal pressure may dominate in a metal-poor galaxy. Outflows from M82 like galaxies comprise of two coupled fluid components: a hot ionized thermal gas and CRs (relativistic non-thermal fluid). For galaxies such as M82, it is found that outflows dominated by thermal mechanical pressure delivers the fastest and hottest ($\sim 10^7\text{K}$) winds making them the most effective mechanism in accelerating a wind followed by CRs and then radiation pressure. Radiation driven winds in such environments fail to attain similar velocities and tend to be denser thus more susceptible to cooling. CR-driven outflows have velocities falling between thermal pressure driven and radiation pressure driven cases [Yu et al., 2021].

2.3 X-ray emission

X-ray emission in galaxies is either related to stellar activity, or closely associated with it through SN and SN-driven gas heating and particle acceleration processes. Previous studies of X-ray sources in external galaxies have shown that the X-ray populations above typical *Chandra* detection luminosity ($\sim 10^{37}\text{ergs s}^{-1}$) [Chiang and Kong, 2011] of nearby galaxies are dominated by X-ray binaries, which consist of an accreting compact

²although inefficient in driving the outflow in most scenarios

object (neutron star or black hole) and a stellar companion. Young supernova remnants (SNRs) also contribute to this population. Additionally, starburst galaxies are also known to be X-ray sources, with X-ray emission coming from their hot ISM, stars, accreting compact objects/X-ray binaries, SNe, galactic wind outflows, and Compton scattering of ambient FIR photons off SN-accelerated relativistic electrons ([Fabbiano, 1988, Persic and Rephaeli, 2002, Soria and Wu, 2002, Mitsuishi et al., 2013, Lopez et al., 2020]). The mean X-ray spectrum of starburst galaxies reflects the diverse nature of the high-energy activity in starburst galaxies. X-ray observations are a natural and powerful probe of the composition and the thermodynamics of the hot ISM and thus, a powerful tool in exploring the physics of feedback. Features in the X-ray spectra of outflows correlate with the abundances of elements which in turn depend on the thermal properties of the emitting gas. The hot phases of the ISM predominantly emit in the X-ray energy band $\sim 0.1 - 10$ keV with elements like O, Ne, Mg, Si, S, and Fe dominating at temperatures $T \lesssim 10^7$ K and Ar, Ca, and Fe showing strong emission lines at higher temperatures. These abundances of elements change with the evolution of the galaxy which is reflected in their spectra. The X-ray spectra also varies over redshifts regardless of the underlying driving mechanisms. Outflows from nearby starburst galaxies, such as NGC 253 and M82, can be resolved in X-rays and [Lopez et al., 2020] determined the temperature profiles of M82's outflows at different distances along its minor axis. However, outflows in distant starburst galaxies are not always spatially resolvable in X-ray observations but their X-ray spectral information can still be retained providing helpful understanding about the thermal properties of the outflow gas. The variability in fluxes across different X-ray energy bands can also provide constraints for the physical conditions within the X-ray emitting outflow gas. Better spectral resolving capabilities and large effective photon collecting areas like that of the *Athena* X-ray observatory will also improve the simulated studies of such outflows by allowing for precise thermodynamical and element abundance determinations. X-ray observations of a given galaxy at multiple epochs have provided opportunities to study long-term variability of X-ray sources in galaxies. A deeper understanding of galactic X-ray sources and comparison with the lesser understood extragalactic X-ray sources, can help in probing the nature of the source and understanding the source populations.

2.3.1 X-ray binaries

Binary systems constitute the brightest class of Galactic X-ray sources. X-ray binaries can be fully characterized based on the mass of the donor star or the nature of the accreting object:

- **High mass X-ray binaries (HMXBs):** A HMXB consists of a compact object (most frequently a neutron star) and an optical companion which is a main-sequence star with $M_{\text{opt}} \gtrsim 8 M_{\odot}$ that loses matter via strong stellar winds. The compact object accretes from the stellar winds rather than an accretion disk resulting in bright X-ray emission. Previous studies of HMXBs suggest that the X-ray photon spectrum from bright ($L_x \gtrsim 10^{37}$ ergs s^{-1}) HMXBs in the 2 - 50 keV band has a

broken power law profile ([Persic and Rephaeli, 2002] and references therein) of the form:

$$f^{\text{H}}(\epsilon) \propto \begin{cases} \epsilon^{-\gamma} & \text{if } \epsilon \leq \epsilon_c \\ \epsilon^{-\gamma} e^{-[(\epsilon - \epsilon_c)/\epsilon_{\text{F}}]} & \text{if } \epsilon > \epsilon_c \end{cases} \quad (1)$$

where ϵ denotes energy (in keV), photon index $\gamma \simeq 1.2 \pm 0.2$, cutoff energy $\epsilon_c \sim 20$ keV, and e-folding energy $\epsilon_{\text{F}} \sim 12$ keV. This broken-law profile is likely a result of X-ray pulsations that arise when the magnetic and rotation axes of the NS are misaligned and if the beamed emission from the magnetic poles rotates through the line of sight of the observer. This is also a strong indicator of a highly magnetized neutron star ($B \sim 10^{12}$ G or larger) where for high mass accretion rates, the accreted material is funneled to the magnetic poles of the NS. Another characteristic in the HMXB spectrum is a Fe-K emission line with central energy in the range 6.4 – 6.7 keV. This feature is likely a result of the fluorescence of the cold and dense material close to the neutron star.

- **Low mass X-ray binaries (LMXBs):** A LMXB consist of a compact neutron star and an optical component which is a post-main-sequence star with $M_{\text{opt}} \lesssim 1 M_{\odot}$. The companion is unable to sustain the accretion through stellar wind (unlike HMXBs) and thus the main channel for matter transfer is via Roche-lobe overflow³. The X-ray spectra of a LMXB in the 0.5 – 20 keV band has a partially Comptonized thermal spectrum ([Persic and Rephaeli, 2002] and references therein) described by:

$$f^{\text{L}}(\epsilon) \propto \begin{cases} \epsilon^{-1.4} e^{-\epsilon/kT} & \text{if } L_{\text{x}} < 10^{37} \text{ erg s}^{-1} \\ e^{-\epsilon/kT} & \text{if } L_{\text{x}} \geq 10^{37} \text{ erg s}^{-1} \end{cases} \quad (2)$$

with $5 \lesssim kT \lesssim 10$, both ϵ and kT in keV [Christian and Swank, 1997]. Conversely for neutron stars with weaker magnetic fields ($B < 10^9$ G), the accretion disk may touch or come close to the NS surface, and the accreting material is distributed over a larger fraction of the NS surface resulting in such a Comptonized thermal spectrum.

Moreover, spectra of BHXBs have a distinct two-component signature (making it a good indicator of the presence of a BH in an X-ray binary [Lewin et al., 1997]): an *ultrasoft* component with a characteristic temperature of $\gtrsim 1$ keV [Ebisawa et al., 1994], and an *ultrahard* power law with photon index in the range ~ 1.5 to ~ 2.5 that extends up to several hundred keV [Wilson and Rothschild, 1983].

³Roche lobe is a region around a star in a binary system where matter is gravitationally bound to the star. If the donor star fills its Roche lobe, matter can flow into the Roche lobe of the compact companion resulting in a steady supply of matter that builds up around the compact object in the form of an accretion disk.

2.3.2 Supernova remnants

X-ray emission from SNRs occurs mostly during the free expansion phase and part of the adiabatic phase of the evolution of SNRs [Woltjer, 1972, Chevalier, 1977]. The spectrum can generally be described with a thermal component that comes from the shock heated plasma ($kT \sim 2$ keV) and a non-thermal component from synchrotron radiation. The thermal emission is useful to reliably measure the abundances and connect them with supernova ejecta yields for the various types of supernova. The synchrotron radiation provides important clues about the cosmic-ray acceleration and magnetic field strengths near supernova remnant shock fronts. During the later stages of evolution (most of the adiabatic phase), SNRs are cool and dim with temperatures $0.5 \text{ keV} \lesssim kT \lesssim 1 \text{ keV}$ and virtually undetectable in X-rays during the radiative cooling phase due to very cool temperatures [Persic and Rephaeli, 2002].

2.3.3 Compton scattering

The high SN rate in a starburst galaxy results in high relativistic electron densities since SN shock are known to be primary sites of cosmic-ray acceleration. This suggests that a higher mean relativistic electron density is expected in a starburst galaxy than a normal galaxy. Studies have shown that the relativistic electron energy density is sufficient in starburst galaxies for part of the total emission to be due to Compton scattering. Enhanced radio emission is also observed from starburst galaxies due to the high density of electrons. If the same electron population produces both the radio and hard X-ray emission, then both spectra are expected to be powerlaws, with roughly the same index [Rephaeli, 1979, Goldshmidt and Rephaeli, 1995], of the form:

$$f_c(\epsilon) = K_c \epsilon^{-\beta}, \quad (3)$$

with β being the photon index roughly in the range $\sim 1.6 - 1.8$. The coefficient K_c can be expressed in terms of the measured radio flux and mean value of the magnetic field in the emitting region [Persic and Rephaeli, 2002].

2.3.4 Diffuse thermal plasma

SN explosions are expected to shock heat the ISM and the galactic-halo gas to approximately galactic virial temperatures, $kT \lesssim 1$ keV resulting in a thermal soft X-ray emission from the gas. Evidently, earlier studies of the $0.5 - 10$ keV spectra of starburst galaxies have also shown the presence of a < 1 keV thermal component [Ptak et al., 1997, Okada et al., 1997, Zezas et al., 1998, Cappi et al., 1999, Della Ceca et al., 1999] [Moran et al., 1999]. *Chandra* data for NGC253⁴ has shown that soft thermal X-rays come from the regions of interaction between the fast starburst-driven wind and the denser ambient ISM [Strickland et al., 2000]. [Strickland and Stevens, 2000] simulations

⁴another starburst galaxy ≈ 3.5 Mpc away

of starburst-driven winds also reveal that the soft X-rays come from the region of wind/ISM interaction, which is characterized by a multi-temperature, non-uniform plasma. The $\gtrsim 2$ keV thermal emission from the galactic wind mostly comes from the central starburst region itself [Pietsch et al., 2001]. The X-ray emission from thermal plasma in starburst galaxies can therefore be described as:

$$f_g(\epsilon) = K_g \times j_{\text{th}}(\epsilon; kT = 0.7 \text{ keV}, Z = Z_\odot) \quad (4)$$

where j_{th} is the spectral emissivity function ($\propto e^{-\epsilon/kT} T^{-1/2}$) and K_g is a density dependent normalization factor [Persic and Rephaeli, 2002].

3 M82

M82 is a classic example of a starbursting galaxy driving a superwind [Rieke et al., 1980, Leroy et al., 2015]. Its proximity ($D \sim 3.6$ Mpc) [Freedman et al., 2001, Gerke et al., 2011] (RA: 9:55:52.7, DEC: 69:40:46) [NASA, 2022] and nearly edge on orientation (with a disk inclination of 80° [McKeith et al., 1995]) makes it an ideal candidate for studying galactic outflows. It exhibits intense star-formation activity, with a very energetic and high-density core, and hosts the most luminous ultraluminous X-ray source, M82 X-1 ($L_x > 10^{41}$ ergs s^{-1}) [Chiang and Kong, 2011]. It is also one of the brightest IR galaxies in the sky [Telesco, 1988]. The star formation activity in M82 was most likely triggered by a close encounter with a neighboring spiral galaxy (M81) some 2×10^8 yr ago [Yun et al., 1994] but has substantially subsided as indicated by its stellar population's age analysis [De Grijs, 2001, Mayya et al., 2004]. Outflows of M82 have been studied across the electromagnetic spectrum with multiple observations in X-rays (e.g. [Ranalli et al., 2008, Konami et al., 2011, Lopez et al., 2020]). Previous *Chandra* observations in M82, have revealed a number of bright OB associations, the brightest of which has an X-ray luminosity of $\sim 5 \times 10^{38}$: this large X-ray emission is presumed to arise from a combination of diffuse plasma, unresolved HMXBs, and O stars [Griffiths et al., 2000]. Outflows from M82-like starburst galaxies have several ionized gas components with different thermal temperatures, as evident from the multi-temperature fits to their X-ray spectra performed by [Lopez et al., 2020] and further reproduced in Section §6. The investigated outflow region in this thesis spans a diameter of ~ 5 kpc.

4 X-Ray instrumentation

X-ray observatories have to be space-borne as X-rays are absorbed by the Earth's atmosphere. There have been multiple X-ray missions in the past such as *XMM-Newton*, *Chandra*, *eROSITA*, and missions such as *Athena* on the not too distant horizon. This thesis utilizes data obtained from *Chandra* ACIS for spectrum extraction and modeling of the outflows from M82. [Weisskopf et al., 2000] and [Harvard, 2019] are used as references for a brief overview of *Chandra* in §4.1. We also make use of *Athena* WFI to run

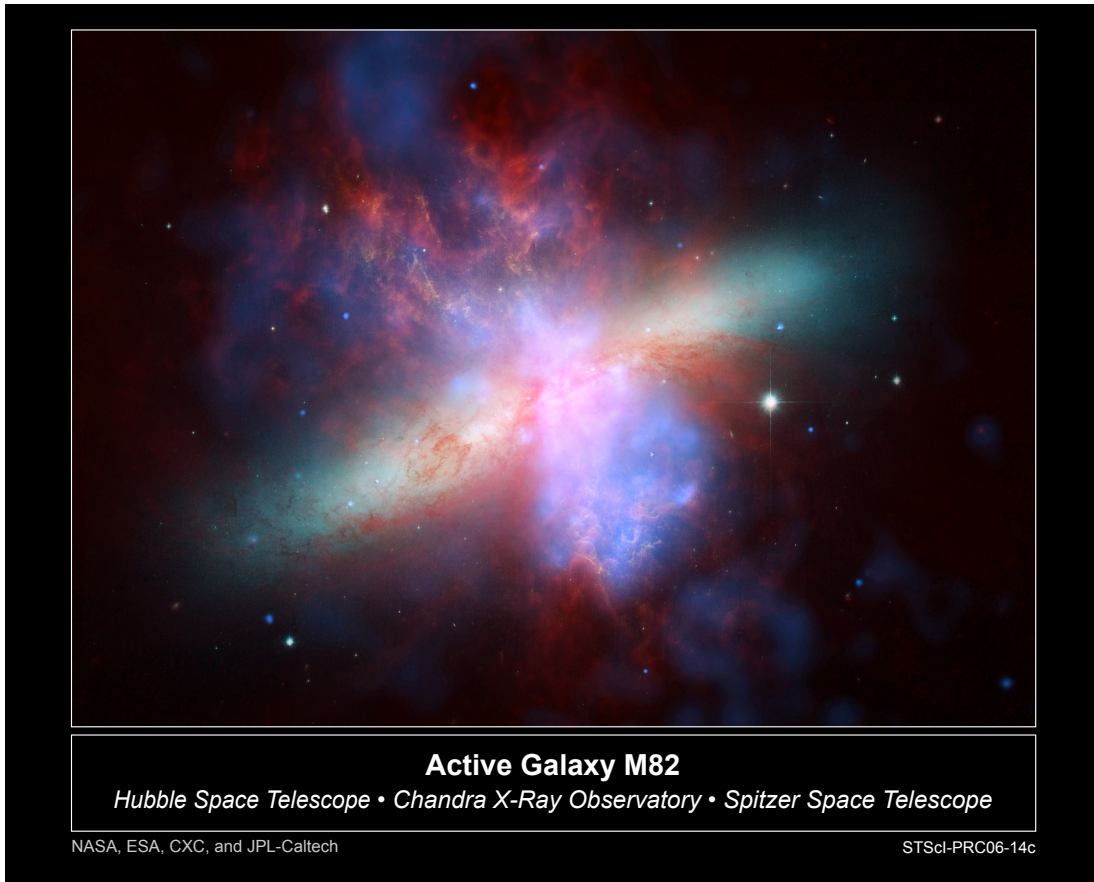


Figure 1: Multi-wavelength image of M82 obtained from the Hubble Space Telescope, Chandra X-Ray Observatory, and Spitzer Space Telescope [NASA, 2006]. X-ray data recorded by *Chandra* is shown here in blue; Infrared light by *Spitzer* appears in red; *Hubble* observations are shown in orange; The bluest visible light appears in yellow-green.

simulations and achieve a deeper understanding of the behavior of such outflows. A brief overview of *Athena* and its components is given in §4.2 using [Meidinger et al., 2017] and [Barcons et al., 2017] as the main references.

4.1 *Chandra*

The Chandra X-Ray Observatory (CXO)⁵ (Fig 2) is one of NASA’s ”Great Observatories”, alongside the Hubble Space Telescope (HST), the Compton Gamma-Ray Observatory (CGRO), and the Spitzer Space Telescope, and was launched in 1999. CXO possesses the abilities for sub-arcsecond imaging, spectrometric imaging, and for high resolution disper-

⁵<https://chandra.harvard.edu/>

sive spectroscopy over the X-ray band 0.08 - 10 keV (15 - 0.12 nm) [Weisskopf et al., 2000]. It combines the mirrors with four science instruments (LETG, HETG, ACIS, HRC) to capture and probe X-rays from astronomical sources. LETG and HETG are diffraction grating arrays used to redirect the X-rays based on their energy which is later accurately determined by HRC/ACIS. ACIS and HRC help provide information about the number, energy, position and the time of arrival of the incoming X-rays.

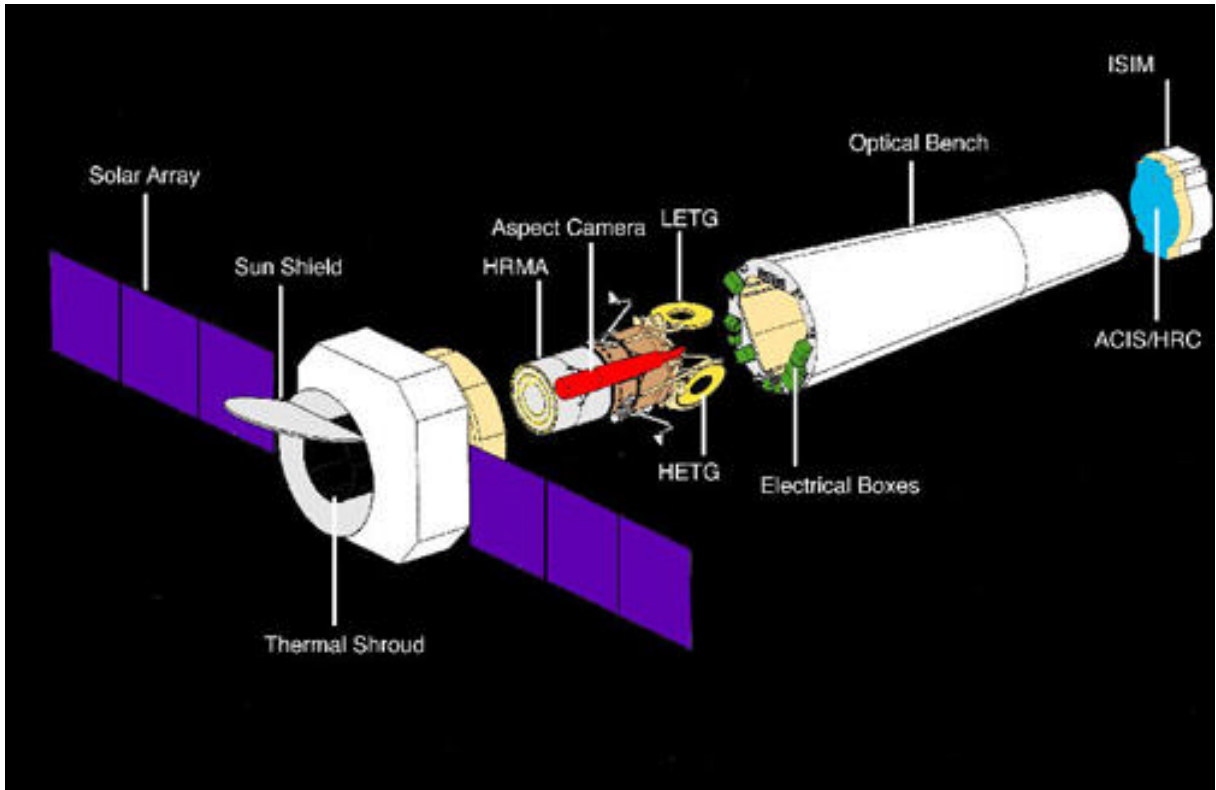


Figure 2: A schematic of the Chandra spacecraft with an explored view of the science instruments [Harvard, 2022b].

The instrumental components for CXO are briefly further described below:

- **Low Energy Transmission Grating/LETG and High Energy Transmission Grating/HETG:** These gratings diffract the intercepted X-rays and change their direction depending sensitively on the X-ray energy. These diffracted X-rays are further detected by one of the focal plane cameras (ACIS/HRC), where their energy is accurately determined. The LETG gratings cover an energy range of 0.08 - 2 keV and the HETG gratings (comprising of a High Energy Grating/HEG and a Medium Energy Grating/MEG) are designed to cover an energy range of 0.4 - 10 keV.
- **Advanced CCD Imaging Spectrometer/ACIS:** As the name suggests, ACIS is made of an array of CCDs and consists of two instruments: ACIS-I and ACIS-S.

ACIS-I provides high-resolution spectrometric imaging over a large field of view (17-arcmin-square). ACIS-S serves as a primary readout detector for the HETG and is also responsible for high-resolution spectrometric imaging over a 8-arcmin-square field of view but extending to lower energies than the ACIS-I.

- **High Resolution Camera/HRC:** The HRC also consists of two instruments: HRC-I optimized for imaging and HRC-S for spectroscopy. HRC-I has the largest field of view on-board *Chandra* (31-arcmin-square). HRC-S serves as a primary readout detector for the LETG. HRC has a wider energy range (0.06 - 10keV) than ACIS (0.08 - 10 keV) but with less intrinsic spectral resolution ($\Delta E/E \sim 1$) [Harvard, 2022a].

4.2 *Athena*

Athena (Advanced Telescope for High-ENergy Astrophysics)⁶ (Fig 3) is a future X-ray observatory mission selected by the European Space Agency (ESA), expected to be launched in the late 2020s. *Athena* will operate in the energy range 0.2 - 12 keV and will possess improved spectroscopic and imaging capabilities compared to the current X-ray observatories. *Athena* will perform surveys more than two orders of magnitude faster than *XMM-Newton* or *Chandra*. With the improved angular resolution, spectral resolution, throughput, and detection sensitivity, physical evolution of clusters and groups of galaxies at different epochs could be determined. *Athena's* white paper describes the observatory mission and instrumental statistics which can be found at [Nandra et al., 2013]. It comprises of two complimentary and interchangeable focal plane instruments, WFI and X-IFU, which are briefly discussed below:

- **Wide Field Imager/WFI:** WFI is a spectral imaging camera with a large field of view (40-arcmin-square). It also provides a detector featuring high count rate capability for the observation of very bright point sources. For this thesis, we utilize the WFI instrument for the purpose of running the simulations.
- **X-ray Integral Field Unit/X-IFU:** X-IFU is a X-ray spectrometer that provides very high spectral resolution.

4.3 Simulation tools

SIXTE: Simulation of X-ray TElescopes (SIXTE) software package is a mission-independent Monte Carlo simulation toolkit for X-ray astronomical instrumentation developed by Dr. Karl Remeis Sternwarte and Erlangen Center for Astroparticle Physics [Dauser et al., 2019]. The targets to be simulated are obtained from the SIMPUTs (described below), and based on the source definition, a sample of photons is produced. These photons are then propagated through a representation of the optics of the mission, resulting in a list of impact

⁶<https://www.the-athena-x-ray-observatory.eu/>

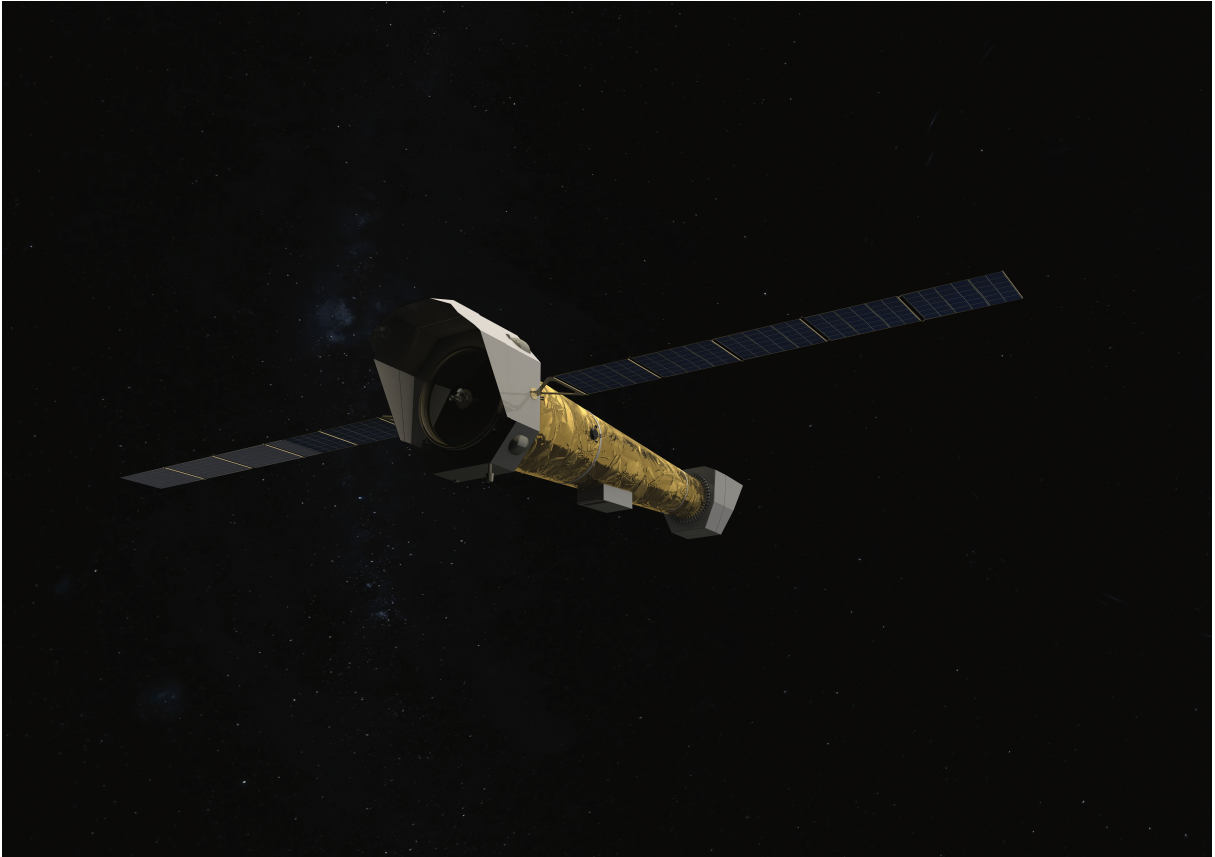


Figure 3: Artist's impression of *Athena* [ATHENA, 2022].

times, positions, and energies on the detector. These impacts are then utilized to generate the final event list. Figure 4 illustrates these three major functional blocks of SIXTE. More information about the usage of the tool can be found in the SIXTE manual⁷. The SIXTE software package contains various detector types such as *Athena-WFI* and *Athena X-IFU* and thus simulations can be performed for a wide range of specific instruments. The SIXTE tools utilized for the simulations in this thesis are:

- **attgen_dither**: The `attgen_dither` tool is used to create an attitude file. The attitude file is a FITS file that contains the pointing of the satellite RA and Dec for a given `time` in seconds. This is done in order to avoid imprinting the gaps in between the chips in the data.
- **athenawfisim**: This tool runs the simulation for the *Athena WFI* instrument by using the specified `simput` file for a certain exposure time and the XML-file(s). The properties of a specific instrument is described by a set of XML-file(s). Similar simulation tools exist in SIXTE for different detectors such as *runsixt* (only

⁷<https://www.sternwarte.uni-erlangen.de/sixte/>

for detectors described by a single XML-file), *xifupipeline* for the *Athena X-IFU* instrument, *erosim* for *eROSITA* simulations etc.

- **imgev**: The output event file(s), (multiple files can be combined using FTOOL *ftmerge*), obtained from the *Athena WFI* simulation can be used to create an image of the full WFI detector using the *Sixte* tool *imgev*.
- **makespec**: This tool creates a spectral file for a specified region in the output event file of *athenawfisim*.
- **radec2xy**: This tool calculates the X and Y sky pixel coordinates via a tangential parallel projection corresponding to the RA and Dec event coordinates.

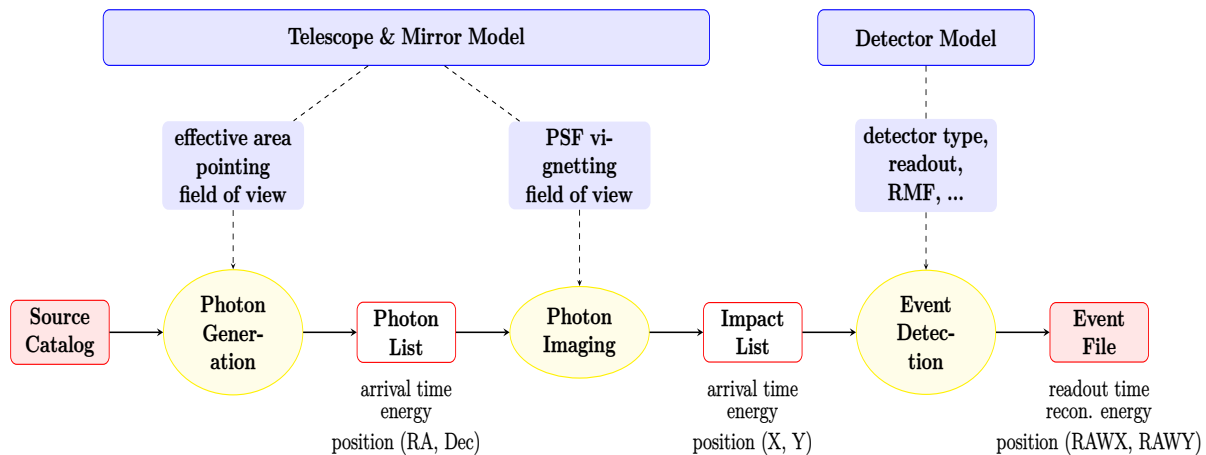


Figure 4: Flow chart illustrating the three major functional blocks of the SIXTE simulation software (yellow boxes) [Dauser et al., 2019].

SIMPOT: SIMulated inPUT or SIMPUT is a file format [Schmid et al., 2013] for source input files to enable realistic simulations of astronomical observations. It is based on the Flexible Image Transport System (FITS) [Wells and Greisen, 1979, Ponz et al., 1994, Hanisch et al., 2001, Pence et al., 2010] and contains information such as the position, flux, energy spectrum, spectral model, etc. of the source or multiple sources. This information is stored in different Header and Data Units (HDUs). SIMPUT is an instrument-independent definition of sources and thus can be used for different instrumentation e.g. *Chandra* or *Athena*. A schematic layout of a sample catalog is shown in Figure 5. The SIMPUT tools utilized for the simulations in this thesis are:

- **simputfile**: This tool produces a SIMPUT file containing a catalog with a source location, a spectrum, the desired energy range, the flux, and an image.
- **simputmerge**: This tool merges multiple simput files to a single file.

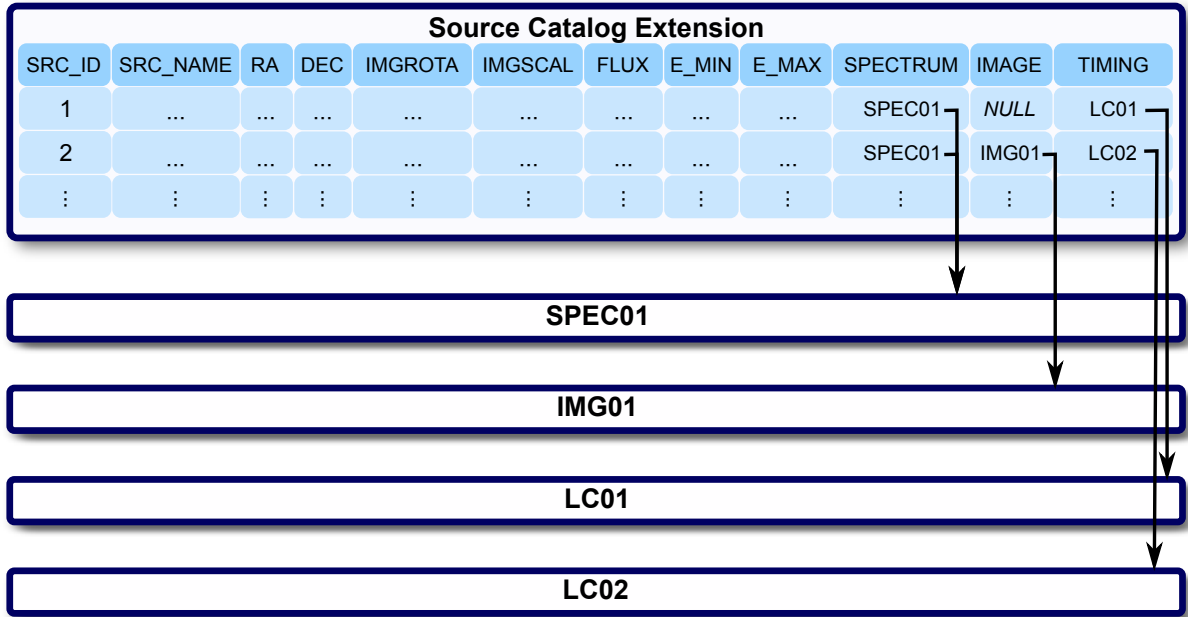


Figure 5: Schematic of a SIMPUT file. The source catalog contains information like the position and observed fluxes of one or more X-ray sources. Additional data describing the energy spectra, spatial extent and time variability is stored in separate Header and Data Units (HDUs) and linked in the source catalog [Dauser et al., 2019].

5 Creating a diffuse emission image for M82

We utilize existing *Chandra* ACIS observations taken between 1999-2010, for studying and analyzing the outflows from M82. These observations are detailed in Tab 1 and total an exposure time of 534 ks.

Observation Id	Instrument	Exposure	Date
361	ACIS-I	33.25 ks	1999-09-20
1302	ACIS-I	15.52 ks	1999-09-20
2933	ACIS-S	18.02 ks	2002-06-18
10542	ACIS-S	118.61 ks	2009-06-24
10543	ACIS-S	118.45 ks	2009-07-01
10544	ACIS-S	73.53 ks	2009-07-07
10545	ACIS-S	95.04 ks	2010-07-28
10925	ACIS-S	44.54 ks	2009-07-07
11800	ACIS-S	16.82 ks	2010-07-20

Table 1: *Chandra* ACIS observations for M82

The observations were reduced using *Chandra* Interactive Analysis of Observations (CIAO) Version 4.12⁸ to create an image of the diffuse emission from M82 and to study its spectral features. The data was reprocessed using *chandra_repro*⁹ to obtain the level 2 event files. While the *Chandra* ACIS chip reads out, it is still taking data. Photons detected during this readout are clocked out in the wrong row and therefore have incorrect y-chip values. These out-of-time events detected in the detector resulted in a streak running on both sides of the bright central core along the semi-major axis. This streak can be removed without loss of information using the CIAO command *acisreadcorr*¹⁰ by specifying the sky coordinates for the central bright source, and the thickness of the streak (acting as a source free background) dx,dy in chip-x and chip-y. The *dmextract*¹¹ command is then used to create a spectrum of this background region which is used to run *acisreadcorr*. The multiple observations were combined to a single tangent point to create a merged event file using *merge_obs*¹²¹³. This command also creates exposure corrected images and exposure maps for the combined observations as shown in Fig 6, in different energy bands listed in Tab 2.

Band	Energy range	Effective energy
Broad	0.5 - 7 keV	2.3 keV
Soft	0.5 - 1.2 keV	0.92 keV
Medium	1.2 - 2.0 keV	1.56 keV
Hard	2.0 - 7.0 keV	3.8 keV

Table 2: ACIS source detection energy bands and effective energies

The images shown below (c.f. Figure 6) contain a diffuse emission at the center and a number of spread out discrete sources. In order to create an image of the diffuse emission from M82¹⁴, the location of these discrete sources needs to be detected and removed from the flux images. To achieve this, *wavdetect*, a wavelet detection algorithm implemented within CIAO was used which creates a region file that contains information about the location, counts etc for each point source. However, there were some spurious detections due to the strong diffuse emission in the central region of M82. Such detections were modified/deleted after careful visual inspection, and a candidate point source list was obtained. The finalized discrete source regions are shown in Fig 7. The *wavdetect*

⁸<https://cxc.cfa.harvard.edu/ciao/>

⁹https://cxc.cfa.harvard.edu/ciao/ahelp/chandra_repro.html

¹⁰<https://cxc.harvard.edu/ciao/threads/acisreadcorr/>

¹¹<https://cxc.cfa.harvard.edu/ciao/ahelp/dmextract.html>

¹²The parameters used for this call are the level 2 reprocessed event files with the removed readout streaks, psfecf=0.9, psfmerge=exptime, and binsize=1.

¹³https://cxc.cfa.harvard.edu/ciao/ahelp/merge_obs.html

¹⁴https://cxc.cfa.harvard.edu/ciao/threads/diffuse_emission/index.html

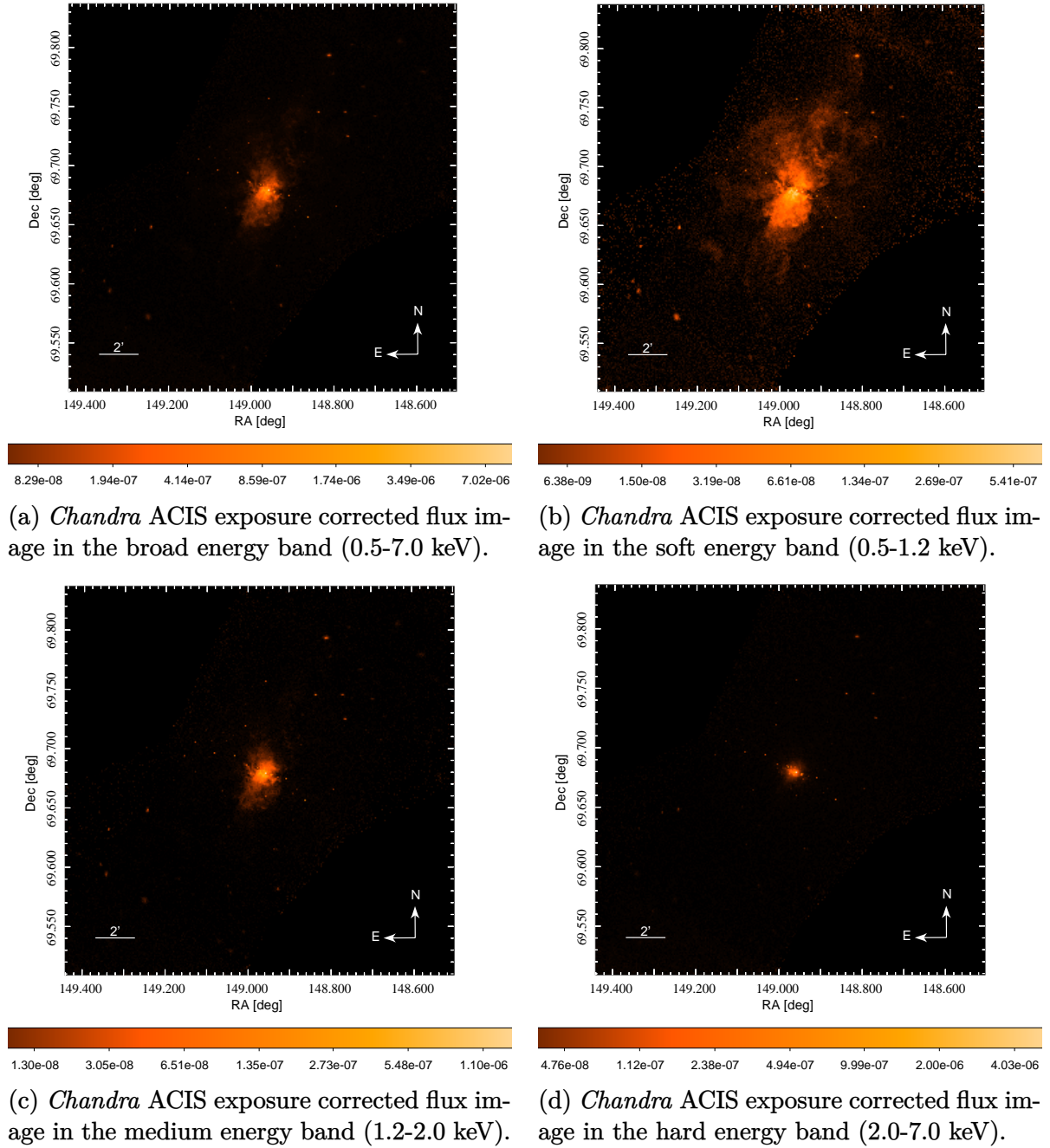


Figure 6: *Chandra* ACIS exposure corrected flux images with binsize=1 produced in different energy bands using the CIAO *merge_obs* command on the nine observations listed above in Tab 1.

command is a powerful tool that has the ability to separate closely-spaced point sources and thus was implemented here.

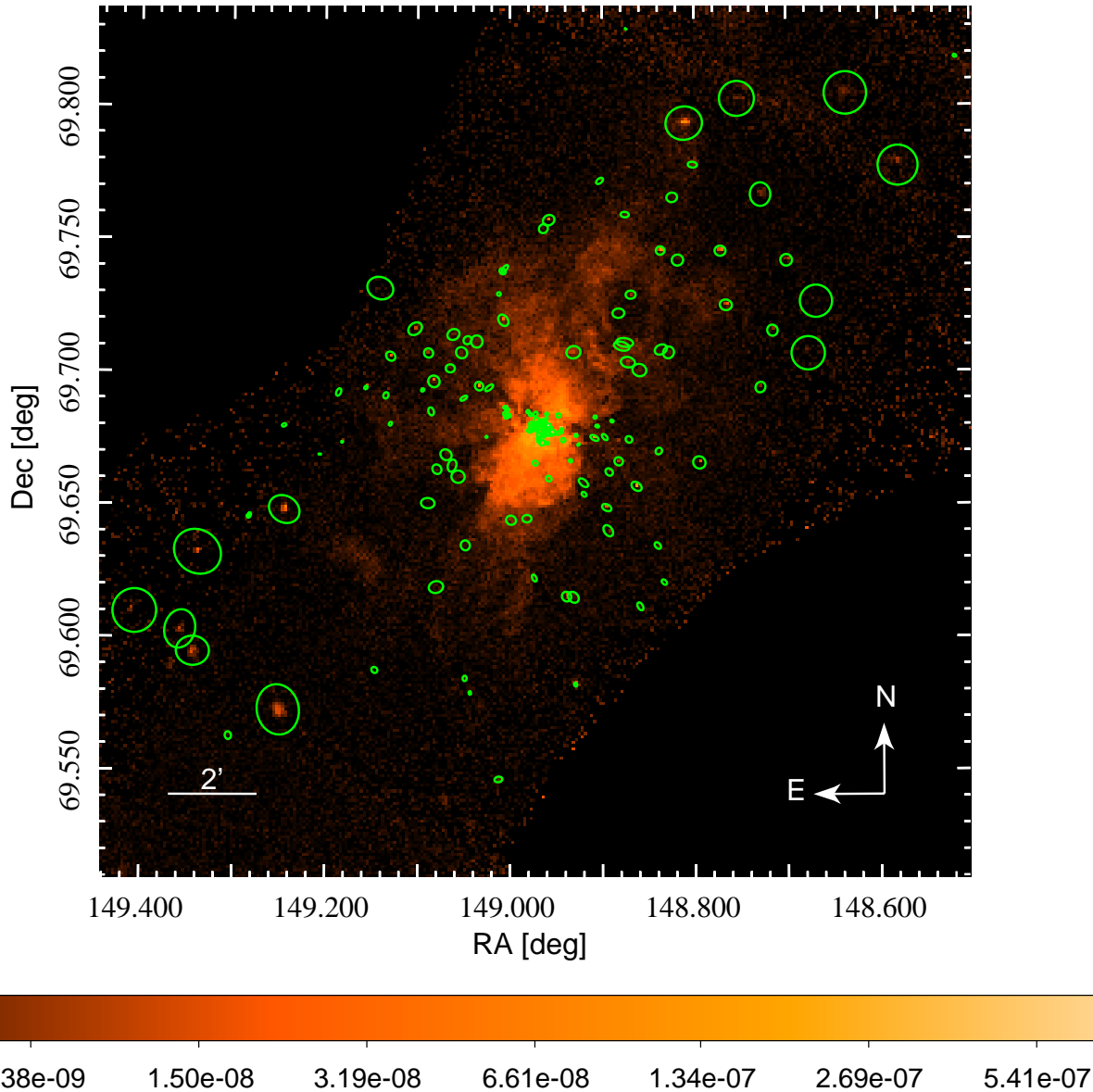


Figure 7: Adopted source regions obtained from running *wavdetect* and edited manually, shown here with green circles on the *Chandra* ACIS exposure corrected flux image in the soft energy band (0.5-1.2 keV).

Secondly, the CIAO *roi* tool was used to generate source and background regions from the source list. This tool reads in the position and shape of each region from the source region file and creates source and background regions for each non-overlapping source

region. Overlapping source regions are treated as a single source region. Background regions are co-located at the source position with a radius covering the source region. Source from another region that fall into the background for a different region are excluded from that background. These source and background regions are in-turn utilized to execute the *dmfilth* command that replaces pixel values in source regions of the image with values interpolated from the background regions. This was done for all the flux images shown in Fig 6 resulting in images containing the diffuse emission without the discrete sources in all four (broad, soft, medium, hard) energy bands. The diffuse images can further be smoothed by running the *aconvolve* command. The kernel specification used to execute this command was a Gaussian with parameters (2, 5, 1, 7, 7) representing 2 dimension, extending to 5 sigma in size in each direction, normalized to 1, and has a sigma of 7 pixels along each axis. The convolution method used was FFT (Fast-Fourier Transform). It is also possible to create an exposure-corrected image by incorporating the exposure map that was created by *merge_obs*. This can be achieved by the CIAO command *dmimgcalc* which divides the unsmoothed diffuse image by the exposure map. This step will not make a big difference unless there are significant exposure variations across the field. Fig 9a shows a *Chandra* ACIS exposure-corrected smoothed diffuse image in the broad band for M82 and Fig 9b shows the *Chandra* ACIS exposure-corrected smoothed diffuse emission in RGB. From the RGB image, one can see that the emission coming from the regions away from the central starbursting core appear to be in soft X-rays but hard emission is also observed closer to the center. The main purpose for creating this point-source free emission is to precisely analyse the chemical composition and the thermodynamics at different radii from the starbursting core which is useful to study the physics of feedback. Furthermore, the diffuse emission image also acts as a convenient initial point in simulating such emissions for different X-ray instrumentation and at different redshifts.

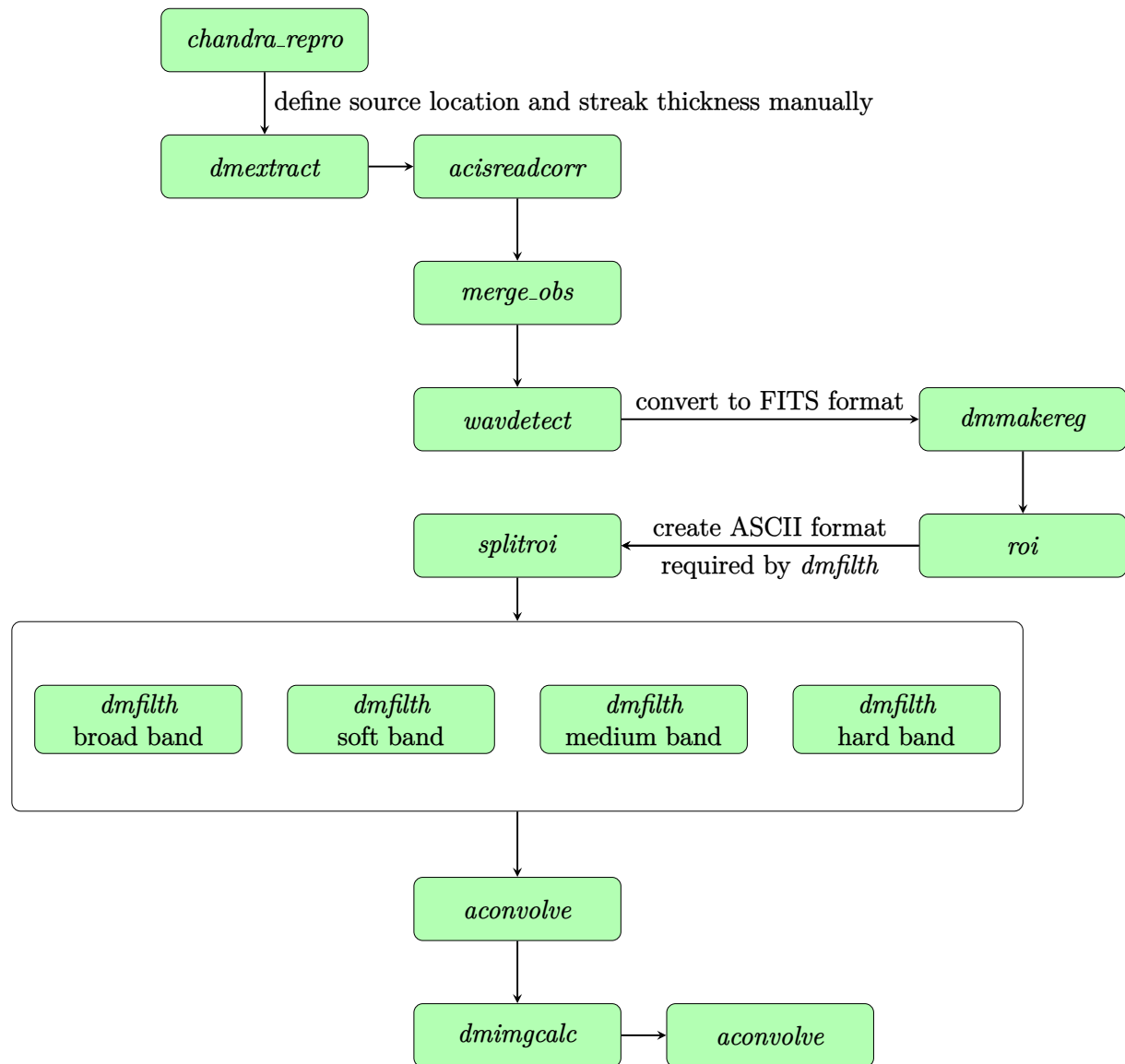
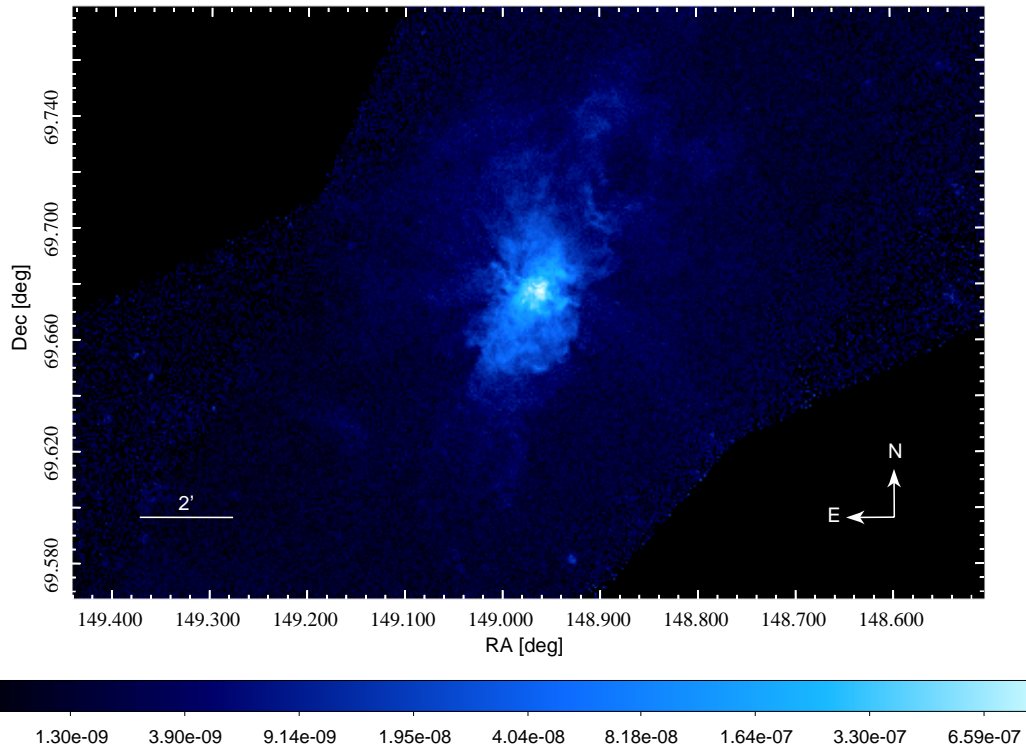
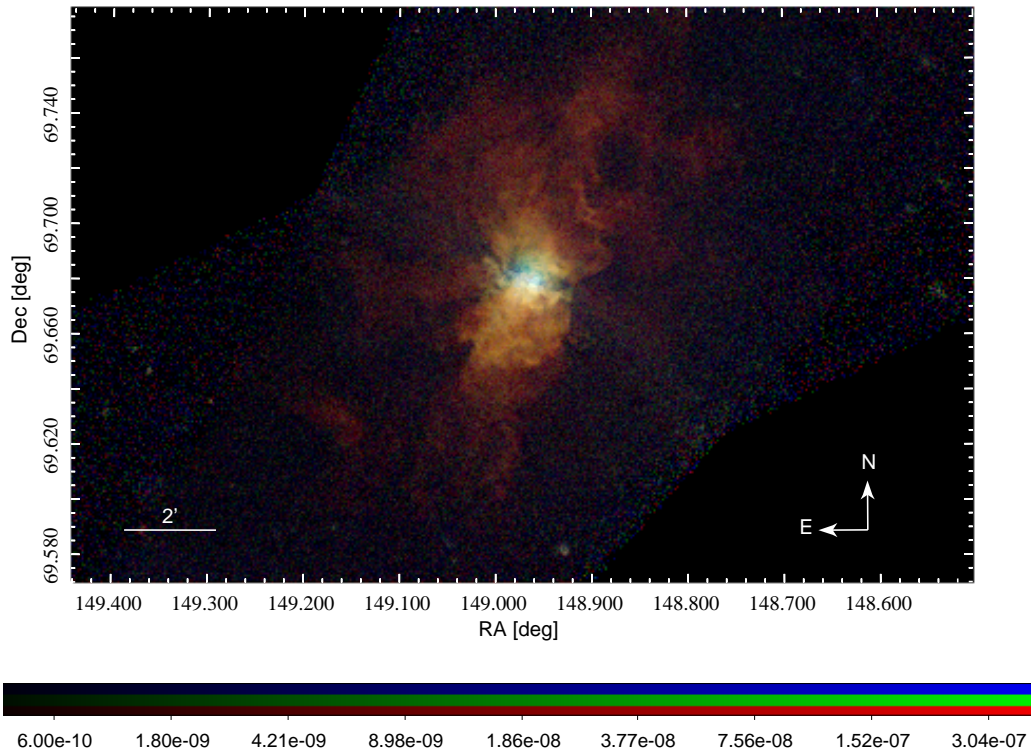


Figure 8: Steps to produce an image of the diffuse emission from *Chandra* ACIS observation.



(a) *Chandra* ACIS exposure-corrected smoothed diffuse emission from M82 with point sources removed in the broad band (0.5 - 7.0 keV)



(b) *Chandra* ACIS exposure-corrected smoothed diffuse emission with point sources removed in RGB. Red shows the exposure corrected X-ray emission in the soft band (0.5 - 1.2 keV), green shows the X-ray emission in the medium band (1.2 - 2.0 keV) and blue shows the X-ray emission in the hard band (2.0 - 7.0 keV).

Figure 9: Diffuse emission images for M82

6 Spectrum extraction and analysis for M82

Once the image of the diffuse emission is obtained, one can perform spectral analysis to study the emission at different regions in the emission. For the extraction and analysis of the spectra, only the latest six of the nine observations, (Obs ID: 10542, 10543, 10544, 10545, 10925, 11800), totaling an exposure time of 467 ks, were considered to limit the systematic differences arising from different chip configurations and temporal variations in the years between observations. The diffuse emission from M82 was divided into eleven regions (similar to [Lopez et al., 2020]) with a $0.2' \times 3.0'$ central region aligning with the M82 major axis calling it the "Disk (D)" region. Five regions each of the size $0.5' \times 3.0'$ extending on either side of the disk region were called the "North (N)" and "South (S)" regions. These regions are shown in Fig 10 and the location of their centroids is given in Tab 3.

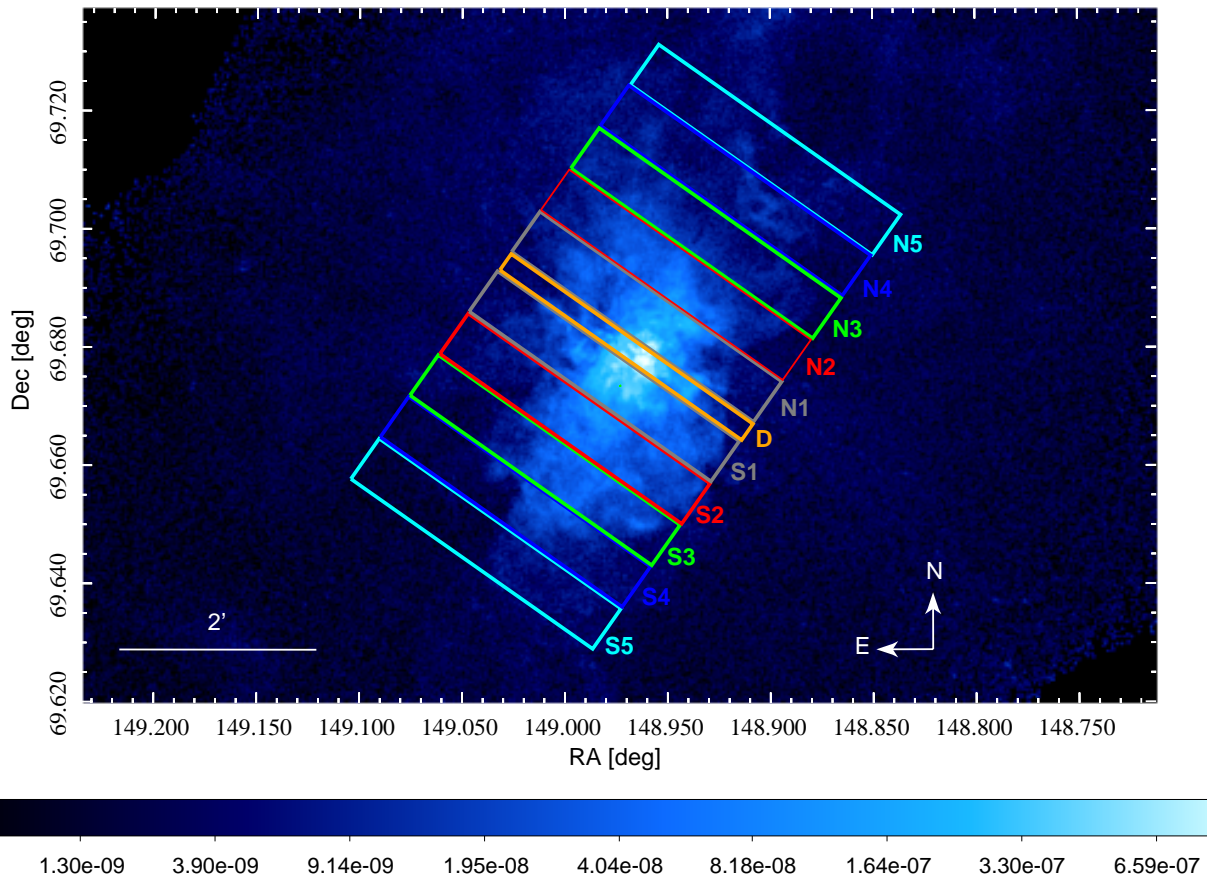


Figure 10: The different regions used for spectrum extraction from the six above-mentioned observations shown here on the *Chandra* ACIS exposure-corrected diffuse emission image in the broad band (c.f. Figure 9a)

For spectrum extraction in CIAO, background regions were carefully adopted as emission-

Region	RA [deg]	Dec [deg]
N5	148.9021583	69.7135114
N4	148.9172900	69.7064581
N3	148.9317454	69.6994028
N2	148.9459033	69.6923583
N1	148.9596717	69.6852794
D	148.9700538	69.6801556
S1	148.9808683	69.6751567
S2	148.9959467	69.6680300
S3	149.0101692	69.6606842
S4	149.0245733	69.6536389
S5	149.0384300	69.6462506

Table 3: Location of the centroids of the specified regions in Fig 10.

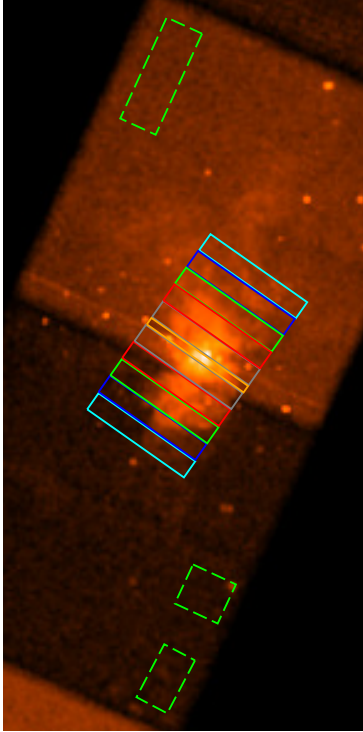
free regions from the same chip on which the source region lies. For ObsIDs 10542 and 10543, seven of these regions (N1-N5, D, S1) fell on the S3 chip while the remainder of the regions (S2-S5) fell on the S2 chip. Therefore, a background from the edge of the S3 chip was utilized to extract spectra for regions (N1-N5, D, S1) and similarly a background from the edge of the S2 chip was adopted for spectrum extraction for regions (S2-S5). For ObsIDs 10544, 10545, 10925, and 11800, all the source regions lie on the same chip and thus the background regions were defined on the edge of the same chip. The adopted background regions are shown in Fig 11.

The candidate point source list obtained after running *wavdetect* in the previous step is used to remove the discrete sources from all of these six observation IDs. The spectra for the region under investigation was then extracted by running the CIAO command *speextract*¹⁵ on each of these observations individually by using the appropriate background for the source region of interest. This step resulted in six different spectra for each of the eleven diffuse emission regions. The spectra for each region were combined together using the CIAO command *combine_spectra*¹⁶ and modeled using XSPEC Version 12.12.0¹⁷. The combined spectra were then grouped and binned together using XSPEC command *grppha* with a binning factor of 30. The obtained spectra for the different regions are shown in Fig 12. Emission lines for metals such as Ne, Mg, Si, S, Ar, Ca, and Fe are observed and the prominent emission lines are labeled for the disk region. Among these lines, two peaks at $\approx 6.38 \pm 0.04$ keV and $\approx 6.70 \pm 0.02$ keV corresponding to Fe XXV are observed (based on a Gaussian fit to the features, c.f. Figure 13), for the disk region but not for the other regions in the outflow. This is consistent with the findings of [Strickland and Heckman, 2007] suggesting this extends < 100 pc along the

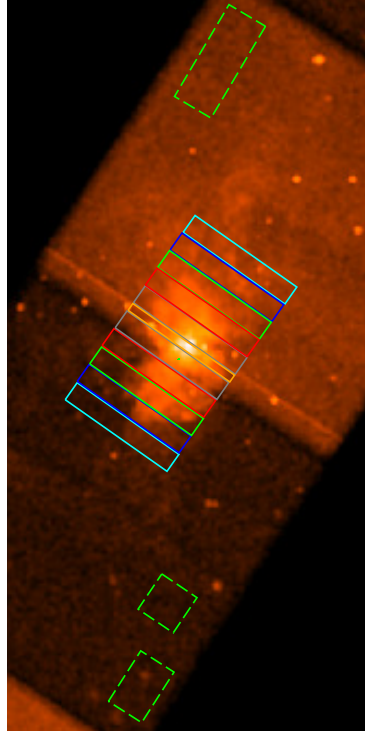
¹⁵<https://cxc.cfa.harvard.edu/ciao/threads/extended/>

¹⁶https://cxc.cfa.harvard.edu/ciao/ahelp/combine_spectra.html

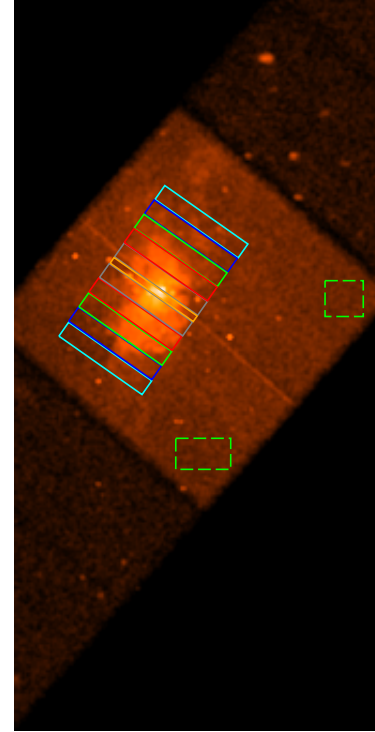
¹⁷<https://heasarc.gsfc.nasa.gov/xanadu/xspec/manual/node1.html>



(a) *Chandra* ACIS image of Obs ID **10542** (bin-size=4) with source regions in the center covering the diffuse emission and background source-free regions given in green at the edge of the chips. For source regions (N1-N5, D, and S1), the background region was accepted from the same chip given in top left. For source regions (S2-S5), the background regions used for spectral analysis are given in the bottom right.



(b) *Chandra* ACIS image of Obs ID **10543** (bin-size=4) with source regions in the center covering the diffuse emission and background source-free regions given in green at the edge of the chips. For source regions (N1-N5, D, and S1), the background region was accepted from the same chip given in top left. For source regions (S2-S5), the background regions used for spectral analysis are given in the bottom right.

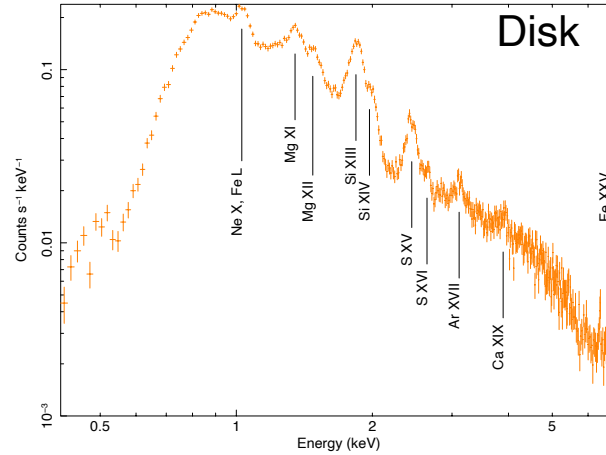


(c) *Chandra* ACIS image of Obs ID **10544** (bin-size=2) with source regions in the center covering the diffuse emission and background source-free regions given in green at the edge of the chips. Since all the source regions fall on the same chip, the same background region was used for spectral analysis. This was also the case for ObsIDs 10545, 10925, and 11800.

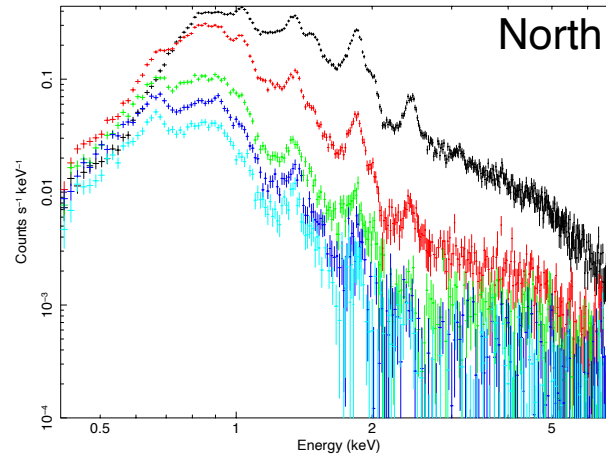
Figure 11: Source and background regions used for spectrum extraction for different observations.

M82 minor axis. Moreover, O VIII line expected at ≈ 0.65 keV was not observed for the central regions (D, N1, S1) due to the high intrinsic hydrogen absorption in M82 ($N_{\text{H}}^{\text{M82}} = 3.28^{+0.38}_{-0.33} \times 10^{21} \text{cm}^{-2}$) (Tab 5). The emission lines for Ar, Ca, and Fe seem to fade

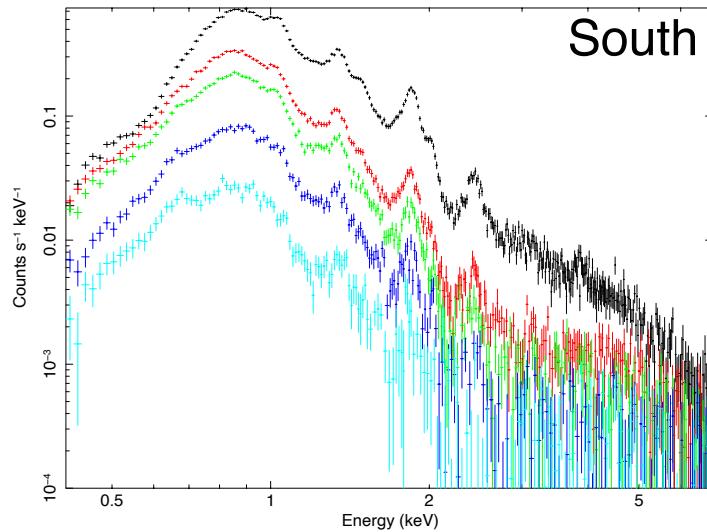
off significantly with also a reduction in hard X-ray counts as we move away from the disk region (N1 and S1 being [0.4] kpc away from the disk and every subsequent region being [0.5] kpc away from the adjacent region) suggesting metallicity and temperature variabilities in the outflowing gas.



(a) Combined *Chandra* ACIS spectrum for the disk region with the prominent emission lines labeled. O VIII (at ≈ 0.65 keV) is not detected here because of the high intrinsic column density of $N_{\text{H}}^{\text{M82}} = (3.28 \pm 0.3) \times 10^{21} \text{ cm}^{-2}$ Tab 5.



(b) Combined *Chandra* ACIS spectra extracted for the North regions. Black spectrum corresponds to region N1, red corresponds to N2, green corresponds to N3, blue corresponds to N4, and cyan corresponds to N5.



(c) Combined *Chandra* ACIS spectra extracted for the South regions. Black spectrum corresponds to region S1, red corresponds to S2, green corresponds to S3, blue corresponds to S4, and cyan corresponds to S5.

Figure 12: Extracted *Chandra* ACIS spectra for the eleven different regions.

7 Spectral fitting

One can now develop a good fitting model for the generated spectra to obtain spectral parameters like element abundances and thermal plasma temperatures in the different regions of the outflow. The grouped spectra for the individual regions were fit by using a combination of various Xspec models. The multiplicative models implemented include `const`, `tbabs`, `tbvarabs` and additive models `vnei` (unlike [Lopez et al., 2020] where the `vapex` model was implemented), `vacx`, and `powerlaw` were used. A brief description of each of the models implemented is as follows:

- **const:** This is an energy-independent multiplicative factor that was allowed to vary in the fitting. This factor accounts for the slight changes in the flux/emission measure between the observations.
- **tbabs:** This component accounts for the hydrogen column density and the Galactic absorption in the direction of M82. The parameter value was frozen at $N_{\text{H}} = 0.04 \times 10^{22} \text{cm}^{-2}$ ([Lopez et al., 2020] and references therein).

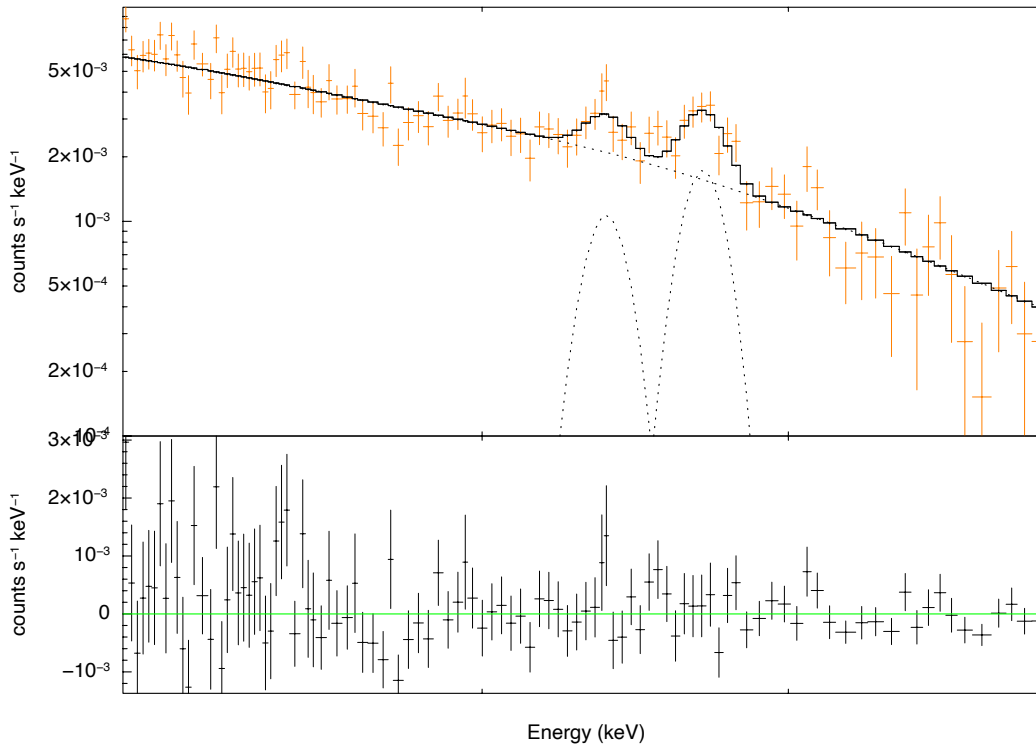


Figure 13: Gaussian fit to the Fe XXV line in the 5 – 8 keV energy range. Fitting model: Bremsstrahlung + Gaussian + Gaussian with $\chi^2/\text{d.o.f} = 101/98$.

- **tbvarabs:** This component accounts for M82’s intrinsic absorption $N_{\text{H}}^{\text{M82}}$ and was allowed to vary. It additionally allows for varying elemental abundances which in this case were set to solar abundances Z_{\odot} ([Lopez et al., 2020] and references therein).
- **vnei:** This is the non-equilibrium ionization collisional plasma model. It has parameters accounting for the plasma temperature, hydrogen abundance, abundances for He, C, N, O, Ne, Mg, Si, S, Ar, Ca, Fe, Ni with respect to solar abundances. The abundances for metals with observed emission lines in the spectra were allowed to vary and the remaining abundances were set to solar abundances Z_{\odot} .
- **vacx:** The AtomDB charge exchange (CX) model component vacx^{18} was included to

¹⁸This is not inherently an Xspec model but can be externally installed into Xspec. More information on this model can be found at http://www.atomdb.org/CX/acx_0.6.0.pdf

account for the line emission that is produced when positive ions capture electrons from neutral material. Previous studies of *XMM-Newton* RGS data demonstrate that 25% of the 0.4 – 2.0 keV flux [Zhang et al., 2014] and 50% of the O VII, Ne IX, and Mg XI flux originates from CX [Liu et al., 2011] and therefore the vacx component could not be neglected. The FracHe0 parameter of this component, which accounts for the fraction of neutral Helium in the plasma, was frozen to the default value of 0.090909.

- **powerlaw:** This is a simple photon power law of the form $A(E) = KE^{-\Gamma}$, where Γ is the photon index of the power law (dimensionless), and K is the norm in units of photons/keV/cm²/s at 1 keV. This is used to account for the emission due to Compton scattering.

All the additive models used for the fitting were used together with the multiplicative components (const * tbabs * tbvarabs). The observed diffuse emission has both thermal and non-thermal components. The thermal emission originates mostly from the interaction of the hot, low-density outflowing galactic winds powered by SN explosions/stellar winds from young stars and the cold, high-density ambient ISM. The non-thermal emission on the other hand, originates from the Compton scattering of the SN-accelerated, radio-emitting relativistic electrons off the FIR and CMB radiation fields. The spectral fitting began by implementing a single vnei model that resulted in large residuals in line emissions from Mg XII, Si XIV and hard X-rays. An additional thermal component (vnei) improved the fitting of the emission peaks and reduced the fit residuals. Previous studies of starburst galaxies have shown that the 0.5-10 keV spectra is best fit using one (or more) low temperature ($kT < 1$) keV component(s) plus a harder component. This hard component can either be thermal with $kT \sim 5 - 10$ keV or non thermal with $\Gamma \sim 1.5 - 2$ [Persic and Rephaeli, 2002]. Moreover, a purely thermal component implies low chemical abundances ($Z \sim 0.3 Z_{\odot}$) whereas comparable contributions from both thermal and non-thermal components would imply ($Z \sim Z_{\odot}$). Therefore, a powerlaw component was further employed to improve the fit for the hard X-ray energies (> 3 keV) as an additional vnei component did not significantly improve the fit. It is also consistent with the element abundances obtained from the vnei components being comparable to solar abundances. Powerlaw photon index $\Gamma \in [1.0, 2.0]$ were tested resulting in a best fit $\Gamma = 1.5$ and was therefore frozen at this value for all the 11 regions. A charge exchange component (vacx) was also included in the fitting for the above mentioned reasons which further improved the fitting to the spectra. This model (consisting of two thermal components, charge exchange, and powerlaw) showed the best fit for 7 of the 11 regions namely (N1-N3, S1-S4). Moreover, an additional vnei component was required for the fitting of the disk region to account for the detected Fe XXV line(s). Regions N4, N5, and S5 only include one vnei component as an additional vnei component did not significantly improve the fit. The best-fit models for all the regions are listed in Tab 4. The individual metallicities for the charge exchange (CX) and the two thermal components (vnei) were tied together. Additionally, the vacx temperature was tied with the higher of the two thermal compo-

ment's temperature. The best-fit parameters obtained using the specified fitting models are tabulated in Tab 5 along with a 90% confidence interval that was estimated using Xspec command *steppar*¹⁹. Figure 14 shows the fit curve for the disk region with the remaining fits shown in §A.

Region	Best-fit Model
N5	const * tbabs * tbvarabs * (vnei + vacx + powerlaw)
N4	const * tbabs * tbvarabs * (vnei + vacx + powerlaw)
N3	const * tbabs * tbvarabs * (vnei + vnei + vacx + powerlaw)
N2	const * tbabs * tbvarabs * (vnei + vnei + vacx + powerlaw)
N1	const * tbabs * tbvarabs * (vnei + vnei + vacx + powerlaw)
D	const * tbabs * tbvarabs * (vnei + vnei + vnei + vacx + powerlaw)
S1	const * tbabs * tbvarabs * (vnei + vnei + vacx + powerlaw)
S2	const * tbabs * tbvarabs * (vnei + vnei + vacx + powerlaw)
S3	const * tbabs * tbvarabs * (vnei + vnei + vacx + powerlaw)
S4	const * tbabs * tbvarabs * (vnei + vnei + vacx + powerlaw)
S5	const * tbabs * tbvarabs * (vnei + vacx + powerlaw)

Table 4: Best-fit models for the different regions.

Reg.	$N_{\text{H}}^{\text{M82}}$ ($\times 10^{21} \text{cm}^{-2}$)	kT_1 (keV)	kT_2 (keV)	O/O _⊙	Ne/Ne _⊙	Mg/Mg _⊙	Si/Si _⊙	S/S _⊙	Fe/Fe _⊙	$\chi^2/\text{d.o.f.}$
N5	< 0.01	0.35 ^{+0.05} _{-0.02}	---	0.55 ^{+0.18} _{-0.21}	1.05 ± 0.39	1.17 ^{+0.47} _{-0.44}	1.0	1.0	0.20 ± 0.05	176/169
N4	< 0.01	0.37 ± 0.02	---	0.60 ^{+0.20} _{-0.14}	1.21 ^{+0.38} _{-0.33}	1.10 ^{+0.33} _{-0.26}	1.0	1.0	0.20 ^{+0.05} _{-0.03}	217/190
N3	< 0.01	0.29 ^{+0.02} _{-0.03}	0.98 ± 0.04	1.84 ^{+2.91} _{-0.69}	3.39 ^{+5.43} _{-1.38}	2.82 ^{+4.53} _{-1.07}	2.13 ^{+3.23} _{-0.98}	1.0	1.65 ^{+3.02} _{-0.79}	268/214
N2	1.27 ± 0.23	0.40 ^{+0.05} _{-0.01}	0.77 ± 0.05	0.82 ^{+0.18} _{-0.14}	1.43 ± 0.34	1.26 ^{+0.23} _{-0.10}	1.20 ^{+0.21} _{-0.17}	0.91 ^{+0.28} _{-0.15}	0.37 ± 0.05	328/264
N1	3.90 ± 0.12	0.64 ^{+0.01} _{-0.02}	1.74 ^{+0.15} _{-0.11}	1.0	1.25 ^{+0.06} _{-0.09}	1.28 ^{+0.08} _{-0.11}	1.46 ^{+0.10} _{-0.13}	1.75 ^{+0.13} _{-0.16}	0.27 ± 0.02	667/383
D	3.28 ^{+0.38} _{-0.33}	0.76 ^{+0.04} _{-0.05}	5.83 ^{+3.82} _{-0.82}	1.0	1.80 ^{+1.20} _{-0.47}	3.79 ^{+1.39} _{-1.60}	6.90 ^{+3.70} _{-2.69}	15.63 ^{+9.68} _{-5.74}	1.10 ^{+0.59} _{-0.42}	457/367
S1	1.57 ± 0.14	0.66 ± 0.01	1.61 ^{+0.03} _{-0.06}	1.0	2.40 ± 0.20	1.72 ± 0.15	1.34 ^{+0.12} _{-0.08}	1.18 ^{+0.07} _{-0.11}	0.47 ^{+0.02} _{-0.04}	824/329
S2	0.39 ± 0.24	0.84 ^{+0.03} _{-0.06}	0.44 ± 0.04	0.36 ± 0.06	0.80 ^{+0.15} _{-0.13}	0.75 ± 0.11	0.61 ± 0.08	0.33 ± 0.16	0.33 ± 0.04	296/229
S3	< 0.01	0.69 ± 0.01	0.40 ^{+0.06} _{-0.09}	0.37 ^{+0.15} _{-0.08}	1.11 ± 0.24	0.80 ± 0.10	0.68 ^{+0.11} _{-0.09}	1.0	0.27 ^{+0.05} _{-0.03}	272/205
S4	0.91 ± 0.45	0.55 ^{+0.19} _{-0.05}	0.24 ^{+0.17} _{-0.02}	0.44 ^{+0.20} _{-0.12}	1.17 ^{+0.55} _{-0.34}	0.81 ^{+0.34} _{-0.21}	0.69 ^{+0.24} _{-0.17}	1.0	0.27 ^{+0.12} _{-0.07}	219/170
S5	< 0.01	0.44 ± 0.06	---	0.34 ^{+0.30} _{-0.15}	0.62 ^{+0.65} _{-0.19}	0.62 ^{+0.49} _{-0.19}	1.0	1.0	0.17 ^{+0.09} _{-0.04}	186/166

Table 5: Best-fit parameters of the tbabs and vnei components of the Xspec model described in Tab 4.

NOTE: A third vnei component not listed in this table was added to the region D model to account for the Fe XXV line. The best-fit temperature of that component was $kT_3 = 0.30^{+0.10}_{-0.06}$ keV.

¹⁹<https://heasarc.gsfc.nasa.gov/xanadu/xspec/manual/node86.html>

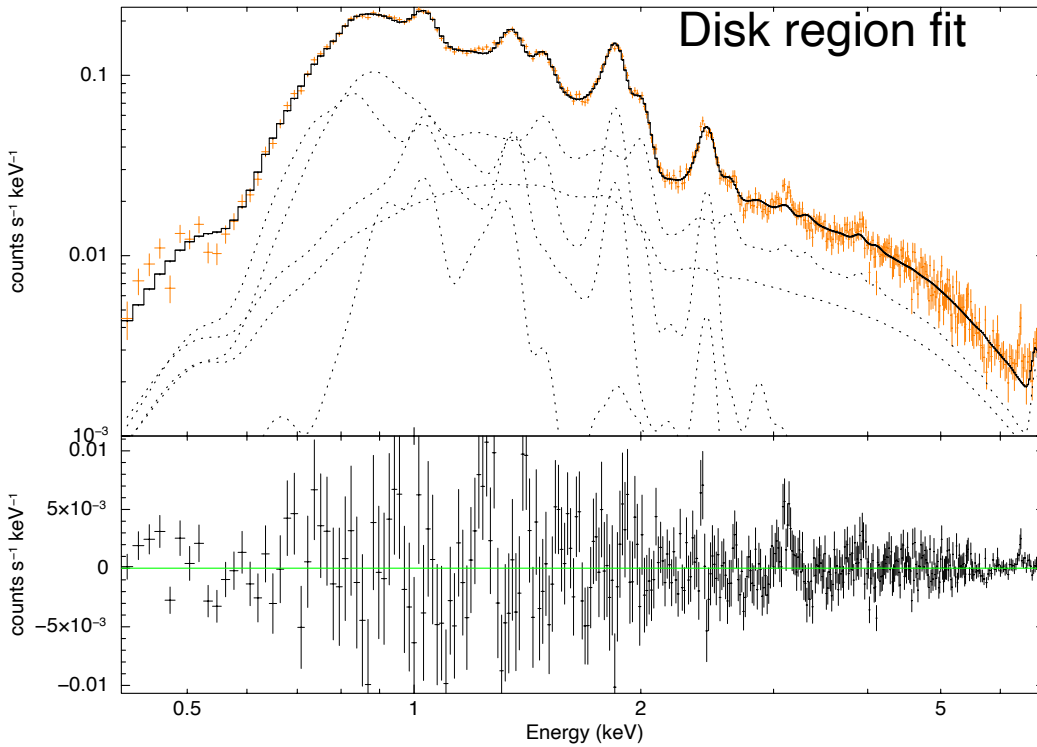


Figure 14: The above figure shows the fit curve for the central disk region. The orange markers denote the data points for the disk spectrum same as Figure 12a. The solid black line is the fit curve to the spectrum. The dashed black curves are the individual Xspec model components, in this case, (vnei+vnei+vnei+vacx+powerlaw). The bottom plot shows the residuals in the fit to the data.

8 Simulation modeling

Based on the spectra and fitting models obtained from the *Chandra* observations of the diffuse emission for different regions, models for the *Athena* simulation were developed by first dividing the total energy band (0.4-6.9 keV) into five smaller bands as follows:

Band	Energy range	Region of interest
Band 1	0.4 - 0.7 keV	N3, S3
Band 2	0.7 - 1.3 keV	N2, S2
Band 3	1.3 - 2.2 keV	S1
Band 4	2.2 - 3.0 keV	N1
Band 5	3.0 - 6.9 keV	D

Table 6: Energy cuts applied to different regions to create simulation files (simputs) for *Athena*.

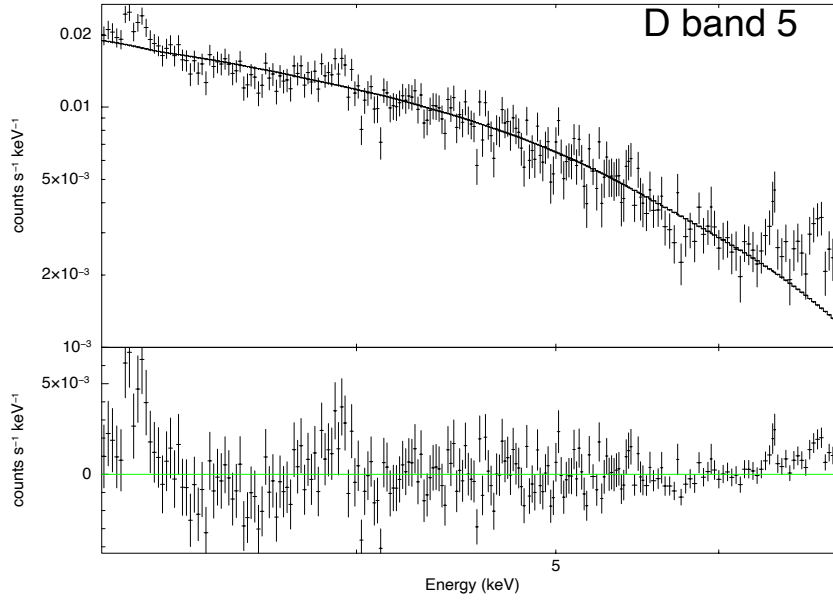
Spectrum of region D was used for the highest energy band (3.0 – 6.9 keV) as it had the best statistics in this energy range. Similarly, spectra of the next closest regions, N1 and S1, were used for the energy range 2.2 – 3.0 keV and 1.3 – 2.2 keV respectively. Energy range 0.7 – 1.3 keV was used for spectra of regions N2 and S2 and the lowest energy range 0.4 – 0.7 keV was used for regions N3 and S3 spectra. Secondly, these seven selected regions' spectra were fit individually in the new energy ranges with the same multiplicative components (const * tbabs * tbvarabs) as earlier in Sec §7. It was observed that a powerlaw component with a powerlaw index $\Gamma = 1.7$ showed the best fit for the spectrum of region D in band 5 with 361/215 reduced χ^2 /d.o.f. statistics. Best-fits for spectra of regions N1 in band 4 and N3, S3 in band 1 were obtained using one thermal component due to a single emission line in these energies. The elemental abundances of Si, and S for the N1 region spectrum and O abundance for regions N3 and S3 spectra were allowed to vary with the remaining parameters set to solar abundances Z_{\odot} . Finally, spectra of regions S1 in band 3 and N2, S2 in band 2 required two thermal components for the best fit due to multiple emission lines. The two vnei model metallic abundances were tied together and the elemental abundances of Mg, and Si for the S1 region spectrum and Ne abundance for spectra of regions N2 and S2 were allowed to vary with the remaining parameters set to solar abundances Z_{\odot} . The best fit plots for individual region's spectra in the new energy bands are shown in Figure 15 with best-fit parameters in Tab 7,8, and the combined spectra for these regions is shown in Figure 16.

Region	$N_{\text{H}}^{\text{M82}}$ ($\times 10^{21} \text{cm}^{-2}$)	kT (keV)	O/ O_{\odot}	Si/ Si_{\odot}	S/ S_{\odot}	χ^2 /d.o.f.
N1	$25.47^{+7.93}_{-7.41}$	$1.03^{+0.07}_{-0.04}$	1.0	$1.38^{+0.62}_{-0.50}$	$0.66^{+0.09}_{-0.07}$	63/47
N3	$0.66^{+0.5}_{-0.4}$	$0.25^{+0.03}_{-0.02}$	$0.68^{+0.29}_{-0.16}$	1.0	1.0	28/13
S3	$0.78^{+0.53}_{-0.56}$	$0.24^{+0.07}_{-0.04}$	$0.34^{+0.08}_{-0.05}$	1.0	1.0	13/13

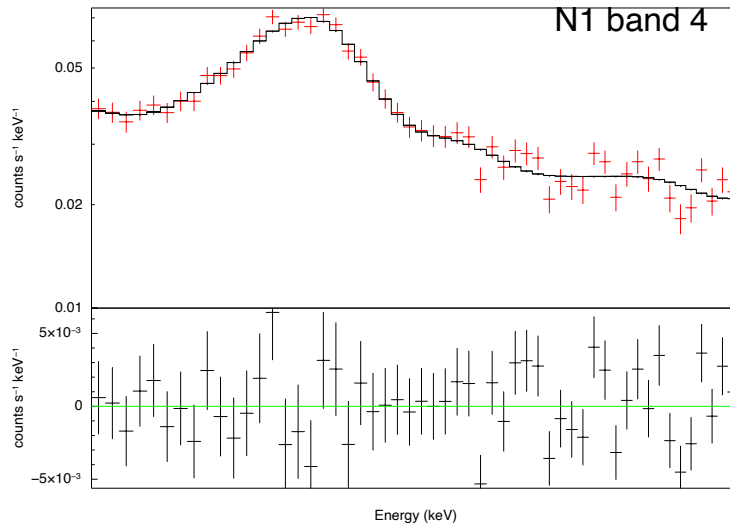
Table 7: Best-fit parameters for regions fitted with a single vnei model in the new energy bands.

Region	$N_{\text{H}}^{\text{M82}}$ ($\times 10^{21} \text{cm}^{-2}$)	kT_1 (keV)	kT_2 (keV)	Ne/Ne $_{\odot}$	Mg/Mg $_{\odot}$	Si/Si $_{\odot}$	$\chi^2/\text{d.o.f.}$
S1	2.06 ± 1.5	$0.93^{+0.19}_{-0.29}$	$2.18^{+2.82}_{-0.44}$	1.0	$1.28^{+0.42}_{-0.33}$	$1.23^{+0.67}_{-0.28}$	50/50
N2	$3.80^{+0.50}_{-0.36}$	0.77 ± 0.04	0.21 ± 0.01	$0.63^{+0.18}_{-0.16}$	1.0	1.0	118/31
S2	$3.06^{+0.37}_{-0.32}$	$0.79^{+0.03}_{-0.04}$	$0.23^{+0.02}_{-0.01}$	$0.66^{+0.15}_{-0.20}$	1.0	1.0	92/31

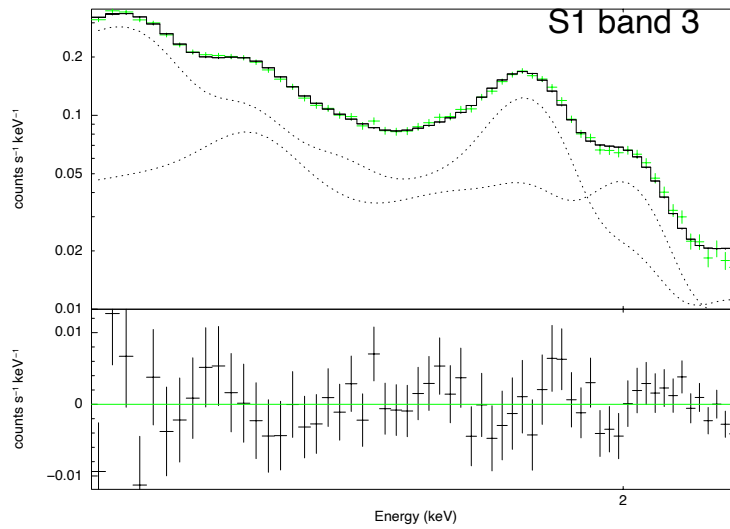
Table 8: Best-fit parameters for regions fitted with two vnei models in the new energy bands.



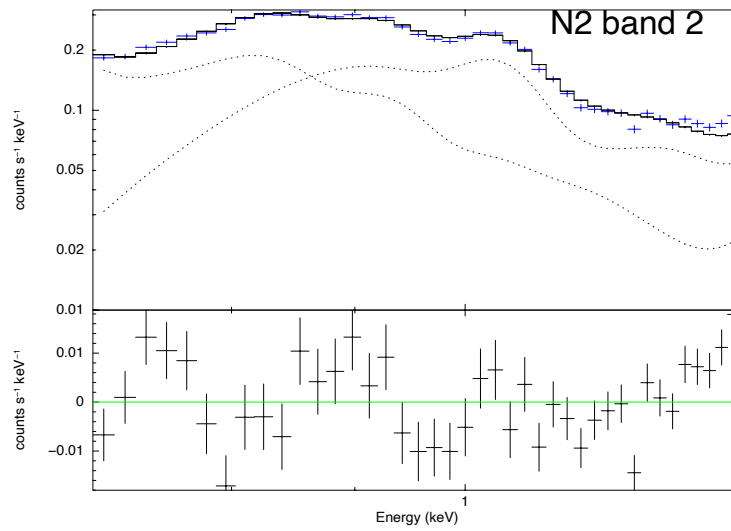
(a) Spectral fit for D region in energy band 3.0 - 6.9 keV. Fitting model: $\text{const} * \text{tbabs} * \text{tbvarabs} * \text{powerlaw}$.



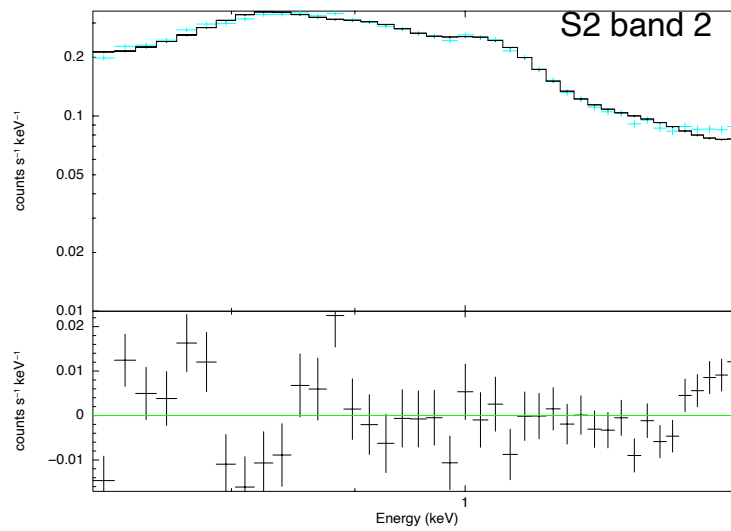
(b) Spectral fit for N1 region in energy band 2.2 - 3.0 keV. Fitting model: $\text{const} * \text{tbabs} * \text{tbvarabs} * \text{vnei}$.



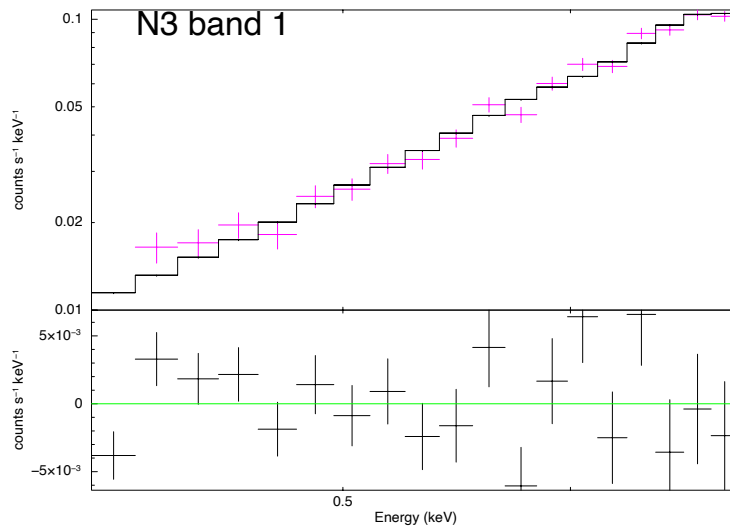
(c) Spectral fit for S1 region in energy band 1.3 - 2.2 keV. Fitting model: $\text{const} * \text{tbabs} * \text{tbvarabs} * (\text{vnei} + \text{vnei})$.



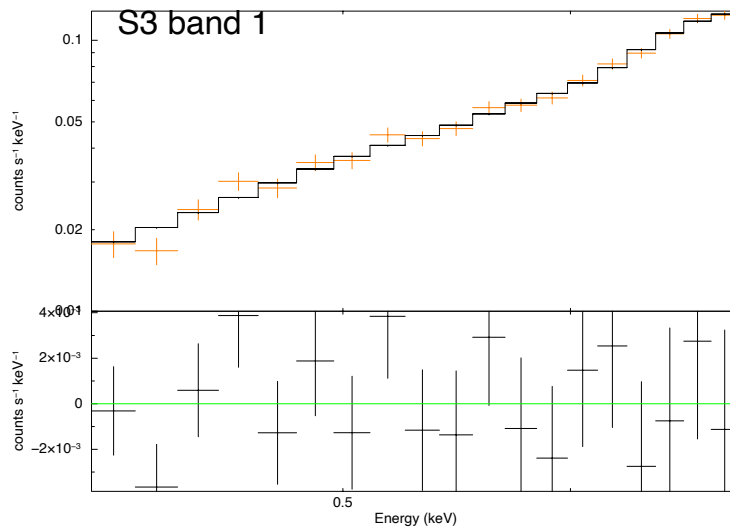
(d) Spectral fit for N2 region in energy band 0.7 - 1.3 keV. Fitting model: $\text{const} * \text{tbabs} * \text{tbvarabs} * (\text{vnei} + \text{vnei})$.



(e) Spectral fit for S2 region in energy band 0.7 - 1.3 keV. Fitting model: $\text{const} * \text{tbabs} * \text{tbvarabs} * (\text{vnei} + \text{vnei})$.



(f) Spectral fit for N3 region in energy band 0.4 - 0.7 keV. Fitting model: $\text{const} * \text{tbabs} * \text{tbvarabs} * \text{vnei}$.



(g) Spectral fit for S3 region in energy band 0.4 - 0.7 keV. Fitting model: $\text{const} * \text{tbabs} * \text{tbvarabs} * \text{vnei}$.

Figure 15: Best-fit plots for the regions utilized for the purposes of simulations in the developed sub-energy bands.

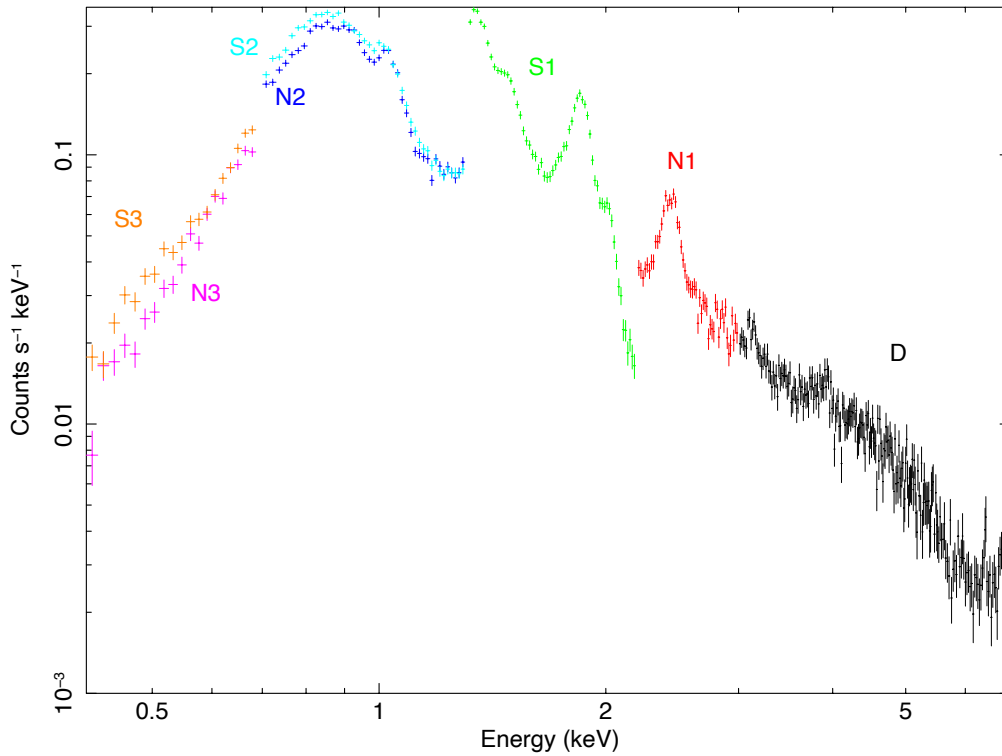


Figure 16: Combined spectra for the 7 utilized regions in the 5 sub-energy bands.

Now `simputfile` files can be created with the clearly defined regions and the energies, using the command `simputfile`. The input parameters used were the location (RA, Dec) defined by the pointing direction of the satellite (centroid of region D), the minimum and maximum energy of the specific region (E_{\min} , E_{\max}), the lower and upper bound of the spectrum ($E_{\text{low}} = 0.2$ keV, $E_{\text{max}} = 10.0$ keV), the Xspec spectral fitting model, the source flux (`srcFlux`) which was obtained using Xspec command `flux` for each region given in Tab 9, and an imagefile (the diffuse emission images developed from *Chandra* data in different energy bands §B). An example `simput` call for the disk region is as follows:

```
simputfile \
RA=148.9700538 Dec=69.6801556 \
srcFlux=6.8373e-13 \
Elow=0.2 Eup=10 \
XSPECFile=D_band5.xcm \
Emin=3.0 Emax=6.9 \
ImageFile=diffuse_hard.fits \
```

`Simput=D_band5.fits`

The RA and Dec is in degrees, the srcFlux is in units of erg/s/cm², Elow, Eup, Emin, and Emax are in units of keV, XSPECFile is the spectral model for the region in the particular energy range (in this example “Disk” in range 3.0 - 6.9 keV and hence powerlaw), Imagefile is the diffuse emission image (diffuse emission image in the hard band for region D) and the name of the output file is defined using the Simput parameter. This was done for all the 7 regions of interest resulting in 7 simput files which were combined using simput tool *simputmerge* into a single FITS file called “M82_diffuse.fits”. An attitude file was further created to avoid imprinting the gaps in between the chips for an exposure time of 100ks using simput command:

```
attgen_dither \  
Attitude=M82_100ks.fits \  
Amplitude=0.08 \  
SrcRA=148.9700538 \  
SrcDec=69.6801556 \  
Exposure=100000
```

The above call creates a Lissajous dithering pattern (Figure 17) with a given amplitude (in degrees), centered around SrcRA and SrcDEC (in degrees) for a given exposure time in seconds. The output file name is defined using the Attitude parameter.

Region	Energy band	Flux in ergs/s/cm ²
D	Band 5	6.8373×10^{-13}
N1	Band 4	3.2976×10^{-13}
S1	Band 3	5.9587×10^{-13}
N2	Band 2	4.2808×10^{-13}
S2	Band 2	5.9516×10^{-13}
N3	Band 1	8.8158×10^{-14}
S3	Band 1	1.6018×10^{-13}

Table 9: Srcflux, obtained using Xspec command *flux*, used for *simputfile* call for the different regions and respective energy bands.

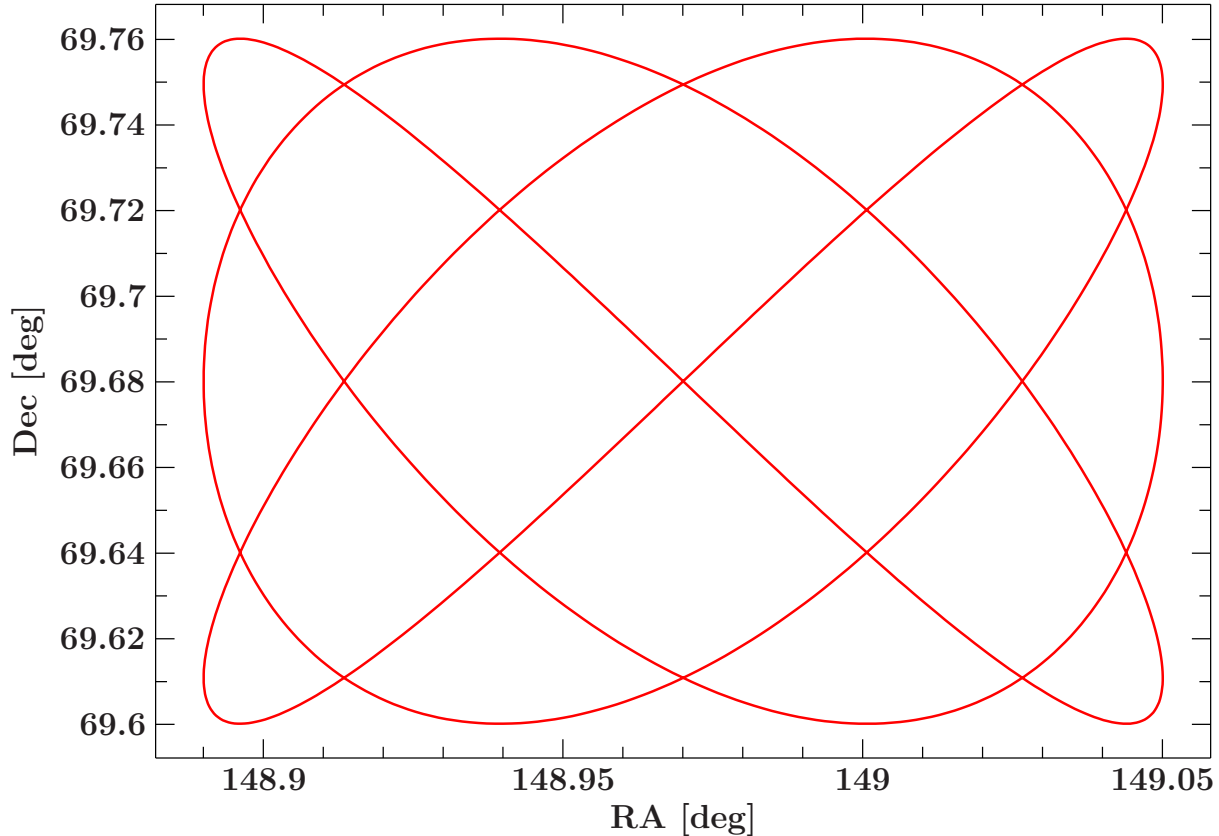


Figure 17: The pointing of satellite in RA and Dec as specified by the attitude file generated for an exposure of 100ks.

The different instrument information is stored in XML files. For *athenawfisim*, this required information is stored in 4 different files called `ld_wfi_10arcsecHEW_ff_chip[0,1,2,3].xml`. The given configuration contains 4 (512 x 512) chips, with an optical blocking filter and a time resolution of $5018\mu\text{s}$ assuming a $10''$ HEW. Now using the merged simput file, the attitude file and the XML files, a simulation for the *Athena* WFI instrument can be performed using SIXTE call as follows:

```
athenawfisim \
Attitude=M82_100ks.fits \
Prefix=sim_ \
XMLFile0=xml[0] XMLFile1=xml[1] XMLFile2=xml[2] XMLFile3=xml[3] \
Simput=M82_diffuse.fits \
EvtFile=M82_evt.fits \
Exposure=100000 \
clobber=yes
```

The parameters `Attitude` and `Simput` takes the attitude file and the merged file as inputs respectively. The output of this simulation is an event file for each of the 4 chips defined

using the parameter `EvtFile`. This can be combined to a single event file using the FTOOL *ftmerge*. Now this combined event file is used to create an image of the full WFI detector with the SIXTE tool *imgev* as follows:

```
imgev \
EvtFile=sim_M82_evt.fits \
Image=sim_M82_img.fits \
CoordinateSystem=0 Projection=TAN \
NAXIS1=1063 NAXIS2=1063 CUNIT1=deg CUNIT2=deg \
CRVAL1=148.9700538 CRVAL2=69.6801556 CRPIX1=532 CRPIX2=532 \
CDELTA1=-6.207043e-04 CDELTA2=6.207043e-04 history=true \
clobber=yes
```

The `EvtFile` parameter takes the merged event file as input, `NAXIS1` and `NAXIS2` accommodate the pixels of the 4 chips (512 x 512) of the detector (with additional pixels assigned to account for the gap between the chips), `CRVAL1` and `CRVAL2` defines the aim point of the satellite in degrees corresponding to RA and Dec, `CRPIX1` and `CRPIX2` are the pixel coordinates of the detector, `CDELTA1` and `CDELTA2` are the pixel size in degrees and the output image file name is defined using the parameter `Image`. The image produced using a 100ks simulation for the *Athena* WFI instrument is shown in Figure 18 and Figure 19.

One can also extract spectra for desired regions from this simulated file using SIXTE tool *makespec* as follows:

```
makespec \
EvtFile=sim_M82_evt.fits \
Spectrum=D_spec.pha \
EventFilter="RA>148.962 && RA<148.977 && Dec>69.678 && Dec<69.683" \
RSPPath=${xmlmdir} clobber=yes
```

The `EvtFile` parameter is the input event file, and `Spectrum` is the output spectral file. The `EventFilter` parameter defines a square/rectangular region around the specified RA and Dec coordinates and extracts spectrum from this region. Alternatively, `EventFilter` can also make use of a ds9 region to extract the spectra. This is done by first making the event file compatible for this purpose by using:

```
radec2xy \
EvtFile=sim_M82_evt.fits \
projection=TAN \
RefRA=148.9700538 RefDec=69.6801556
```

and replacing the `EventFilter` command in *makespec* with:

```
EventFilter= "regfilter(\"D.reg\")"
```

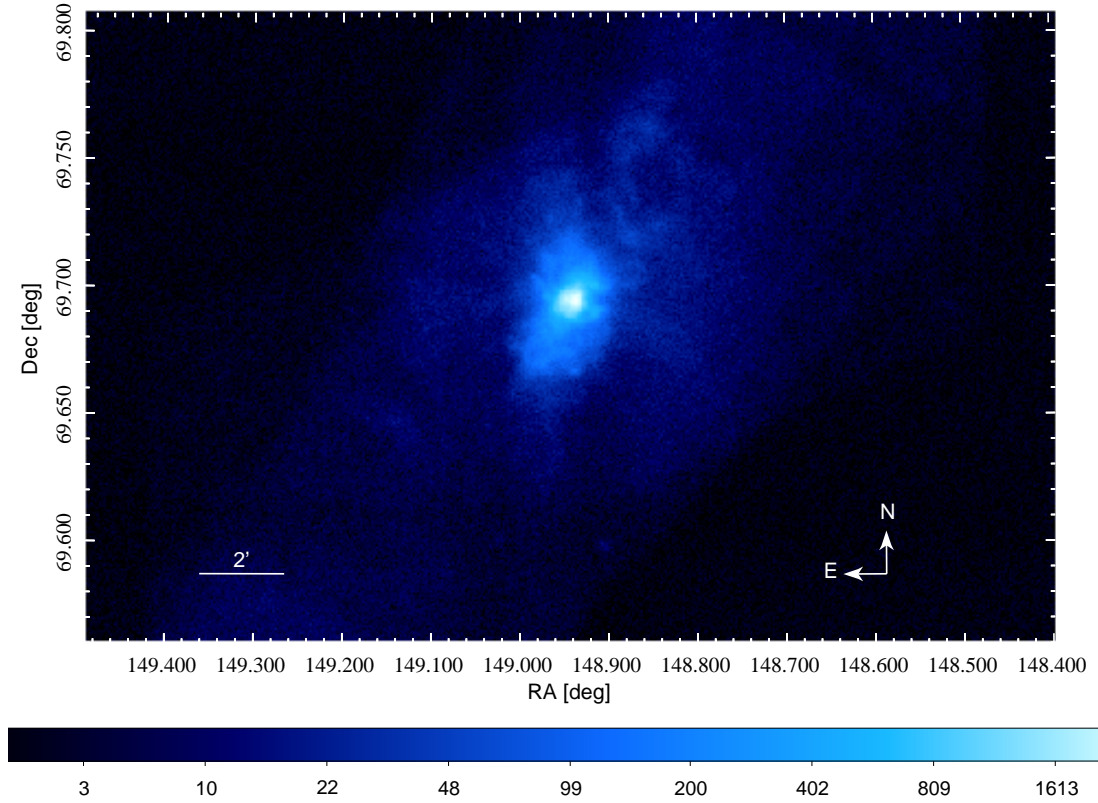


Figure 18: Diffuse emission image created for M82 in the broad energy band using a 100ks simulation of the *Athena WFI* instrument.

RefRA and RefDec in *radec2xy* are the reference RA and Dec locations which are the same as CRVAL1 and CRVAL2 used in *imgev*. The resultant spectra obtained using the ds9 defined regions on the *Chandra* diffuse emission image (10) are shown in 20.²⁰

²⁰There was a positional offset between the image obtained from the simulation and the *Chandra* image and thus the ds9 regions did not correctly overlap. Hence, they were manually shifted to align with the desired positions before the extraction of the spectra from the WFI simulation.

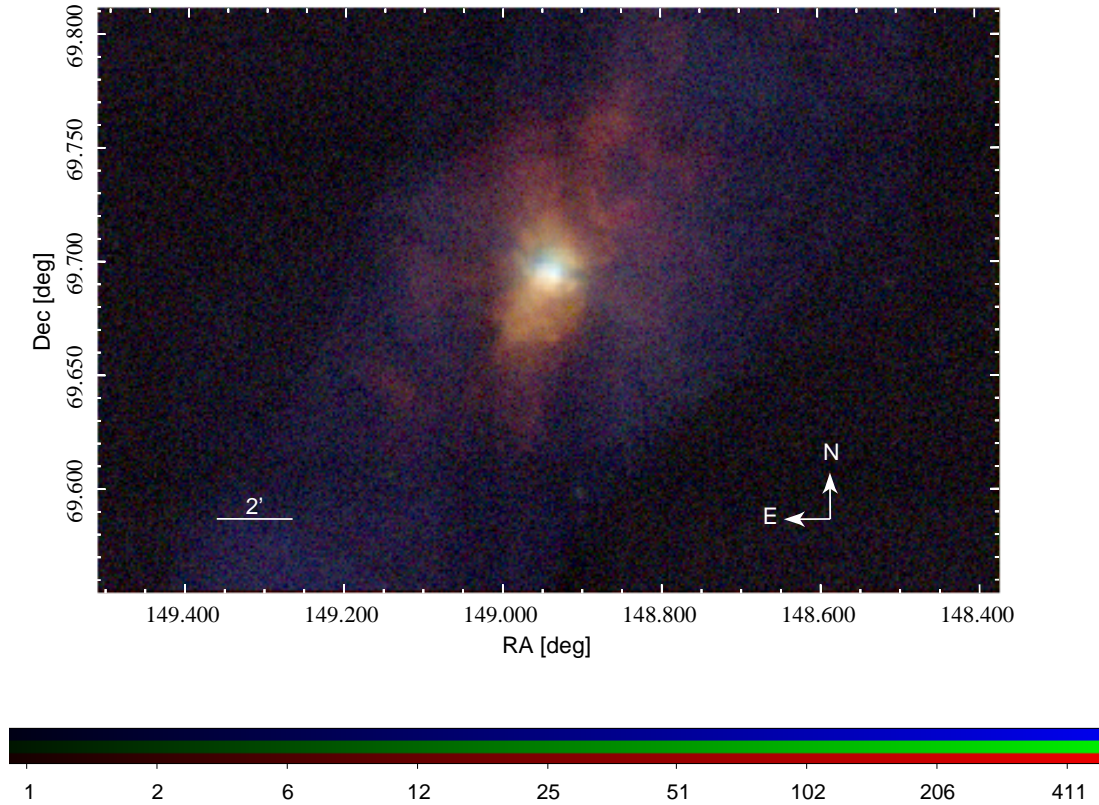
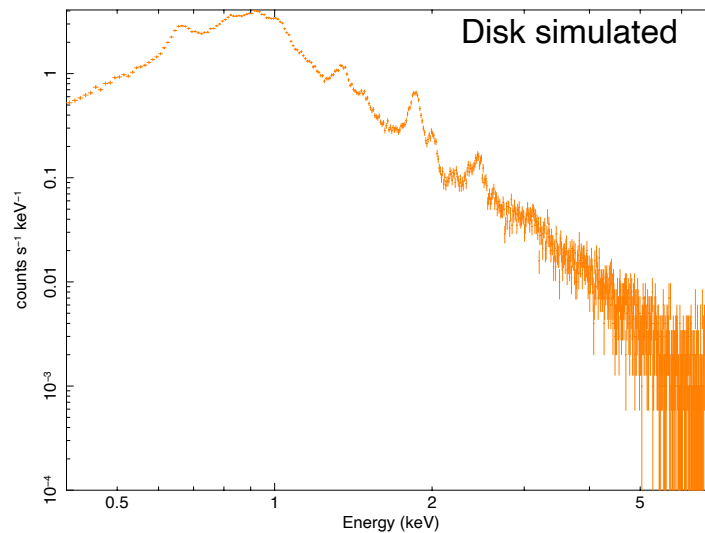
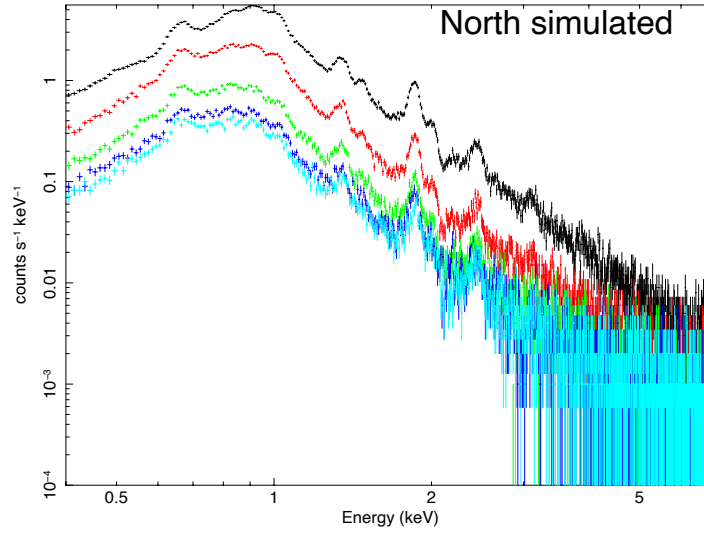


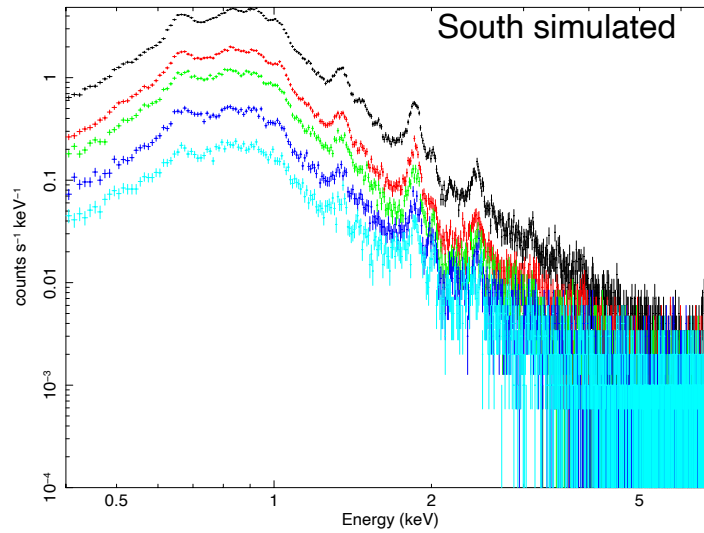
Figure 19: Diffuse emission image created for M82 in RGB using a 100ks simulation of the *Athena* WFI instrument. Red shows the X-ray emission in the soft band (0.5 – 1.2 keV), Green shows the X-ray emission in the medium band (1.2 – 2.0 keV) and Blue shows the X-ray emission in the hard band (2.0 – 7.0 keV).



(a) Spectrum obtained from the simulation for the disk region.



(b) Spectra obtained from the simulation for the north regions. Black spectrum corresponds to region N1, red corresponds to N2, green corresponds to N3, blue corresponds to N4, and cyan corresponds to N5.



(c) Spectra obtained from the simulation for the south regions. Black spectrum corresponds to region S1, red corresponds to S2, green corresponds to S3, blue corresponds to S4, and cyan corresponds to S5.

Figure 20: Extracted spectrum for the different regions obtained using the 100ks *Athena* WFI simulation.

Spectral fitting is now performed to these spectra obtained from the WFI simulation to estimate the temperature and metallicity in the different regions of the emission and to build a comparison with the values obtained from the spectra of the *Chandra* ACIS observations. We use the same fitting models as described in Tab 4. The spectral fit for the simulated disk region is shown in Figure 21. §C shows the fits for the remaining simulated spectra along with Tab 10 listing the fit parameters.

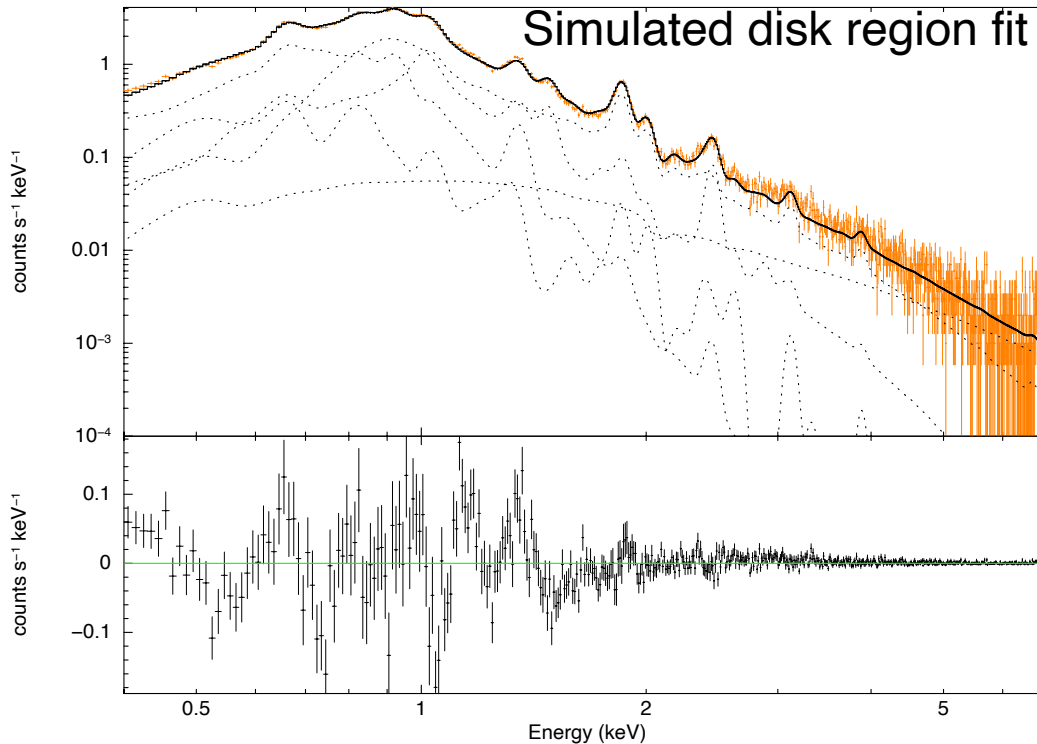


Figure 21: The above figure shows the fit curve for the spectrum of the simulated central disk region. The orange markers denote the data points for the simulated disk spectrum similar to Figure 20a. The solid black line is the fit curve to the spectrum. The dashed black curves are the individual Xspec model components, in this case, (vnei+vnei+vnei+vacx+powerlaw). The bottom plot shows the residuals in the fit to the data.

One can now re-introduce the discrete sources that were removed from the *Chandra* data, to better understand the spatial resolving capabilities of the WFI instrument and to ensure upto what redshifts the instrument is able to resolve the point sources from the diffuse emission. In order to mimic the emission from these point sources and estimate

their flux, an absorbed power-law model with a photon index $\Gamma = 1.7$, and a column density of hydrogen $N_{\text{H}} = 3 \times 10^{22} \text{cm}^{-2}$ was assumed [Chiang and Kong, 2011]. A generalized flux for this spectral model in the energy range 0.4 - 6.9 keV was obtained using Xspec command *flux* and was found to be $2.27 \times 10^{-9} \text{ ergs/s/cm}^2$. One can further obtain the count rate for the *Chandra* ACIS-S chip using PIMMS (Portable, Interactive, Multi-Mission Simulator) which was found to be $1.396 \times 10^2 \text{ counts/s}$. This count rate acts as a normalization factor to convert the generalized flux into intrinsic flux. The candidate source list that was obtained from *wavdetect* in §5 contains the number of counts for each point source and the exposure time (467 ks for the utilized data). Using this, one obtains the intrinsic flux of each source as:

$$\begin{aligned} flux &= \frac{\text{generalized flux}}{\text{normalisation}} \cdot \frac{\#\text{counts}}{\text{exposure}} \\ &= \frac{2.27 \times 10^{-9} \text{ erg/s/cm}^2}{1.396 \times 10^2 \text{ counts/s}} \cdot \frac{\#\text{counts}}{467\text{ks}}. \end{aligned}$$

Now the same steps as earlier are repeated to create simput files for each point source, merged together into a single simput file, and the *Athena* WFI simulation is performed for 100ks using two simputs, Simput1: containing information about the diffuse emission, and Simput2: containing information about the point sources. The resulting image obtained using *imgev* from this simulation is shown in Figure 22.

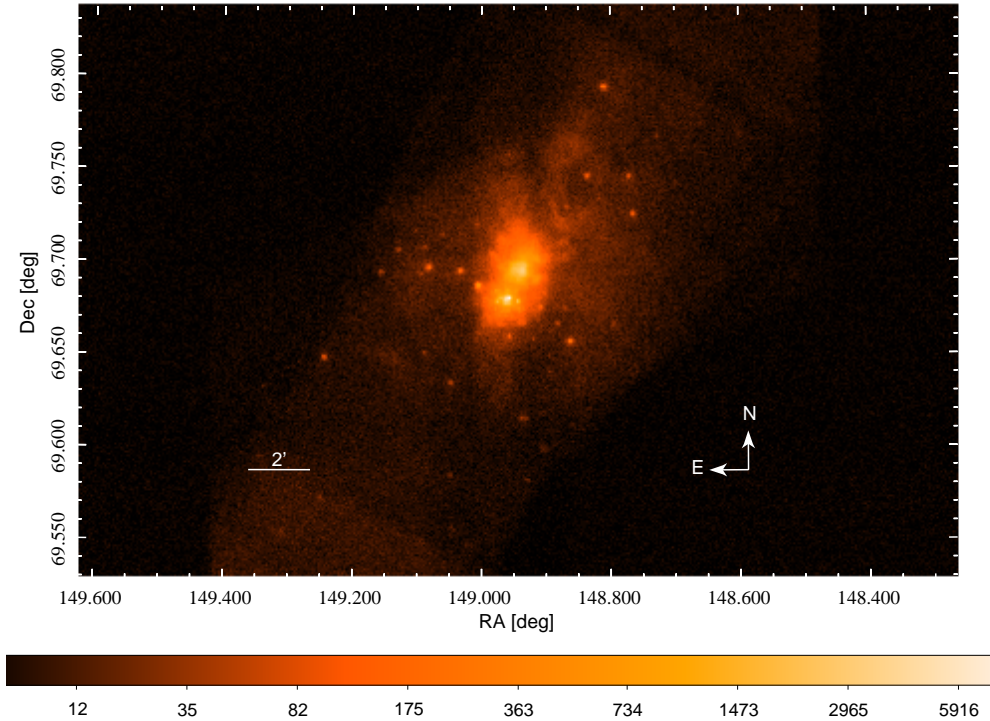


Figure 22: Simulated image of M82 in the broad energy band using a 100ks simulation of the *Athena* WFI instrument.

9 Simulations at higher red-shifts

In order to understand the spatial resolution of *Athena* WFI, *Chandra* ACIS images obtained above were projected to higher red-shifts ($z = 0.004375, 0.00875, 0.01714, 0.02571$) corresponding to distances ($d = 18$ Mpc, 36 Mpc, 72 Mpc, 108 Mpc) by assuming a constant luminosity but varying the flux and the image resolution. The fluxes for individual sources were scaled using the equation:

$$flux(z) = flux_{M82} \cdot \left(\frac{(1 + z_{M82}) \cdot d_{M82}}{(1 + z) \cdot d(z)} \right)^2,$$

where $flux(z)$ is the rescaled flux of the object at the new redshift, $flux_{M82}$ is the original flux of M82, z_{M82} (0.000875) is the redshift of the galaxy at its actual distance, z is the redshift at the new distance, d_{M82} (~ 3.6 Mpc) and $d(z)$ are the original and the new distances respectively. The image resolution (CDELTA1 and CDELTA2 parameter in tool *imagev*) was also scaled by a factor:

$$CDELTA(z) = CDELTA_{M82} \cdot \left(\frac{(1 + z_{M82}) \cdot d_{M82} \cdot (1 + z)^2}{(1 + z) \cdot d(z) \cdot (1 + z_{M82})^2} \right),$$

to run the *Athena* WFI simulation. The resulting simulated images for these distances are shown in Figure 23,24,25,26.

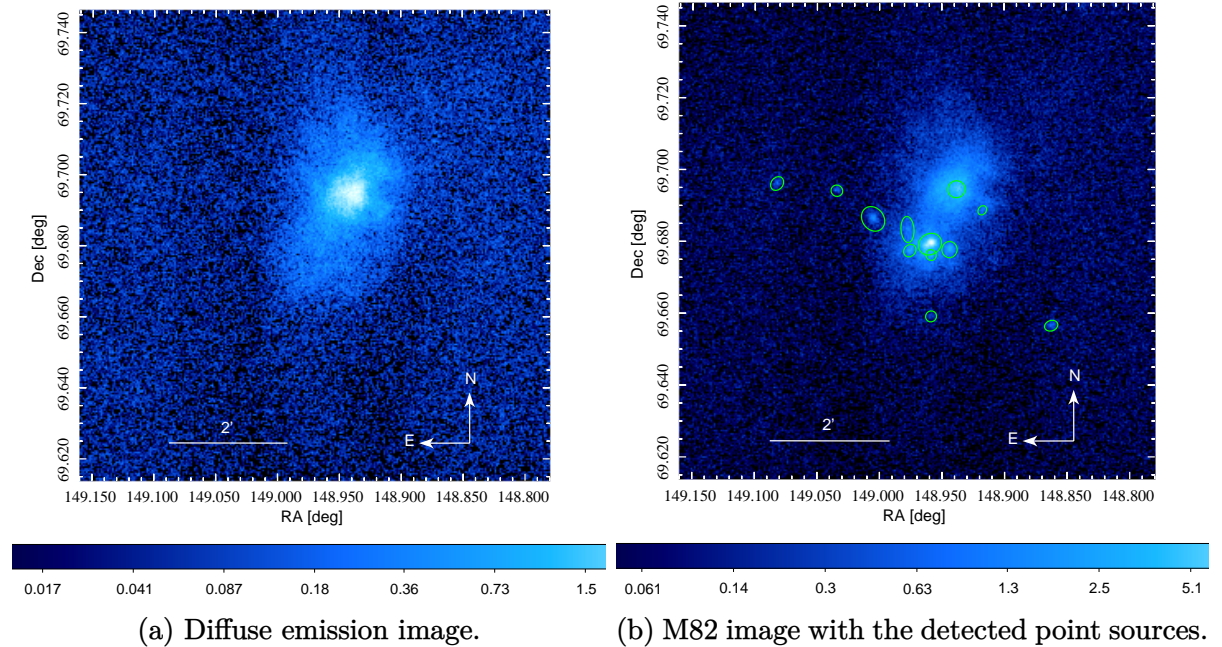


Figure 23: 100ks *Athena* WFI simulation for M82 at 5 times the original distance ($d_{\text{new}} = 18$ Mpc and $z_{\text{new}} = 0.004375$).

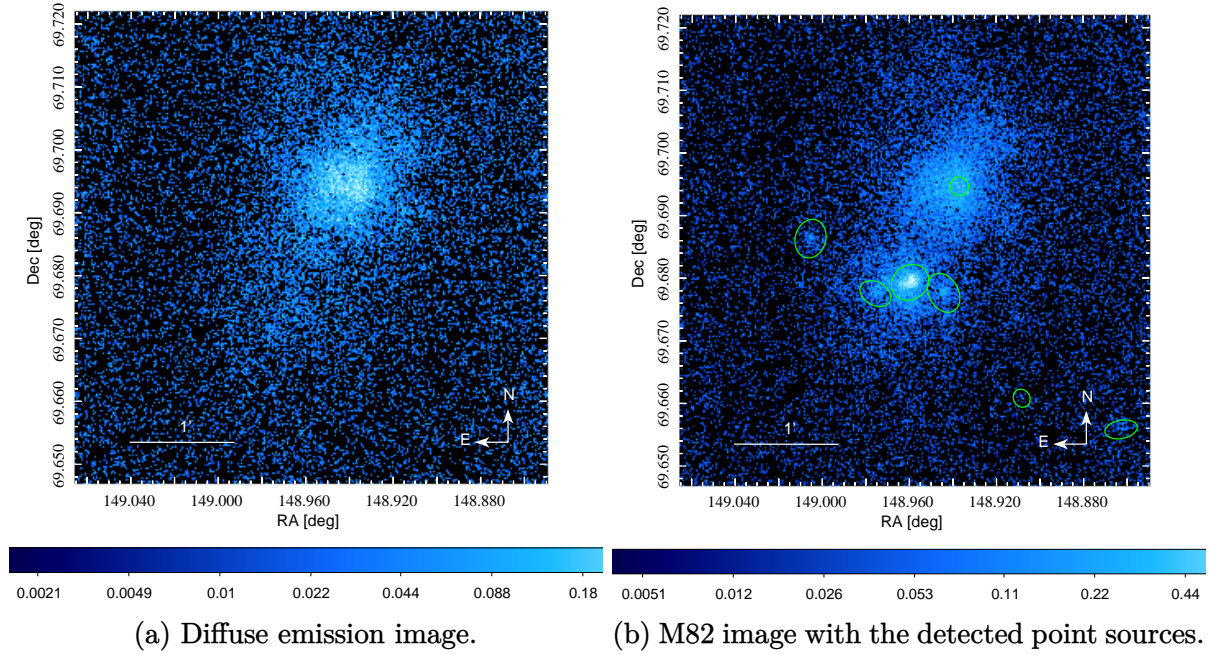


Figure 24: 100ks *Athena* WFI simulation for M82 at 10 times the original distance ($d_{\text{new}} = 36$ Mpc and $z_{\text{new}} = 0.00875$).

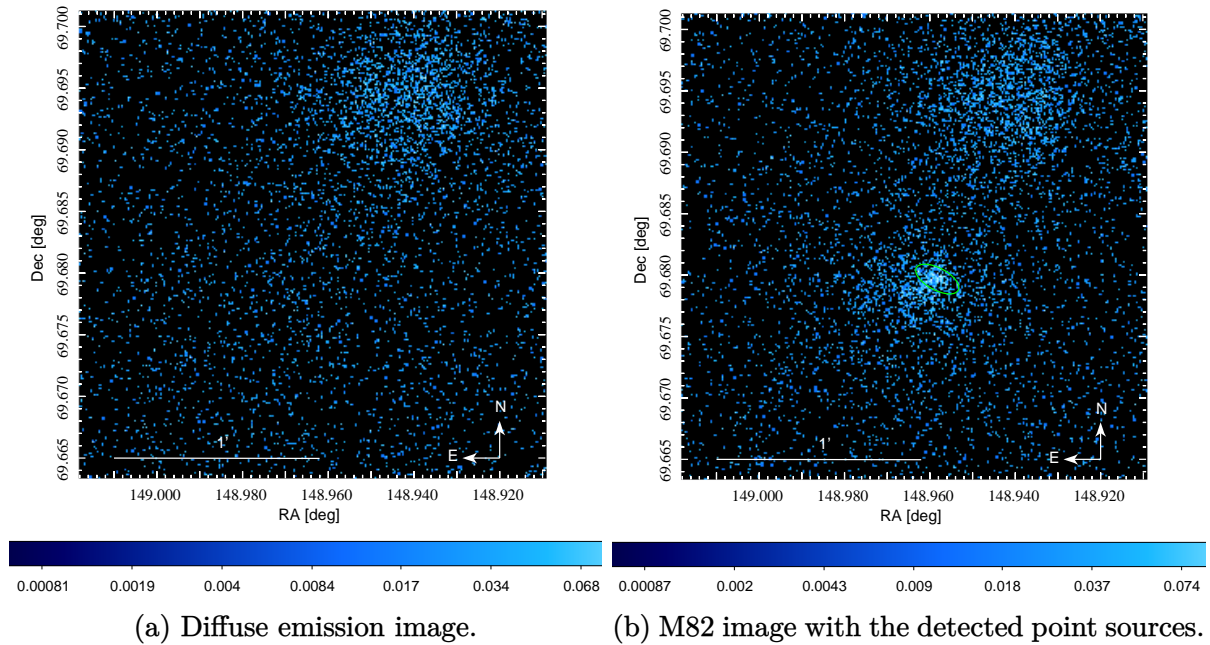


Figure 25: 100ks *Athena* WFI simulation for M82 at 20 times the original distance ($d_{\text{new}} = 72$ Mpc and $z_{\text{new}} = 0.01714$).

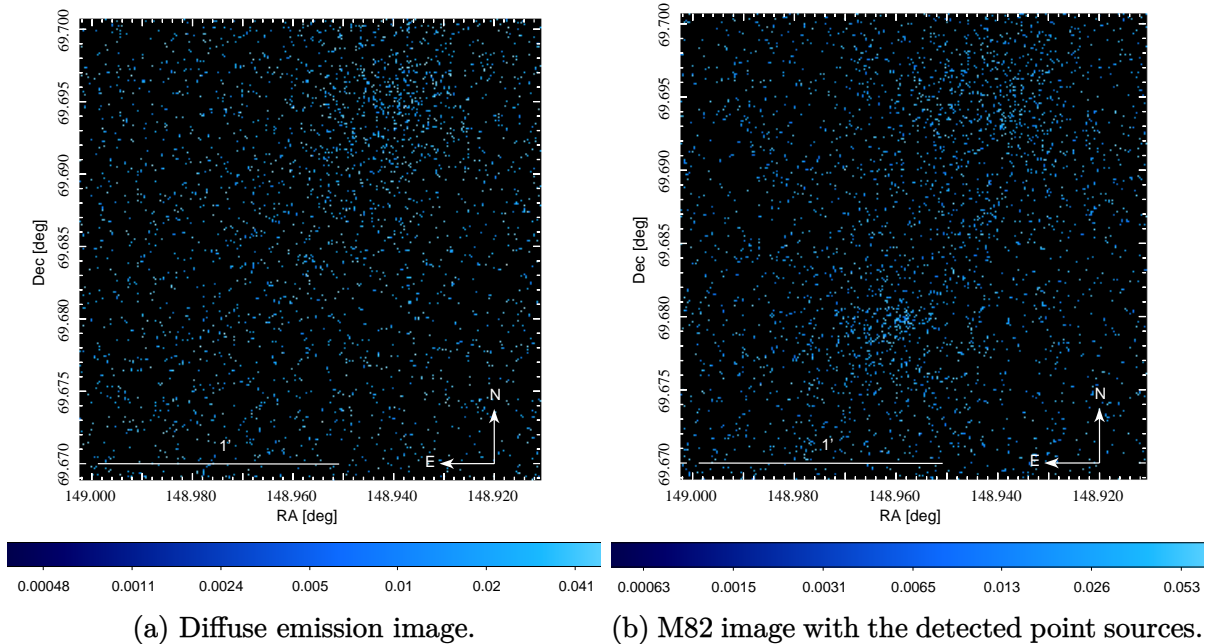


Figure 26: 100ks *Athena* WFI simulation for M82 at 30 times the original distance ($d_{\text{new}} = 108$ Mpc and $z_{\text{new}} = 0.02571$).

In the above images, the luminosity remains constant but the flux and the image size decreases. The images on the right show the simulation with discrete sources in the emission. For comparison, the left images show only the diffuse emission. Regions marked with green ellipse show the result of running CIAO *wavdetect* on the images. Some discrete sources are detected in the image for $z = 0.004375$ and $z = 0.00875$. A single discrete source emission region is also detected in the image for $z = 0.01714$. The emission around this detected region is not observed in the diffuse emission suggesting that it likely originates from unresolved point sources. The introduction of the discrete sources in the emission also results in an extended blob like structure towards the bottom of the diffuse emission further suggesting emission from unresolved sources. No distinct features are visible in the simulation at redshift of 0.02571. These simulations were performed by assuming a 10" half-energy width for the WFI instrument. A smaller half-energy width will most likely result in better spatial resolution and would provide a better understanding of these unresolved sources.

10 Conclusion

In this work, X-ray emission properties of M82's galactic outflows were investigated using *Chandra* ACIS observations. It was found that the soft X-ray emission (0.4–3.0 keV) could be modeled using one or more thermal components while the hard emission required a non-thermal component. Additionally, a decline in the temperature, element abundance, and the X-ray surface brightness was observed as a function of the distance from the central star-bursting core. Further simulations were performed for the *Athena* WFI instrument to achieve an estimate of the spatial resolving capabilities of *Athena* to distinguish the point source emission from the diffuse (unresolved) emission. Observational features could be resolved upto a distance 20 times ($d = 72$ Mpc, $z = 0.01714$) the current distance of M82 ($d = 3.6$ Mpc, $z = 0.000875$). At a distance of ~ 36 Mpc (10 times the current distance to M82), bright point sources can be resolved and detected with *Athena* WFI and at ~ 72 Mpc (20 times the distance to M82), the nuclear region can be distinguished from the rest of the emission from the galaxy.

Starburst galaxies are of interest as they resemble young galaxies in the earlier universe. Since the cosmic star formation rate and furthermore, the cosmic chemical enrichment was substantially higher at epochs corresponding to $z \gtrsim 1$, a starburst phase was very common in the early universe [Persic and Rephaeli, 2002]. So, if the main properties of starburst galaxies in the present universe resemble those of normal galaxies in the earlier universe, study of the local starburst galaxies may provide useful insight into the evolutionary phase and the processes that occurred at that earlier epoch. Outflows from starburst galaxies transport matter and metals beyond the interior of the galaxy, polluting and enriching the circumgalactic medium with metals [Songaila, 1997, Ellison et al., 2000, Aguirre et al., 2005, Bertone et al., 2005] affecting further star-formation activities and cooling mechanisms. Therefore, galactic outflows play an important role in the evolution of their host galaxies, circumgalactic environments, and the intergalactic medium. The feedback potential of galactic outflows is linked to their Hydro-Dynamical (HD) properties and driving mechanisms. For example, winds that transport cosmic rays, hot gases and metals far into the IGM are predominantly driven by cosmic rays, whereas faster winds that are able to transport matter and energy more quickly are likely to be dominated by thermally driven outflows [Yu et al., 2020]. Thus, being able to identify the nature of an outflow to high redshifts acts as a powerful probe that allows us to study the evolution of galaxies, outflows and the effects of galactic-scale feedback over cosmic time. X-rays are a powerful means of probing the thermal properties of hot gas and consequently the HD properties of galactic outflows. *Chandra* and *XMM-Newton* observations have imaged and spatially resolved galactic outflows from nearby starburst galaxies e.g. NGC 253 [Mitsuishi et al., 2013] and M82 (the analysis in this thesis and [Lopez et al., 2020]) in X-rays. Spectral variations and decreasing X-ray brightness over distance from the galactic center is observed for the outflows in M82 §7. The results obtained through these spectral fits show similar trends as compared to previous works (e.g. [Lopez et al., 2020]). However, being able to distinguish differences between thermally driven systems and CR

driven systems for galaxies at a larger distance ($\gtrsim 5$ Mpc) will require high quality spectroscopic data which can be provided by next generation facilities such as *Athena*. With the upcoming advanced facilities like *Athena*, galactic outflows beyond the local universe could be studied and metallicity evolution in the diffuse gas of galactic outflows over different redshifts could be investigated. *Athena* is sufficiently sensitive to detect these outflows at cosmological distances revealing crucial details of the feedback process. The absorption lines and their variability from outflows will determine the ionization state, density, temperature, abundances, velocities, and geometry of the winds down to the inner regions where they are launched. Substantial understanding of the redistribution of matter and metals in the IGM from the galactic winds in star-forming galaxies can be obtained via the high-resolution spectroscopy expected from *Athena*. *Athena* will open up a vast discovery space leading to completely new areas of scientific investigation and the exploration of previously unexplored territories.

Acknowledgements

I express my sincere thanks to Dr. Karl Remeis Sternwarte, Bamberg and Friedrich-Alexander-Universität (FAU), Erlangen-Nürnberg for providing me a platform to perform my thesis in my area of interest. Since the time I approached Prof. Dr. Manami Sasaki for the thesis, she has been a very supportive mentor. The culture within the observatory groups to offer their support made it really easy for me to ask for assistance.

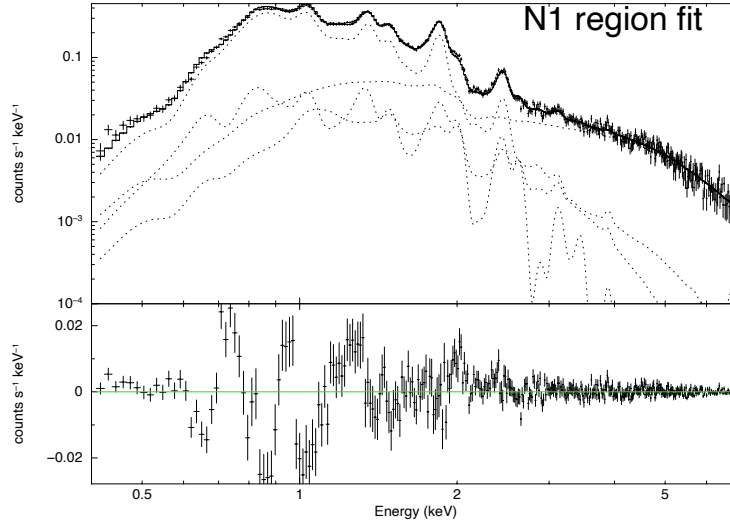
Honestly, I do not know how to express my gratitude to Maximilian Lorenz. First of all, I thank him for believing in me and always helping me with technical issues that I encountered. Right since the first day of my thesis, his knowledge and his modesty have been very inspiring for me. He has tolerated me despite thousands of my questions, and has always responded with completely satisfying and helpful suggestions. I thank Max from the bottom of my heart for being the perfect guide and also giving me a ride to the observatory whenever necessary.

I sincerely thank Prof. Dr. Manami Sasaki of FAU to agreeing to supervise me. The amount of freedom and encouragement I received from her is rare and gave me the confidence to successfully perform the necessary tasks required to complete this thesis. Her research group and the weekly meetings provided me with a good platform to clarify my doubts and always receive the necessary inputs. She was always readily available via zoom for a consultation whenever I needed one.

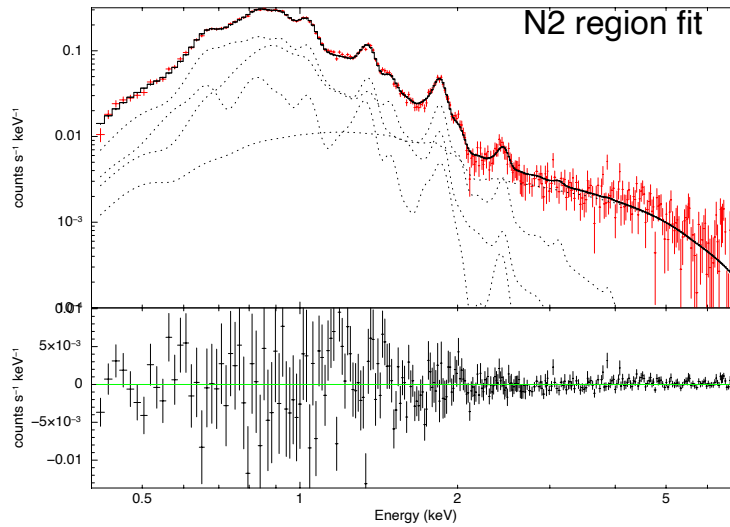
I sincerely thank Prof. Dr. Joern Wilms of FAU for giving me the opportunity to work on the SIXTE tool which proved to be a big part of this project. The knowledge I acquired working under his guidance came in handy when performing the simulations for *Athena*. I would also like to thank Ole König for always being approachable for any SIXTE related or simulations' issues that I encountered.

These have been very difficult times for all of us due to the pandemic. It would have been impossible for me to maintain my spirit without my family back in India who has stood by me and supported me throughout this entire process. My roommates have been a constant guide with their personal Master's thesis experiences. Finally, I would like to thank my friends Ashay Sathe, Karen Terveer, and Johannes Wesseler who were always available through my tantrums and provided me with a good laugh whenever needed.

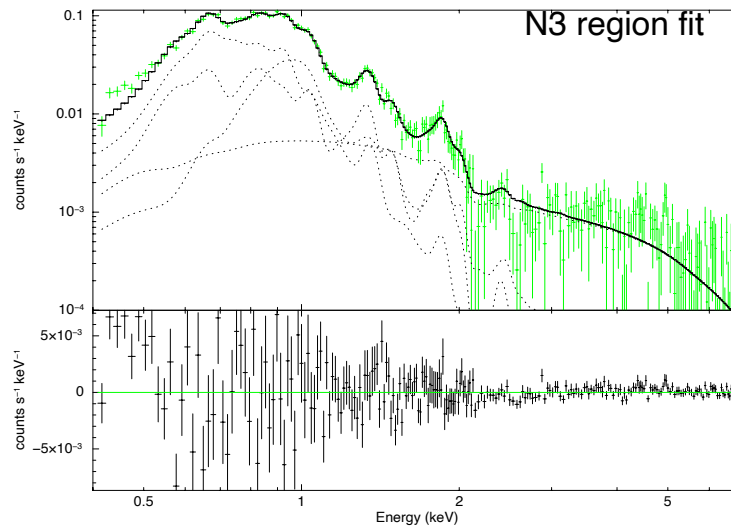
Appendix A Spectral fits



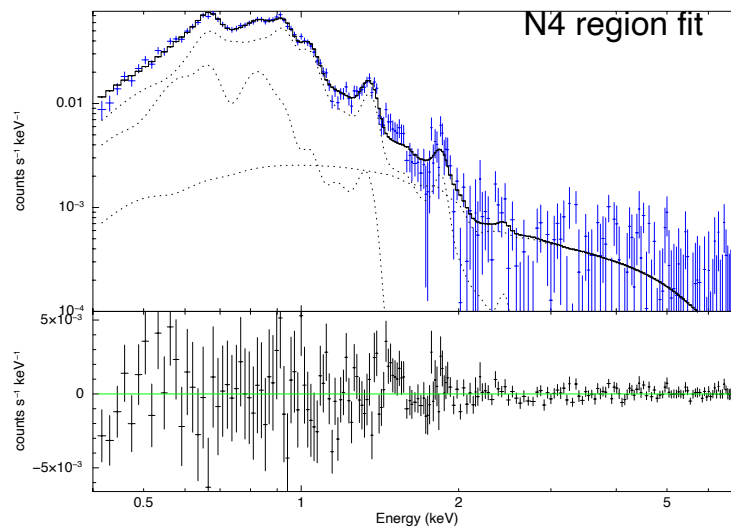
(a) Spectral fit for N1 region. Fitting model: $\text{const} * \text{tbabs} * \text{tbvarabs} * (\text{vnei} + \text{vnei} + \text{vacx} + \text{powerlaw})$.



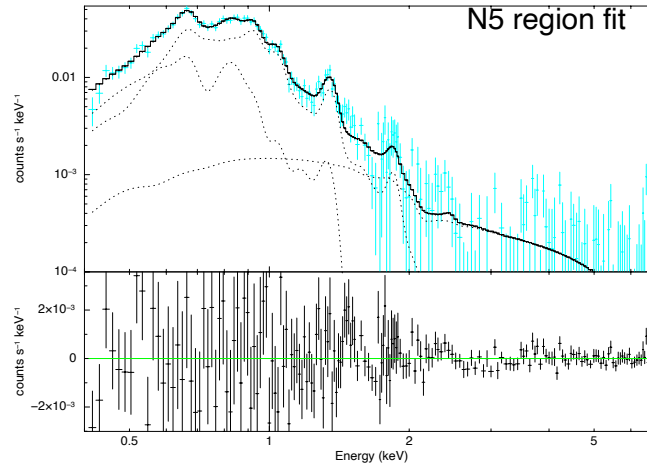
(b) Spectral fit for N2 region. Fitting model: $\text{const} * \text{tbabs} * \text{tbvarabs} * (\text{vnei} + \text{vnei} + \text{vacx} + \text{powerlaw})$.



(c) Spectral fit for N3 region. Fitting model: $\text{const} * \text{tbabs} * \text{tbvarabs} * (\text{vnei} + \text{vnei} + \text{vacx} + \text{powerlaw})$.

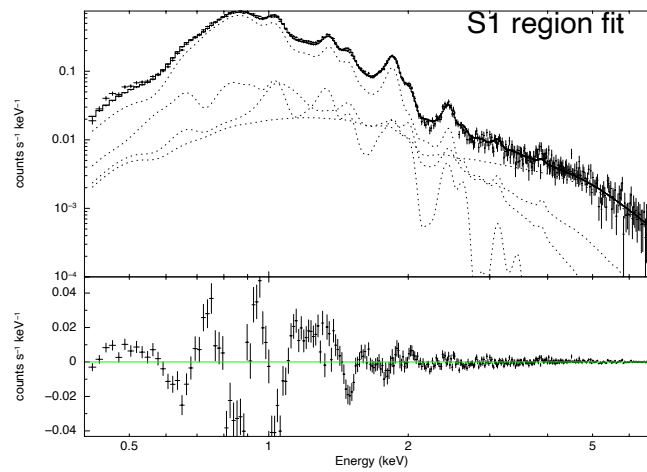


(d) Spectral fit for N4 region. Fitting model: $\text{const} * \text{tbabs} * \text{tbvarabs} * (\text{vnei} + \text{vacx} + \text{powerlaw})$.

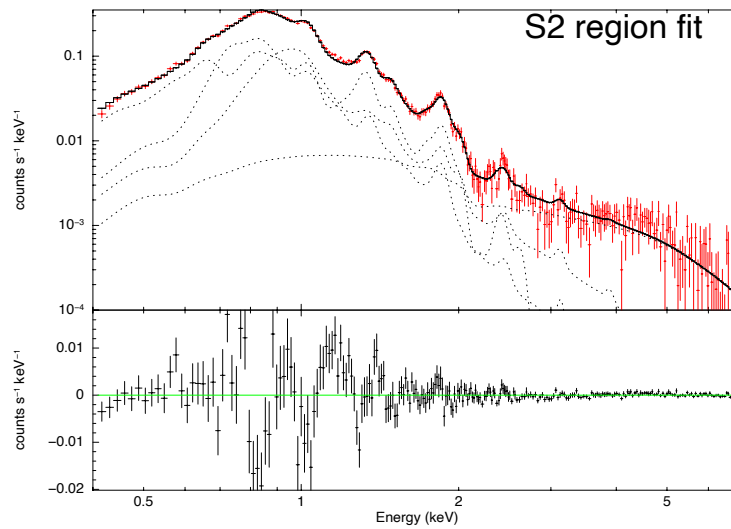


(e) Spectral fit for N5 region. Fitting model: $\text{const} * \text{tbabs} * \text{tbvarabs} * (\text{vnei} + \text{vacx} + \text{powerlaw})$.

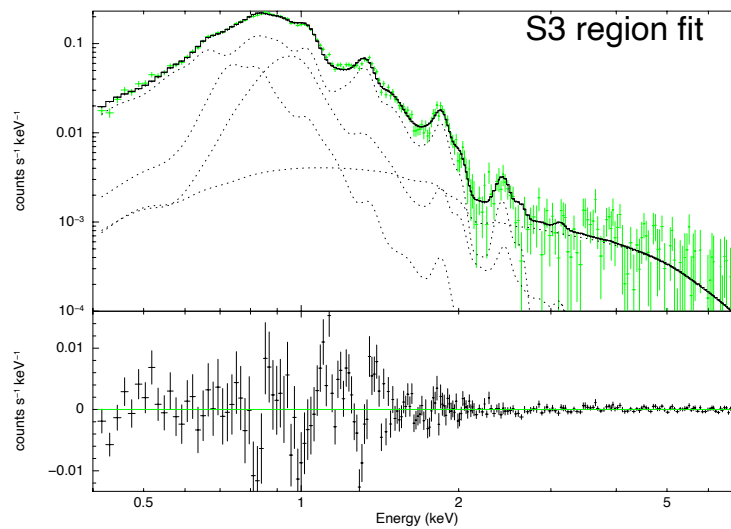
Figure 27: Spectral fitting of the North regions with the fitting residuals at the bottom of each subplot. The markers denote the data points and the solid black line being the fitting curve. The dashed black curves are the individual additive model components.



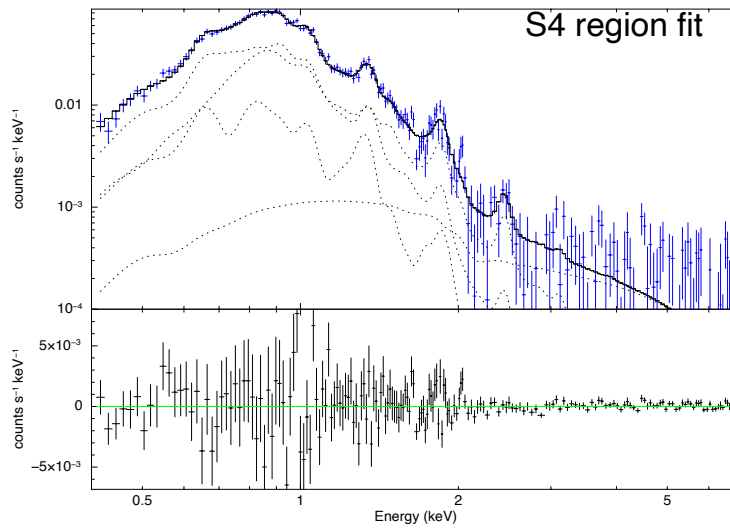
(a) Spectral fit for S1 region. Fitting model: $\text{const} * \text{tbabs} * \text{tbvarabs} * (\text{vnei} + \text{vnei} + \text{vacx} + \text{powerlaw})$.



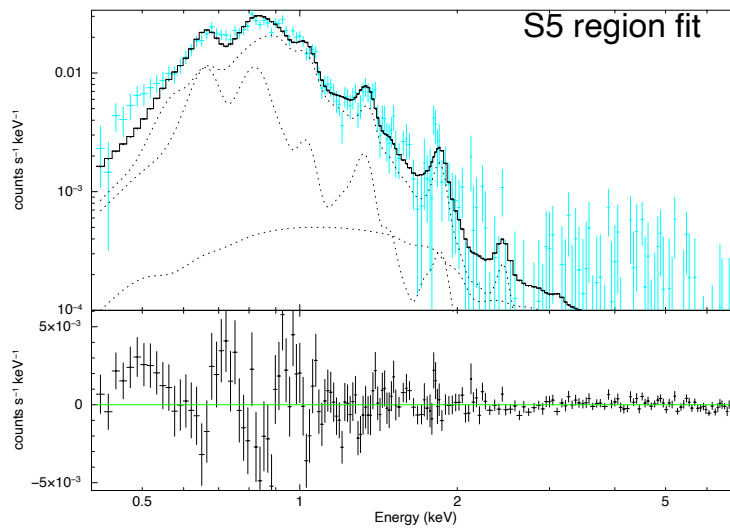
(b) Spectral fit for S2 region. Fitting model: $\text{const} * \text{tbabs} * \text{tbvarabs} * (\text{vnei} + \text{vnei} + \text{vacx} + \text{powerlaw})$.



(c) Spectral fit for S3 region. Fitting model: $\text{const} * \text{tbabs} * \text{tbvarabs} * (\text{vnei} + \text{vnei} + \text{vacx} + \text{powerlaw})$.



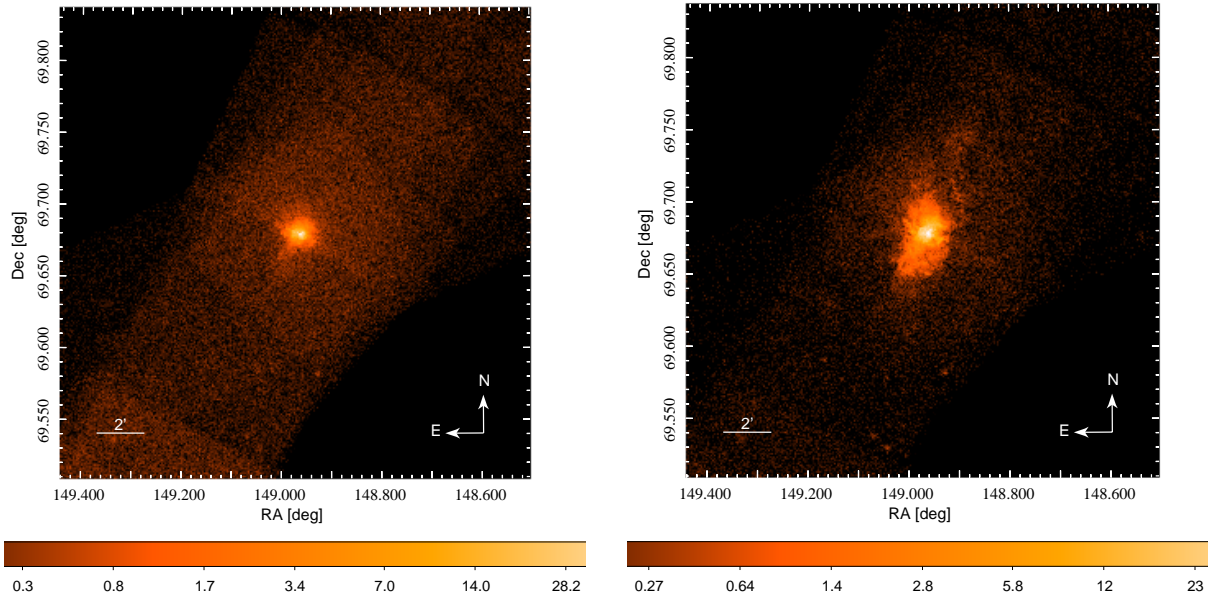
(d) Spectral fit for S4 region. Fitting model: $\text{const} * \text{tbabs} * \text{tbvarabs} * (\text{vnei} + \text{vnei} + \text{vacx} + \text{powerlaw})$.



(e) Spectral fit for S5 region. Fitting model: $\text{const} * \text{tbabs} * \text{tbvarabs} * (\text{vnei} + \text{vacx} + \text{powerlaw})$.

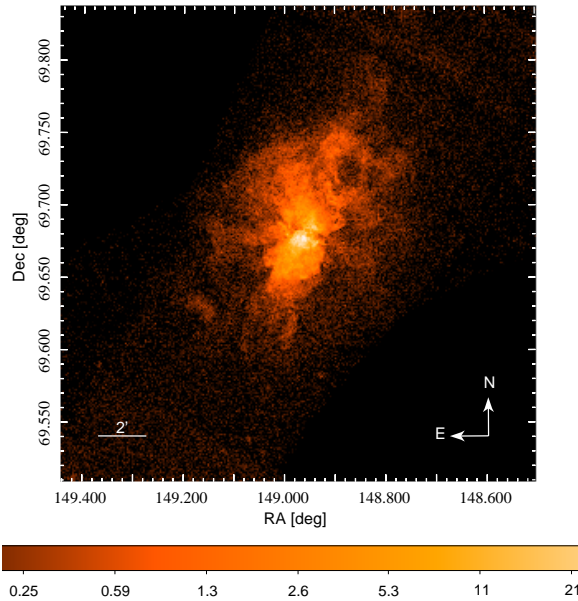
Figure 28: Spectral fitting of the South regions with the fitting residuals at the bottom of each subplot. The markers denote the data points and the solid black line being the fitting curve. The dashed black curves are the individual additive model components.

Appendix B *Chandra* diffuse emission images



(a) Exposure-corrected smoothed diffuse emission image for M82 in the hard energy band (2.0 – 7.0 keV). Used as an Imagefile in the SIMPUT call for region D and N1.

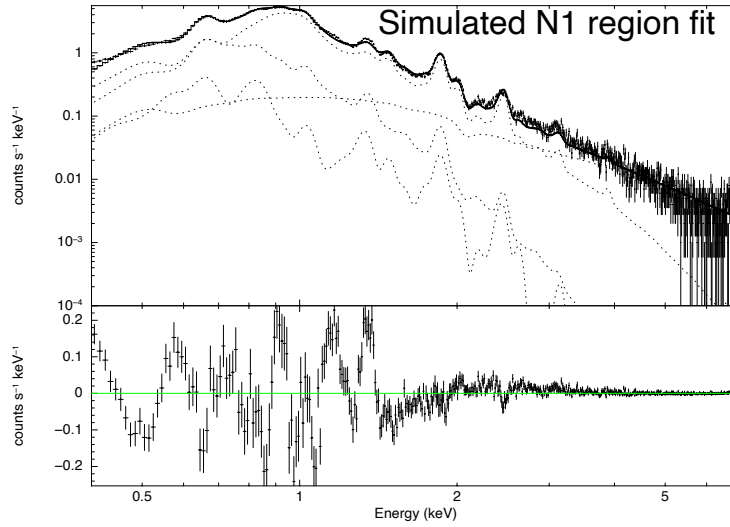
(b) Exposure-corrected smoothed diffuse emission image for M82 in the medium energy band (1.2 – 2.0 keV). Used as an Imagefile in the SIMPUT call for region S1.



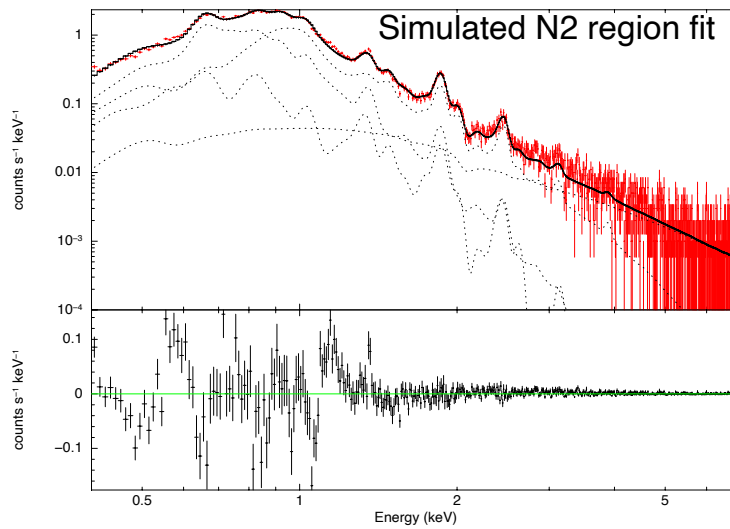
(c) Exposure-corrected smoothed diffuse emission image for M82 in the soft energy band (0.5 – 1.2 keV). Used as an Imagefile in the SIMPUT call for region N2, S2, N3, and S3.

Figure 29: Diffuse emission images created for M82 using *Chandra* ACIS data in the various energy bands.

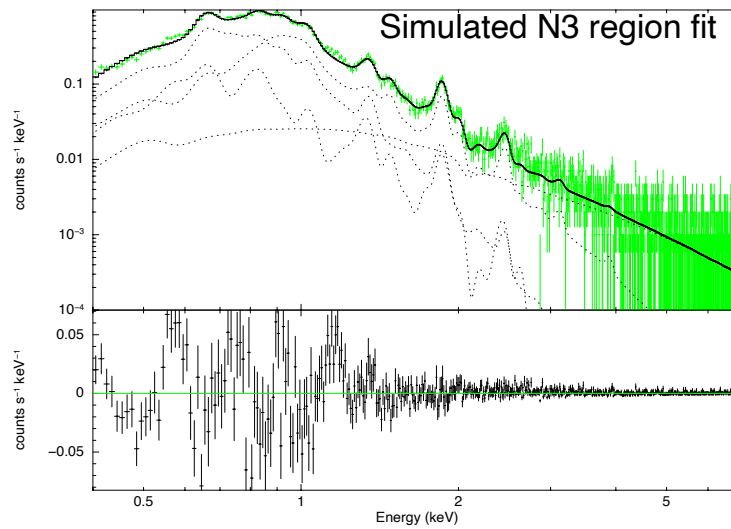
Appendix C Simulated spectral fits



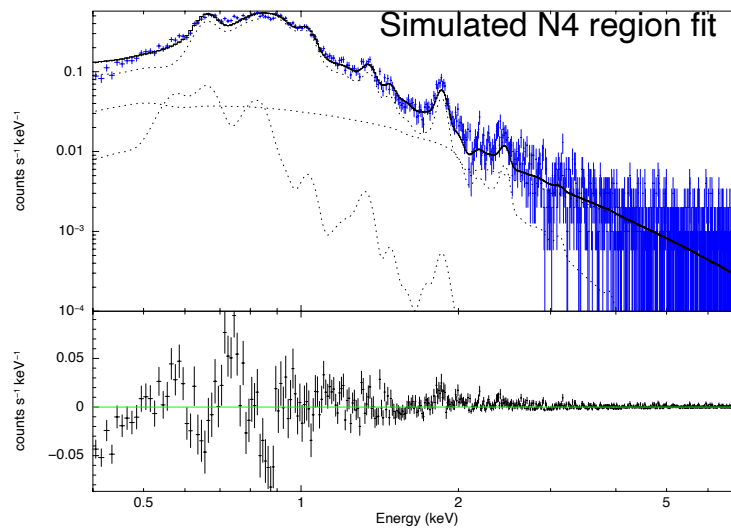
(a) Spectral fit for simulated N1 region. Fitting model: $\text{const} * \text{tbabs} * \text{tbvarabs} * (\text{vnei} + \text{vnei} + \text{vacx} + \text{powerlaw})$.



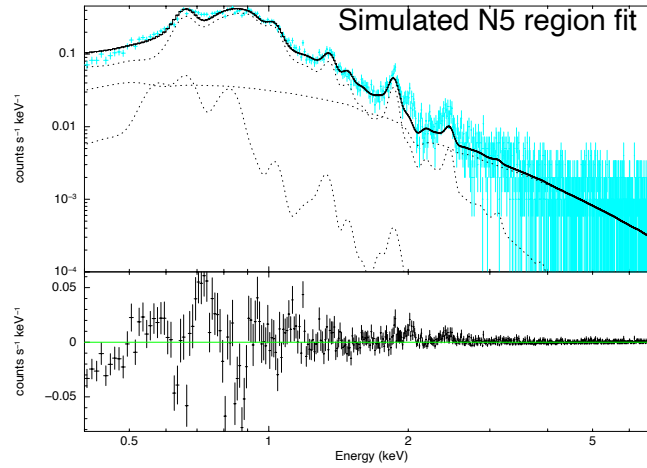
(b) Spectral fit for simulated N2 region. Fitting model: $\text{const} * \text{tbabs} * \text{tbvarabs} * (\text{vnei} + \text{vnei} + \text{vacx} + \text{powerlaw})$.



(c) Spectral fit for simulated N3 region. Fitting model: $\text{const} * \text{tbabs} * \text{tbvarabs} * (\text{vnei} + \text{vnei} + \text{vacx} + \text{powerlaw})$.

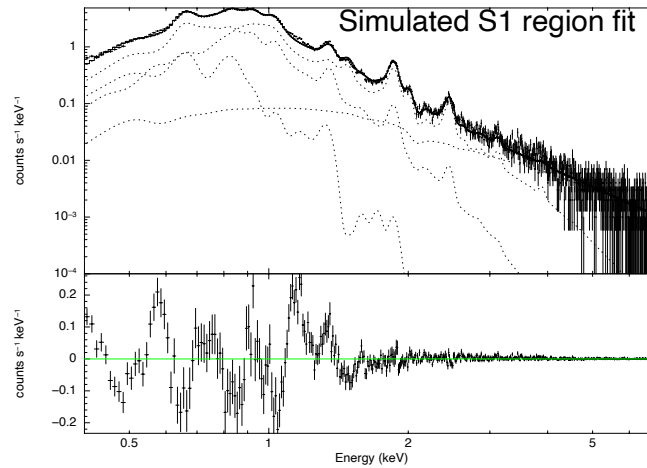


(d) Spectral fit for simulated N4 region. Fitting model: $\text{const} * \text{tbabs} * \text{tbvarabs} * (\text{vnei} + \text{vacx} + \text{powerlaw})$.

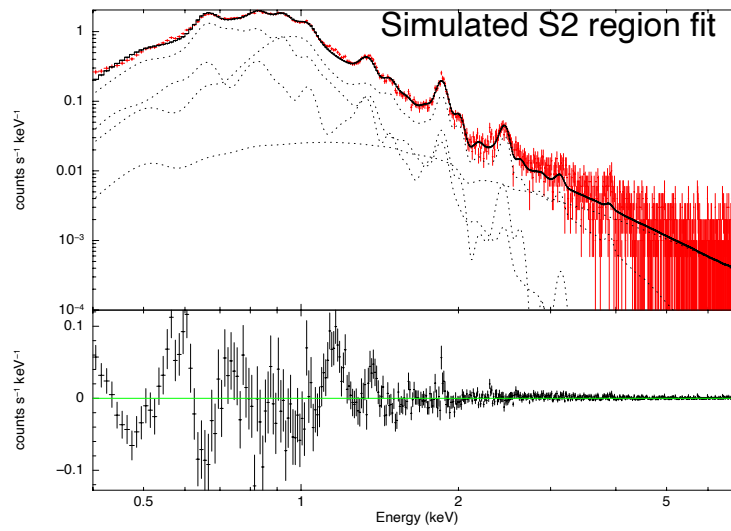


(e) Spectral fit for simulated N5 region. Fitting model:
 $const * tbabs * tbvarabs * (vnei+vacx+powerlaw)$.

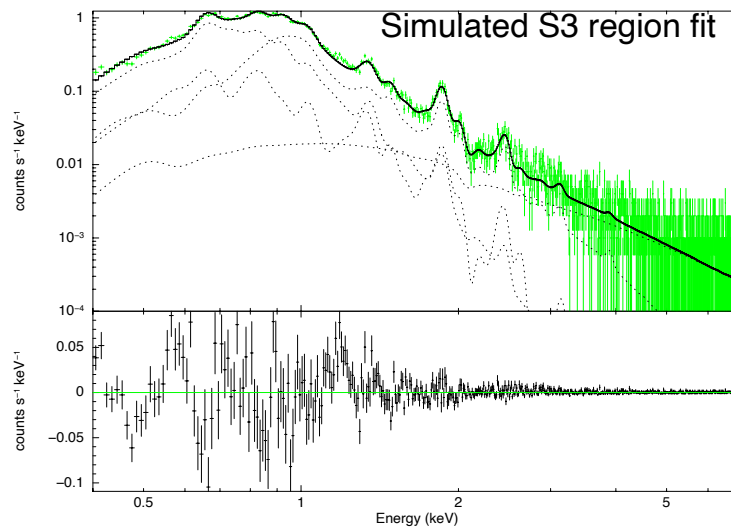
Figure 30: Spectral fitting of the simulated north regions with the fitting residuals at the bottom of each subplot. The markers denote the data points and the solid black line being the fitting curve. The dashed black curves are the individual additive model components.



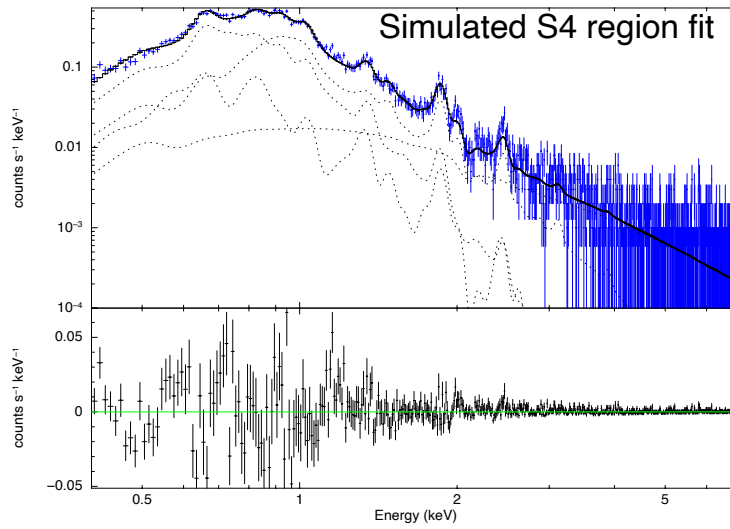
(a) Spectral fit for simulated S1 region. Fitting model:
 $const * tbabs * tbvarabs * (vnei+vnei+vacx+powerlaw)$.



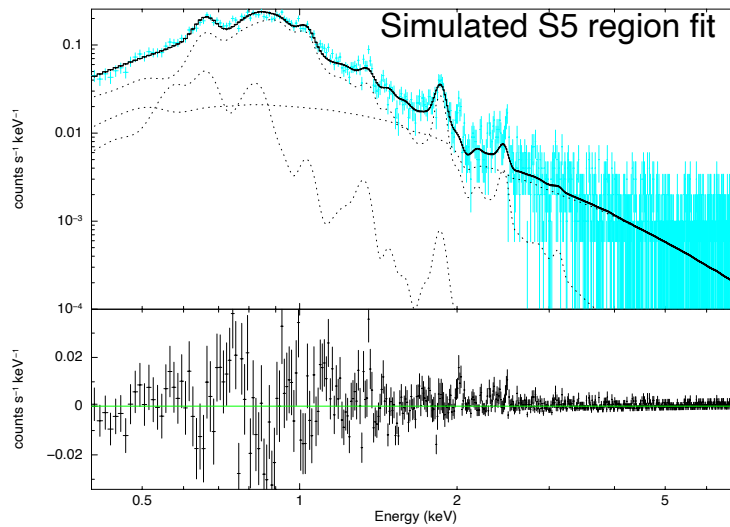
(b) Spectral fit for simulated S2 region. Fitting model: $\text{const} * \text{tbabs} * \text{tbvarabs} * (\text{vnei} + \text{vnei} + \text{vacx} + \text{powerlaw})$.



(c) Spectral fit for simulated S3 region. Fitting model: $\text{const} * \text{tbabs} * \text{tbvarabs} * (\text{vnei} + \text{vnei} + \text{vacx} + \text{powerlaw})$.



(d) Spectral fit for simulated S4 region. Fitting model: $\text{const} * \text{tbabs} * \text{tbvarabs} * (\text{vnei} + \text{vnei} + \text{vacx} + \text{powerlaw})$.



(e) Spectral fit for simulated S5 region. Fitting model: $\text{const} * \text{tbabs} * \text{tbvarabs} * (\text{vnei} + \text{vacx} + \text{powerlaw})$.

Figure 31: Spectral fitting of the simulated south regions with the fitting residuals at the bottom of each subplot. The markers denote the data points and the solid black line being the fitting curve. The dashed black curves are the individual additive model components.

Reg.	$N_{\text{H}}^{\text{M82}}$ ($\times 10^{21} \text{cm}^{-2}$)	kT_1 (keV)	kT_2 (keV)	O/O $_{\odot}$	Ne/Ne $_{\odot}$	Mg/Mg $_{\odot}$	Si/Si $_{\odot}$	S/S $_{\odot}$	Fe/Fe $_{\odot}$	$\chi^2/\text{d.o.f.}$
N5	< 0.01	0.78 ± 0.02	---	$2.72^{+0.43}_{-0.34}$	$0.94^{+0.28}_{-0.20}$	$0.93^{+0.15}_{-0.14}$	1.0	1.0	0.39 ± 0.04	767/639
N4	< 0.01	0.77 ± 0.02	---	$2.55^{+0.25}_{-0.20}$	$1.06^{+0.28}_{-0.08}$	$0.83^{+0.11}_{-0.12}$	1.0	1.0	$0.36^{+0.03}_{-0.04}$	837/639
N3	$1.22^{+0.23}_{-0.20}$	$0.36^{+0.03}_{-0.10}$	$0.91^{+0.09}_{-0.02}$	$0.94^{+0.12}_{-0.41}$	$0.80^{+0.12}_{-0.36}$	$0.78^{+0.14}_{-0.12}$	$1.06^{+0.16}_{-0.14}$	1.0	0.37 ± 0.05	747/636
N2	$1.30^{+0.20}_{-0.10}$	0.41 ± 0.02	0.95 ± 0.01	$0.65^{+0.08}_{-0.05}$	$0.62^{+0.04}_{-0.06}$	$0.61^{+0.04}_{-0.03}$	$0.84^{+0.03}_{-0.06}$	$0.96^{+0.13}_{-0.11}$	$0.34^{+0.02}_{-0.03}$	964/635
N1	$1.39^{+0.01}_{-0.03}$	$0.39^{+0.02}_{-0.01}$	0.93 ± 0.01	1.0	$0.51^{+0.05}_{-0.02}$	$0.58^{+0.02}_{-0.03}$	$0.90^{+0.03}_{-0.02}$	1.12 ± 0.06	0.26 ± 0.00	1746/636
D	$1.46^{+0.03}_{-0.14}$	0.86 ± 0.04	$1.70^{+0.09}_{-0.12}$	1.0	$2.39^{+0.09}_{-0.89}$	$3.97^{+0.31}_{-1.50}$	$0.73^{+0.28}_{-0.20}$	$4.91^{+0.53}_{-0.88}$	$1.16^{+0.10}_{-0.38}$	918/637
S1	1.45 ± 0.05	$0.91^{+0.02}_{-0.00}$	$0.37^{+0.01}_{-0.00}$	1.0	$1.02^{+0.10}_{-0.04}$	$0.86^{+0.07}_{-0.04}$	$0.99^{+0.06}_{-0.05}$	$1.17^{+0.06}_{-0.09}$	$0.34^{+0.02}_{-0.01}$	1319/636
S2*	1.88	0.95	0.31	0.72	0.79	0.54	0.87	0.98	0.43	819/635
S3	$1.63^{+0.37}_{-0.73}$	$0.94^{+0.03}_{-0.06}$	$0.30^{+0.05}_{-0.02}$	$0.78^{+0.19}_{-0.12}$	$0.78^{+0.22}_{-0.13}$	$0.70^{+0.10}_{-0.11}$	$0.96^{+0.09}_{-0.11}$	1.0	$0.49^{+0.08}_{-0.02}$	727/636
S4	$1.32^{+0.58}_{-0.23}$	$0.91^{+0.10}_{-0.03}$	$0.36^{+0.03}_{-0.07}$	$0.95^{+0.21}_{-0.38}$	$0.83^{+0.17}_{-0.28}$	$0.66^{+0.14}_{-0.24}$	$1.02^{+0.21}_{-0.17}$	1.0	$0.35^{+0.14}_{-0.06}$	605/636
S5	0.50 ± 0.12	$0.78^{+0.03}_{-0.04}$	---	$1.60^{+0.54}_{-0.63}$	$0.72^{+0.46}_{-0.20}$	$0.39^{+0.14}_{-0.11}$	1.0	1.0	$0.28^{+0.06}_{-0.05}$	623/639

Table 10: Best-fit parameters, for the simulated spectra, of the tbabs and vnei components of the Xspec model described in Tab 4.

NOTE: A third vnei component not listed in this table was added to the region D model to account for the Fe XXV line. The best-fit temperature of that component was $kT_3 = 0.27 \pm 0.01$ keV.

*: 90% confidence interval for this region could not be determined.

References

- [Aguirre et al., 2005] Aguirre, A., Schaye, J., Hernquist, L., Kay, S., Springel, V., and Theuns, T. (2005). Confronting cosmological simulations with observations of intergalactic metals. *The Astrophysical Journal*, 620(1):L13.
- [ATHENA, 2022] ATHENA (Accessed on 03/08/2022). Athena spacecraft. https://www.the-athena-x-ray-observatory.eu/media/rokgallery/3/36c1b28e-5194-4516-c753-dacaa9390fc0/Athena_XIFU_movie.jpg.
- [Barcons et al., 2017] Barcons, X., Barret, D., Decourchelle, A., den Herder, J., Fabian, A., Matsumoto, H., Lumb, D., Nandra, K., Piro, L., Smith, R., et al. (2017). Athena: ESA’s X-ray observatory for the late 2020s. *Astronomische Nachrichten*, 338(2-3):153–158.
- [Bertone et al., 2005] Bertone, S., Stoehr, F., and White, S. D. (2005). Semi-analytic simulations of galactic winds: volume filling factor, ejection of metals and parameter study. *Monthly Notices of the Royal Astronomical Society*, 359(4):1201–1216.
- [Bland-Hawthorn et al., 2007] Bland-Hawthorn, J., Veilleux, S., and Cecil, G. (2007). Galactic winds: a short review. *Astrophysics and Space Science*, 311(1):87–98.
- [Cappi et al., 1999] Cappi, M., Persic, M., Bassani, L., Franceschini, A., Hunt, L., Molendi, S., Palazzi, E., Palumbo, G., Rephaeli, Y., and Salucci, P. (1999). Diffuse thermal emission from very hot gas in starburst galaxies. *arXiv preprint astro-ph/9908312*.
- [Chevalier, 1977] Chevalier, R. A. (1977). The interaction of supernovae with the interstellar medium. *Annual review of astronomy and astrophysics*, 15:175–196.
- [Chiang and Kong, 2011] Chiang, Y.-K. and Kong, A. K. (2011). The long-term variability of the X-ray sources in M82. *Monthly Notices of the Royal Astronomical Society*, 414(2):1329–1338.
- [Christian and Swank, 1997] Christian, D. J. and Swank, J. (1997). The survey of low-mass x-ray binaries with the einstein observatory solid-state spectrometer and monitor proportional counter. *The Astrophysical Journal Supplement Series*, 109(1):177.
- [Dauser et al., 2019] Dauser, T., Falkner, S., Lorenz, M., Kirsch, C., Peille, P., Cucchetti, E., Schmid, C., Brand, T., Oertel, M., Smith, R., et al. (2019). Sixte: a generic x-ray instrument simulation toolkit. *Astronomy & Astrophysics*, 630:A66.
- [De Grijs, 2001] De Grijs, R. (2001). Star formation timescales in M82. *Astronomy & Geophysics*, 42(4):4–12.

- [Della Ceca et al., 1999] Della Ceca, R., Griffiths, R. E., Heckman, T. M., Lehnert, M. D., and Weaver, K. A. (1999). Asca observations of the starburst-driven superwind galaxy ngc 2146: Broadband (0.6-9 keV) spectral properties. *The Astrophysical Journal*, 514(2):772.
- [Devine and Bally, 1999] Devine, D. and Bally, J. (1999). H α Emission 11 Kiloparsecs above M82. *The Astrophysical Journal*, 510(1):197.
- [Ebisawa et al., 1994] Ebisawa, K., Ogawa, M., Aoki, T., Dotani, T., Takizawa, M., Tanaka, Y., Yoshida, K., Miyamoto, S., Iga, S., Hayashida, K., et al. (1994). Spectral evolution of the bright x-ray nova gs 1124-68 (nova muscae 1991) observed with ginga. *Publications of the Astronomical Society of Japan*, 46:375–394.
- [Ellison et al., 2000] Ellison, S. L., Songaila, A., Schaye, J., and Pettini, M. (2000). The enrichment history of the intergalactic medium—measuring the c iv/hi ratio in the lya forest. *The Astronomical Journal*, 120(3):1175.
- [Fabbiano, 1988] Fabbiano, G. (1988). X-ray spectra and large-scale features of two starburst galaxies-NGC 253 and M82. *The Astrophysical Journal*, 330:672–683.
- [Freedman et al., 2001] Freedman, W. L., Madore, B. F., Gibson, B. K., Ferrarese, L., Kelson, D. D., Sakai, S., Mould, J. R., Kennicutt Jr, R. C., Ford, H. C., Graham, J. A., et al. (2001). Final results from the Hubble Space Telescope key project to measure the Hubble constant. *The Astrophysical Journal*, 553(1):47.
- [Gerke et al., 2011] Gerke, J., Kochanek, C., Prieto, J., Stanek, K., and Macri, L. (2011). A Study of Cepheids in M81 with the Large Binocular Telescope (Efficiently Calibrated with Hubble Space Telescope). *The Astrophysical Journal*, 743(2):176.
- [Goldshmidt and Rephaeli, 1995] Goldshmidt, O. and Rephaeli, Y. (1995). Compton x-ray emission from ngc 253. *The Astrophysical Journal*, 444:113–118.
- [Griffiths et al., 2000] Griffiths, R., Ptak, A., Feigelson, E., Garmire, G., Townsley, L., Brandt, W., Sambruna, R., and Bregman, J. (2000). Hot plasma and black hole binaries in starburst galaxy m82. *Science*, 290(5495):1325–1328.
- [Hanisch et al., 2001] Hanisch, R. J., Farris, A., Greisen, E. W., Pence, W. D., Schlesinger, B. M., Teuben, P. J., Thompson, R. W., and Warnock, A. (2001). Definition of the flexible image transport system (FITS). *Astronomy & Astrophysics*, 376(1):359–380.
- [Harvard, 2019] Harvard (2019). Chandra instruments. https://chandra.harvard.edu/about/science_instruments.html. (Accessed on 03/07/2022).
- [Harvard, 2022a] Harvard (Accessed on 03/07/2022a). Chandra HRC instrument. <https://cxc.harvard.edu/cal/Hrc/index.html>.

- [Harvard, 2022b] Harvard (Accessed on 03/07/2022b). Chandra X-ray Observatory. https://chandra.harvard.edu/graphics/resources/illustrations/sci_illus_721.jpg.
- [Konami et al., 2011] Konami, S., Matsushita, K., Go Tsuru, T., Gandhi, P., and Tamagawa, T. (2011). Suzaku Metal Abundance Patterns in the Outflow Region of M82 and the Importance of Charge Exchange. *Publications of the Astronomical Society of Japan*, 63(sp3):S913–S924.
- [Krieger et al., 2019] Krieger, N., Bolatto, A. D., Walter, F., Leroy, A. K., Zschaechner, L. K., Meier, D. S., Ott, J., Weiss, A., Mills, E. A., Levy, R. C., et al. (2019). The molecular outflow in NGC 253 at a resolution of two parsecs. *The Astrophysical Journal*, 881(1):43.
- [Lehnert et al., 1999] Lehnert, M. D., Heckman, T. M., and Weaver, K. A. (1999). Very extended X-ray and H α emission in M82: implications for the superwind phenomenon. *The Astrophysical Journal*, 523(2):575.
- [Leroy et al., 2015] Leroy, A. K., Walter, F., Martini, P., Roussel, H., Sandstrom, K., Ott, J., Weiss, A., Bolatto, A. D., Schuster, K., and Dessauges-Zavadsky, M. (2015). The multi-phase cold fountain in M82 revealed by a wide, sensitive map of the molecular interstellar medium. *The Astrophysical Journal*, 814(2):83.
- [Lewin et al., 1997] Lewin, W. H., van den Heuvel, E. P., and van Paradijs, J. (1997). *X-ray Binaries*, volume 26. Cambridge University Press.
- [Liu et al., 2011] Liu, J., Mao, S., and Wang, Q. D. (2011). Charge-exchange x-ray emission of m82: K a triplets of ovi, ne ix and mg xi. *Monthly Notices of the Royal Astronomical Society: Letters*, 415(1):L64–L68.
- [Lopez et al., 2020] Lopez, L. A., Mathur, S., Nguyen, D. D., Thompson, T. A., and Olivier, G. M. (2020). Temperature and Metallicity Gradients in the Hot Gas Outflows of M82. *The Astrophysical Journal*, 904(2):152.
- [Mayya et al., 2004] Mayya, Y., Bressan, A., Rodríguez, M., Valdes, J., and Chavez, M. (2004). Star formation history and extinction in the central kiloparsec of M82-like starbursts. *The Astrophysical Journal*, 600(1):188.
- [McKeith et al., 1995] McKeith, C., Greve, A., Downes, D., and Prada, F. (1995). The outflow in the halo of M82. *Astronomy and Astrophysics*, 293:703–709.
- [Meidinger et al., 2017] Meidinger, N., Barbera, M., Emberger, V., Fürmetz, M., Manhart, M., Müller-Seidlitz, J., Nandra, K., Plattner, M., Rau, A., and Treberspurg, W. (2017). The wide field imager instrument for athena. In *UV, X-Ray, and Gamma-Ray Space Instrumentation for Astronomy XX*, volume 10397, page 103970V. International Society for Optics and Photonics.

- [Mitsuishi et al., 2013] Mitsuishi, I., Yamasaki, N. Y., and Takei, Y. (2013). An X-ray study of the galactic-scale starburst-driven outflow in NGC 253. *Publications of the Astronomical Society of Japan*, 65(2):44.
- [Moran et al., 1999] Moran, E. C., Lehnert, M. D., and Helfand, D. J. (1999). X-rays from ngc 3256: High-energy emission in starburst galaxies and their contribution to the cosmic x-ray background. *The Astrophysical Journal*, 526(2):649.
- [Nandra et al., 2013] Nandra, K., Barret, D., Barcons, X., Fabian, A., Herder, J.-W. d., Piro, L., Watson, M., Adami, C., Aird, J., Afonso, J. M., et al. (2013). The Hot and Energetic Universe: A White Paper presenting the science theme motivating the Athena+ mission. *arXiv preprint arXiv:1306.2307*.
- [NASA, 2006] NASA (2006). Chandra/Hubble/Spitzer X-ray/Visible/Infrared Image of M82. <https://hubblesite.org/contents/media/images/2006/14/1882-Image.html>. (Accessed on 03/04/2022).
- [NASA, 2022] NASA (Accessed on 01/25/2022). Coordinates for M82. http://ned.ipac.caltech.edu/cgi-bin/objsearch?objname=m82&extend=no&hconst=73&omegam=0.27&omegav=0.73&corr_z=1&out_csys=Equatorial&out_equinox=J2000.0&obj_sort=RA+or+Longitude&of=pre_text&zv_breaker=30000.0&list_limit=5&img_stamp=YES.
- [Okada et al., 1997] Okada, K., Mitsuda, K., and Dotani, T. (1997). Star-burst galaxy m83 observed from asca. *Publications of the Astronomical Society of Japan*, 49(6):653–658.
- [Owen et al., 2018] Owen, E. R., Jacobsen, I. B., Wu, K., and Surajbali, P. (2018). Interactions between ultra-high-energy particles and protogalactic environments. *Monthly Notices of the Royal Astronomical Society*, 481(1):666–687.
- [Pence et al., 2010] Pence, W. D., Chiappetti, L., Page, C. G., Shaw, R. A., and Stobie, E. (2010). Definition of the flexible image transport system (FITS), version 3.0. *Astronomy & Astrophysics*, 524:A42.
- [Persic and Rephaeli, 2002] Persic, M. and Rephaeli, Y. (2002). X-ray spectral components of starburst galaxies. *Astronomy & Astrophysics*, 382(3):843–859.
- [Pietsch et al., 2001] Pietsch, W., Roberts, T., Sako, M., Freyberg, M., Read, A., Borozdin, K., Branduardi-Raymont, G., Cappi, M., Ehle, M., Ferrando, P., et al. (2001). Xmm-newton observations of ngc 253: Resolving the emission components in the disk and nuclear area. *Astronomy & Astrophysics*, 365(1):L174–L180.
- [Ponz et al., 1994] Ponz, J., Thompson, R., and Munoz, J. (1994). The FITS image extension. *Astronomy and Astrophysics Supplement Series*, 105:53–55.

- [Ptak et al., 1997] Ptak, A., Serlemitsos, P., Yaqoob, T., Mushotzky, R., and Tsuru, T. (1997). The complex x-ray spectra of m82 and ngc 253. *arXiv preprint astro-ph/9702011*.
- [Ranalli et al., 2008] Ranalli, P., Comastri, A., Origlia, L., and Maiolino, R. (2008). A deep X-ray observation of M82 with XMM–Newton. *Monthly Notices of the Royal Astronomical Society*, 386(3):1464–1480.
- [Reichard et al., 2009] Reichard, T. A., Heckman, T. M., Rudnick, G., Brinchmann, J., Kauffmann, G., and Wild, V. (2009). The lopsidedness of present-day galaxies: connections to the formation of stars, the chemical evolution of galaxies, and the growth of black holes. *The Astrophysical Journal*, 691(2):1005.
- [Rephaeli, 1979] Rephaeli, Y. (1979). Relativistic electrons in the intracluster space of clusters of galaxies—the hard x-ray spectra and heating of the gas. *The Astrophysical Journal*, 227:364–369.
- [Rieke et al., 1980] Rieke, G., Lebofsky, M., Thompson, R., Low, F., and Tokunaga, A. (1980). *Astrophys. J*, 238:24.
- [Rubin et al., 2014] Rubin, K. H., Prochaska, J. X., Koo, D. C., Phillips, A. C., Martin, C. L., and Winstrom, L. O. (2014). Evidence for ubiquitous collimated galactic-scale outflows along the star-forming sequence at $z \sim 0.5$. *The Astrophysical Journal*, 794(2):156.
- [Rupke et al., 2005] Rupke, D. S., Veilleux, S., and Sanders, D. (2005). Outflows in infrared-luminous starbursts at $z < 0.5$. II. Analysis and discussion. *The Astrophysical Journal Supplement Series*, 160(1):115.
- [Schmid et al., 2013] Schmid, C., Smith, R., and Wilms, J. (2013). SIMPUT-A File Format for Simulation Input. *hea-www.harvard.edu/heasarc/formats/simput-1.0.0.pdf*.
- [Shopbell and Bland-Hawthorn, 1998] Shopbell, P. and Bland-Hawthorn, J. (1998). The asymmetric wind in M82. *The Astrophysical Journal*, 493(1):129.
- [Soifer et al., 1986] Soifer, B., Sanders, D., Neugebauer, G., Danielson, G., Lonsdale, C. J., Madore, B., and Persson, S. (1986). The luminosity function and space density of the most luminous galaxies in the iras survey. *Astrophysical Journal*, 303(1):L41–L44.
- [Songaila, 1997] Songaila, A. (1997). A lower limit to the universal density of metals at $z \sim 3$. *The Astrophysical Journal*, 490(1):L1.
- [Soria and Wu, 2002] Soria, R. and Wu, K. (2002). X-ray sources in the starburst spiral galaxy M83—Nuclear region and discrete source population. *Astronomy & Astrophysics*, 384(1):99–111.

- [Strickland et al., 1996] Strickland, D., Ponman, T., and Stevens, I. (1996). ROSAT Observations of the Galactic Wind in M82. *arXiv preprint astro-ph/9608064*.
- [Strickland and Heckman, 2007] Strickland, D. K. and Heckman, T. M. (2007). Iron line and diffuse hard x-ray emission from the starburst galaxy m82. *The Astrophysical Journal*, 658(1):258.
- [Strickland et al., 2000] Strickland, D. K., Heckman, T. M., Weaver, K. A., and Dahlem, M. (2000). Chandra observations of ngc 253: new insights into the nature of starburst-driven superwinds. *The Astronomical Journal*, 120(6):2965.
- [Strickland et al., 2009] Strickland, D. K., Hornschemeier, A., Ptak, A., Schlegel, E., Tremonti, C., Tsuru, T., Tüllmann, R., and Zezas, A. (2009). Starburst Galaxies: Outflows of Metals and Energy into the IGM. *arXiv preprint arXiv:0902.2945*.
- [Strickland and Stevens, 2000] Strickland, D. K. and Stevens, I. R. (2000). Starburst-driven galactic winds—i. energetics and intrinsic x-ray emission. *Monthly Notices of the Royal Astronomical Society*, 314(3):511–545.
- [Swinburne, 2022] Swinburne, U. (Accessed on 01/20/2022). Starburst galaxy — cosmos. <https://astronomy.swin.edu.au/cosmos/s/starburst+galaxy>.
- [Telesco, 1988] Telesco, C. M. (1988). Enhanced star formation and infrared emission in the centers of galaxies. *Annual review of astronomy and astrophysics*, 26(1):343–376.
- [Tsuru et al., 2007] Tsuru, T. G., Ozawa, M., Hyodo, Y., Matsumoto, H., Koyama, K., Awaki, H., Fujimoto, R., Griffiths, R., Kilbourne, C., Matsushita, K., et al. (2007). X-ray spectral study of the extended emission, ‘the cap’, located 11.6 kpc above the disk of M82. *Publications of the Astronomical Society of Japan*, 59(sp1):S269–S282.
- [Varenius et al., 2016] Varenius, E., Conway, J., Martí-Vidal, I., Aalto, S., Barcos-Muñoz, L., König, S., Pérez-Torres, M., Deller, A., Moldón, J., Gallagher, J., et al. (2016). Subarcsecond international LOFAR radio images of Arp 220 at 150 MHz—A kpc-scale star forming disk surrounding nuclei with shocked outflows. *Astronomy & Astrophysics*, 593:A86.
- [Veilleux et al., 2005] Veilleux, S., Cecil, G., and Bland-Hawthorn, J. (2005). Galactic winds. *Annu. Rev. Astron. Astrophys.*, 43:769–826.
- [Walter et al., 2017] Walter, F., Bolatto, A. D., Leroy, A. K., Veilleux, S., Warren, S. R., Hodge, J., Levy, R. C., Meier, D. S., Ostriker, E. C., Ott, J., et al. (2017). Dense molecular gas tracers in the outflow of the starburst galaxy NGC 253. *The Astrophysical Journal*, 835(2):265.

- [Weisskopf et al., 2000] Weisskopf, M. C., Tananbaum, H. D., Van Speybroeck, L. P., and O’Dell, S. L. (2000). Chandra X-ray Observatory (CXO): overview. In *X-Ray Optics, Instruments, and Missions III*, volume 4012, pages 2–16. International Society for Optics and Photonics.
- [Wells and Greisen, 1979] Wells, D. C. and Greisen, E. W. (1979). FITS—a flexible image transport system. In *Image processing in astronomy*, page 445.
- [Wilson and Rothschild, 1983] Wilson, C. and Rothschild, R. (1983). Observations of a hard x-ray component in the spectrum of nova ophiuchi. *The Astrophysical Journal*, 274:717–722.
- [Woltjer, 1972] Woltjer, L. (1972). Supernova remnants. *Annual Review of Astronomy and Astrophysics*, 10:129.
- [Yu et al., 2021] Yu, B. B., Owen, E. R., Pan, K.-C., Wu, K., and Ferreras, I. (2021). Outflows from starburst galaxies with various driving mechanisms and their X-ray properties. *Monthly Notices of the Royal Astronomical Society*, 508(4):5092–5113.
- [Yu et al., 2020] Yu, B. B., Owen, E. R., Wu, K., and Ferreras, I. (2020). A hydrodynamical study of outflows in starburst galaxies with different driving mechanisms. *Monthly Notices of the Royal Astronomical Society*, 492(3):3179–3193.
- [Yun et al., 1994] Yun, M. S., Ho, P. T., and Lo, K. (1994). A high-resolution image of atomic hydrogen in the M81 group of galaxies. *Nature*, 372(6506):530–532.
- [Zezas et al., 1998] Zezas, A., Georgantopoulos, I., and Ward, M. (1998). Rosat and asca observations of x-ray luminous starburst galaxies: Ngc 3310 and 3690. *Monthly Notices of the Royal Astronomical Society*, 301(4):915–925.
- [Zhang et al., 2014] Zhang, S., Wang, Q. D., Ji, L., Smith, R. K., Foster, A. R., and Zhou, X. (2014). Spectral modeling of the charge-exchange x-ray emission from m82. *The Astrophysical Journal*, 794(1):61.

Declaration

I hereby confirm that the work shown and written in this thesis is performed independently by me with only using the aids mentioned otherwise.

Place, Date

Saurabh Mittal